



ALMA MATER STUDIORUM
UNIVERSITÀ DI BOLOGNA

DEPARTMENT OF PHYSICS AND ASTRONOMY "A. RIGHI"

SECOND CYCLE DEGREE

PHYSICS

Fission chambers characterization outside ALFRED reactor vessel

Supervisor
Prof. Cristian Massimi

Co-supervisor
Dr. Gabriele Firpo

Defended by
Laura Lerza

July 2025

Academic Year 2024/2025

Abstract

This thesis presents the characterization of fission chambers for neutron monitoring in the external region of the ALFRED reactor vessel, a European demonstrator for Lead-cooled Fast Reactor (LFR) technology. The study is based on a dedicated Monte Carlo simulation framework aimed at evaluating neutron and photon fluxes under realistic operating conditions. A simplified yet representative model of the reactor geometry was developed to estimate the radiation environment outside the vessel. Several commercially available fission chambers were analyzed in terms of their sensitivity across thermal, epithermal, and fast neutron spectra. The results provide quantitative insight into detector response, operational constraints, and optimal deployment strategies, supporting the development of reliable neutron instrumentation for Generation IV fast reactors.

Contents

Abstract	i
List of Figures	iv
1 Introduction and scope	1
2 Technological Overview and Fundamental Concepts	5
2.1 Main characteristics of the Lead Fast Reactors	5
2.1.1 Nuclear Fission	5
2.1.2 The Nuclear Reactor	8
2.1.3 LFR: The Leading Gen IV Technology	12
2.1.4 ALFRED	14
2.2 Main characteristics of the fission chambers	24
2.2.1 Generic fission chambers	24
2.3 Fission chambers Suitable for LFR applications	27
3 Methodology	33
3.1 Modeling Approach	36
3.1.1 Source definition	39
3.2 Reactor model simplification and input creation	42
3.3 Neutron flux evaluation	45
3.4 Photon flux evaluation	48
3.5 Fission chambers characterization	50
4 Results	53
4.1 Reactor Model simplification	54
4.1.1 Source interface characterization	58
4.2 Neutron fluxes results	62
4.2.1 Results of the SDEF Approach	62
4.2.2 Results of the SSR/SSW Approach	66
4.3 Photon fluxes results	71
4.4 Fission chamber characterization results	73
5 Conclusions	79
Appendix I	81
Appendix II	85

Appendix III

89

References

112

List of Figures

1	Schematic illustration of the fission nuclear process (to the left) and of the chain reaction (to the right).	7
2	Illustrative scheme of a Pressurized Water Reactor: (1) core; (2) moderator/coolant; (3) steam generator; (4) turbines; (5) capacitor; (6) cooling tower.	9
3	Generation of nuclear fission power plants. The time intervals correspond to the design and early implementations of several generations of reactors.	10
4	Plant diagram of the 6 Generation IV fission reactor technologies. . . .	12
5	General system architecture of the ALFRED reactor coolant system. The figure shows the geometric configuration of some of the major components of the RCS together with the internal structures that guide the motion of the fluid.	17
6	Cutaway of the ALFRED reactor vessel.	18
7	Cutaway of ALFRED internal steel structures.	19
8	Simplified section of ALFRED core.	21
9	View (left), cross-section (middle) and details of the ALFRED steam generator.	22
10	View (left) and cross-section (right) images of the ALFRED coolant pump.	24
11	Fission chamber scheme in which the principal general characteristics are depicted.	25
12	Thermal spectrum used for the estimation of the correction factor in Equation 4.	31
13	Scheme of the methodology.	34
14	Modelling approach scheme.	36
15	Interface identification in both the ALFRED Core Model and the ALFRED Reactor Model (Courtesy of ENEA and Ansaldo Nucleare).	38
16	Scheme for the Source definition process.	39
17	Scheme for the Source definition process(Courtesy of ENEA and Ansaldo Nucleare).	40
18	Scheme of the process for the ALFRED Reactor Model simplification and input creation.	42
19	ALFRED Reactor Model with the CAD imported parts.	43
20	Neutron flux evaluation process scheme.	45
21	Upper mesh tallies of ADVANTG (Courtesy of Ansaldo Nucleare). . . .	46
22	Lower mesh tallies of ADVANTG (Courtesy of Ansaldo Nucleare). . . .	46
23	Fission chambers position in the upper part of the reactor.	47
24	Fission chambers positions in the lower part of the reactor.	48

25	Photon flux evaluation process scheme.	48
26	Alfred Reactor Model with the shortest photon path through the lead highlighted (left) and the volume of the second simulation (right). . . .	50
27	Characterization of fission chambers scheme.	50
28	Representative graph of the Fast reactor spectrum and the Thermal one.	51
29	ALFRED Reactor Vessel Model with the CAD imported parts, the concrete shielding, and the homogenized components.	54
30	Meridian section of the Steam Generator with a zoom on the right. . .	55
31	Meridian sections of the Pump Propeller: in correspondence with the tube (left) and in correspondence with the propeller (center), and longitudinal section of the propeller part (left).	56
32	Interface in the ALFRED Core Model with tallies identification.	58
33	Graph (logarithmic scale) of the Neutron Flux vs Energy of the upper part of the interface between the ALFRED Core Model and the ALFRED Reactor Vessel Model.	59
34	Graph (logarithmic scale) of the Neutron Flux vs Energy of the middle part of the interface between the ALFRED Core Model and the ALFRED Reactor Vessel Model.	59
35	Graph (logarithmic scale) of the Neutron Flux vs Energy of the lower part of the interface between the ALFRED Core Model and the ALFRED Reactor Vessel Model.	60
36	Graph (logarithmic scale) of the Neutron Flux vs Energy of the entire interface between the ALFRED Core Model and the ALFRED Reactor Vessel Model.	60
37	Graph (logarithmic scale) of the Photon Flux vs Energy of the entire interface between the ALFRED Core Model and the ALFRED Reactor Vessel Model.	61
38	Behavior of the total neutron flux in the upper part of the ALFRED Reactor Vessel Model with the SDEF approach.	62
39	Graph (logarithmic scale) of the normalized Neutron Flux vs Energy simulated with the SDEF Approach, in the two Tallies in correspondence of the Steam Generator.	63
40	Graph (logarithmic scale) of the normalized Neutron Flux vs Energy simulated with the SDEF Approach, in the two Tallies in correspondence of only pure Lead.	63
41	Graph (logarithmic scale) of the normalized Neutron Flux vs Energy simulated with the SDEF Approach, in the two Tallies in correspondence of the Pump Propeller.	64
42	Behavior of the total neutron flux in the lower part of the ALFRED Reactor Vessel Model with the SDEF approach.	65

43	Graph (logarithmic scale) of the normalized Neutron Flux vs Energy simulated with the SDEF Approach, in the three Tallies in the lower part of the reactor.	65
44	Behavior of the total neutron flux in the upper part of the ALFRED Reactor Vessel Model with the SSR/SSW approach.	66
45	Graph (logarithmic scale) of the normalized Neutron Flux vs Energy simulated with the SSR/SSW Approach, in the two Tallies in correspondence of the Steam Generator.	67
46	Graph (logarithmic scale) of the normalized Neutron Flux vs Energy simulated with the SSR/SSW Approach, in the two Tallies in correspondence of pure Lead.	67
47	Graph (logarithmic scale) of the normalized Neutron Flux vs Energy simulated with the SSR/SSW Approach, in the two Tallies in correspondence of the Pump Propeller.	68
48	Behavior of the total neutron flux in the lower part of the ALFRED Reactor Vessel Model with the SSR/SSW approach.	69
49	Graph (logarithmic scale) of the normalized Neutron Flux vs Energy simulated with the SSR/SSW Approach, in the three Tallies in the lower part of the reactor.	69
50	Representation of the shortest photon path through the lead (left), of the mesh used in photon simulation (middle) and the contour plot (right) of the background radiation level (10^{-8} Gy/h), the result of the photon simulation (10^{-15} Gy/h) and a reference value (1 Gy/h).	71
51	Graph of the Photon Dose vs Depth obtained by the simulation with the SDEF Approach in correspondence of the shortest path through lead. Since the real depth cannot be disclosed, the depth values are not defined numerically.	72
52	Neutron induced ^{235}U fission cross section vs Neutron Energy.	74
53	Behavior of the total neutron flux in the ALFRED Reactor Vessel Model with the SSR/SSW approach.	77
54	ALFRED Core Model received by ENEA (left) and result of the ALFRED Core Model running by Ansaldo Nucleare (right).	81
55	Alfred Reactor Vessel and Inner Structures.	82

1 Introduction and scope

The transition toward sustainable, low-carbon energy production has become one of the primary challenges of the 21st century. Within this context, nuclear energy continues to represent a key pillar in the global energy mix, offering a reliable and large-scale alternative to fossil fuels. However, the long-term viability of nuclear energy relies on continued technological innovation aimed at enhancing safety, minimizing waste, and optimizing fuel resources. In recent decades, significant research and development efforts have been devoted to Generation IV reactor concepts, which are designed to address many of the limitations of current reactor technologies.

Among the various Generation IV systems under investigation, Lead-cooled Fast Reactors (LFRs) stand out due to their unique combination of safety, fuel flexibility, and operational efficiency. These reactors utilize fast-spectrum neutrons and a liquid lead coolant, which confers several advantages over conventional water- or gas-cooled systems. The high boiling point of lead, for example, allows for operation at atmospheric pressure, thereby reducing the risk of pressurized accidents. Moreover, lead offers excellent radiation shielding properties and is chemically inert with respect to air and water, contributing to the overall safety profile of the reactor. From a neutronic perspective, lead has a low neutron moderation capacity, preserving the fast neutron spectrum needed for efficient transmutation of actinides and improved fuel utilization.

In addition to their favorable safety characteristics, LFRs are designed to operate with a wide range of fuels, including mixed oxide (MOX) fuels, minor actinides, and even fertile materials such as Thorium and depleted Uranium. This fuel versatility opens the door to closed fuel cycle strategies and the potential for significant reductions in high-level radioactive waste.

The ALFRED reactor (Advanced Lead-cooled Fast Reactor European Demonstrator) represents a key milestone in the European road map for LFR deployment. As a pre-commercial prototype, ALFRED aims to validate the main technological features of LFRs in an operational environment. Ensuring accurate neutron monitoring within such reactors is essential not only for safe reactor operation but also for the qualification of experimental data, the calibration of simulation tools, and the verification of design assumptions.

In this framework, neutron detection systems—and in particular, fission chambers—play a fundamental role. Fission chambers are gas-filled detectors that exploit the fission reactions of fissile isotopes (e.g., U-235 or Pu-239) to provide a current proportional to the incident neutron flux. These detectors are valued for their robustness, real-

time response, and capability to operate over a wide range of neutron fluxes. However, their performance can be affected by external conditions, such as high temperatures, intense gamma radiation fields, and the energy distribution of the neutron spectrum, especially in fast reactor environments.

This thesis focuses on the characterization of fission chambers intended for deployment in the peripheral region of the ALFRED reactor, specifically outside the reactor safety vessel. The selected location poses several technical challenges: the detectors must endure prolonged exposure to elevated temperatures and intense mixed radiation fields, all while maintaining stability, linearity, and sensitivity. The research addresses the feasibility of using commercially available fission chambers in this context and seeks to determine their performance in terms of sensitivity to different neutron energy ranges: thermal, epithermal, and fast.

The core objectives of this work are threefold:

- To evaluate the suitability of existing fission chamber designs for application in LFR environments.
- To determine their neutron sensitivity profiles using detailed simulation-based methods, considering both standard calibration spectra and realistic reactor operating conditions.
- To contribute to the development and optimization of neutron monitoring strategies in LFR systems, enhancing reactor safety, operability, and the accuracy of nuclear instrumentation systems.

In order to achieve these goals, this thesis employs Monte Carlo simulations using state-of-the-art computational tools for neutron transport modeling, coupled with detailed detector geometry and material specifications. The results are analyzed to identify trends, validate detector sensitivities under different spectral conditions, and assess overall performance against the requirements imposed by the ALFRED reactor environment.

The remainder of this thesis is organized as follows:

- Chapter 1 introduces the context, motivation, and objectives of the research, outlining its scope within the broader field of nuclear instrumentation and Generation IV reactor development.
- Chapter 2 presents the theoretical and technical background relevant to the study. This includes an overview of LFR technology, neutron transport theory, and the fission chamber physics.

- Chapter 3 describes the methodology adopted throughout the work, including the design of simulation models, selection of materials and detector types, and implementation of variance reduction techniques to ensure computational efficiency.
- Chapter 4 discusses the Monte Carlo simulation results in detail, providing quantitative analyses of the energy-dependent flux response and the influence of placement and environmental conditions. The chapter ends with the last data analysis and final discussion about their implications for fission chamber deployment in LFRs.
- Chapter 5 concludes the thesis by synthesizing the main findings and providing a general overview of the study.

2 Technological Overview and Fundamental Concepts

This chapter provides the necessary background to understand the context, motivations, and technical foundations of the study. It is structured into two main parts: the first focuses on the characteristics of Lead Fast Reactors (LFRs), while the second presents an overview of the fission chambers considered for neutron flux monitoring in such a system.

The first section (Section 2.1) outlines the fundamental principles of nuclear fission and the basic components and operation of a nuclear reactor, laying the groundwork for the subsequent focus on ALFRED (Advanced Lead Fast Reactor European Demonstrator), a reference design used in this work. This part highlights the specific features of LFR technology, including its safety characteristics, coolant choice, and relevance in the context of next-generation nuclear systems.

The second section (Section 2.2) examines the main characteristics of fission chambers with an initial discussion on generic fission chamber technologies, their operating principles, and typical applications in radiation detection. Then it narrows down to the selection and suitability of fission chambers for LFR environments, with an emphasis on the particular challenges posed by fast-spectrum lead-cooled systems.

In summary, this chapter forms the technical foundation for the modeling and simulation activities described in the subsequent chapters.

2.1 Main characteristics of the Lead Fast Reactors

2.1.1 Nuclear Fission

Nuclear fission is a nuclear reaction in which the atomic nucleus of heavy elements (such as Uranium and Plutonium) undergoes decay, splitting into nuclei of lighter atoms with lower atomic numbers—and consequently lower masses—while releasing a substantial amount of energy [1][2][3][4].

It has been well established since the early stages of nuclear era that, in the presence of a neutron flux, a Uranium-235 (${}_{92}^{235}\text{U}$) nucleus tends to capture a neutron, forming Uranium-236 (${}^{236}\text{U}$), which subsequently undergoes immediate fission. This reaction results in the formation of lighter nuclei, referred to as fission products or fission

fragments (see Figure 1, left) [1][2][4]. The probability of neutron capture is inversely proportional to the velocity of the neutron; therefore, the so-called 'thermal-energy neutrons', *i.e.*, at thermal equilibrium with the environment and therefore the lowest speed, are those that maximize the probability of a fission process[3].

The energy released during fission corresponds to the difference between the mass of the Uranium-236 nucleus and the combined mass of the two resulting fission fragments, with this mass difference converted into energy according to Einstein's mass-energy equivalence [1][2]. The fission fragments propagate through the surrounding medium, interacting via electrostatic forces with the negatively charged electron clouds of nearby atoms. As a result of these interactions, they gradually lose velocity and eventually come to rest within a few thousandths of a millimeter, converting their kinetic energy into thermal energy [2][3][5].

However, the heat generated by a single fission event is negligible; fission would not be a viable energy source without a cumulative effect known as the chain reaction. In addition to producing the fission fragments, each fission event releases on average, two to three fast neutrons, referred to as fission neutrons. These neutrons, upon propagation through the medium, may collide with other Uranium-235 nuclei, inducing further fission events. This process results in successive generations of neutrons, which in turn trigger additional fission reactions, leading to a self-sustaining chain reaction (see Figure 1, right)[1][3][4]. This mechanism, if properly controlled, enables the large-scale production of energy within a nuclear reactor, making nuclear fission a practical and industrially exploitable process[4].

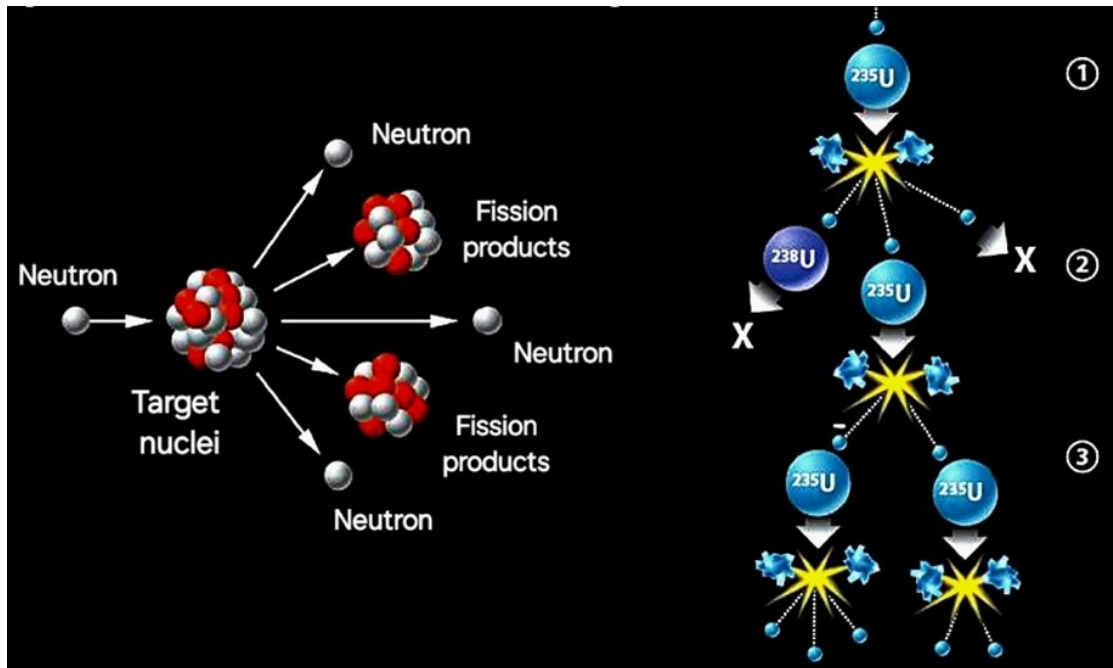


Figure 1: Schematic illustration of the fission nuclear process (to the left) and of the chain reaction (to the right).

Particle / Energy Type	Origin	Energy (MeV)
Fission fragments	Nucleus splitting	~ 168
Neutrons (2-3 per fission)	Emitted during fission	~ 5
Prompt gamma rays	Immediate nuclear de-excitation	~ 7
Delayed gamma rays	Decay of fission products	~ 6
Beta particles (electrons)	Beta decay of fission products	~ 8
Electron antineutrinos	Beta decay of fission products	~ 12

Table 1: Energy components and their origin in a typical nuclear fission event induced by a thermal neutron ($E \sim 0.025$ eV). Values are average estimates.

Particle / Energy Type	Origin	Energy (MeV)
Fission fragments	Nucleus splitting	~ 170
Neutrons (2-4 per fission)	Emitted during fission	~ 7
Prompt gamma rays	Immediate nuclear de-excitation	~ 7.5
Delayed gamma rays	Decay of fission products	~ 6
Beta particles (electrons)	Beta decay of fission products	~ 8
Electron antineutrinos	Beta decay of fission products	~ 12

Table 2: Energy components and their origin in a typical nuclear fission event induced by a fast neutron ($E \sim 1$ MeV). Energy values are approximate averages.

2.1.2 The Nuclear Reactor

A nuclear reactor is a complex technological system through which nuclear energy is produced, controlled, and converted into electrical energy for practical use [6][7]. Among the various reactor types developed, one of the most common is the Pressurized Water Reactor (PWR), depicted in Figure 2. This reactor is schematically composed of the containment structure, the core, the heat exchange systems, and the steam turbines [7][8]. The core, the region where the chain reaction occurs and heat is generated, is approximately cylindrical in shape and consists of the following components [6]:

- Fuel – Typically a mixture of uranium isotopes, primarily containing Uranium-235 (^{235}U), where fission takes place. Natural uranium is a mixture of ^{235}U and ^{238}U (which does not undergo fission for thermalized neutrons), with ^{235}U making up 0.7% of the total. This concentration is too low to sustain a stable chain reaction. Therefore, the uranium undergoes enrichments to increase the ^{235}U content to a few percent. The fuel is generally in the form of uranium oxide, contained within cylindrical fuel rods [6][7].
- Moderator – A material with a lower atomic mass than fuel, typically water, in which the fuel rods are immersed. The moderator slows down the neutrons produced by fission, a necessary condition for sustaining further fission reactions and maintaining the chain reaction [6][7].
- Coolant – The substance that circulates around the fuel elements, keeping them at operational temperatures and transferring the heat generated by fission to be converted into mechanical energy in the turbine generator, ultimately producing electricity. In PWR reactors, such as the one depicted, the coolant and the moderator are the same substance, meaning that pressurized water serves both functions [6][8].

- Absorber – A material (such as boron, cadmium, gadolinium, etc.) with extremely-high radiative capture cross section, and therefore capable of absorbing neutrons and removing them from the chain reaction. By adjusting the amount of absorber, the number of neutrons available for fission can be controlled, thereby regulating the chain reaction. The absorber is typically in the form of movable control rods, which can be inserted or withdrawn from the core, even in small increments, to precisely adjust neutron flux [6][9].

From a functional perspective, even a minor temporary variation in the depth of immersion of the control rods allows for power adjustments by increasing or decreasing neutron absorption. In this type of reactor, the moderator water absorbs heat from the fuel without boiling, as it is maintained at high pressure. It is then circulated through a heat exchanger, serving simultaneously as a coolant and thermal carrier [6][8].

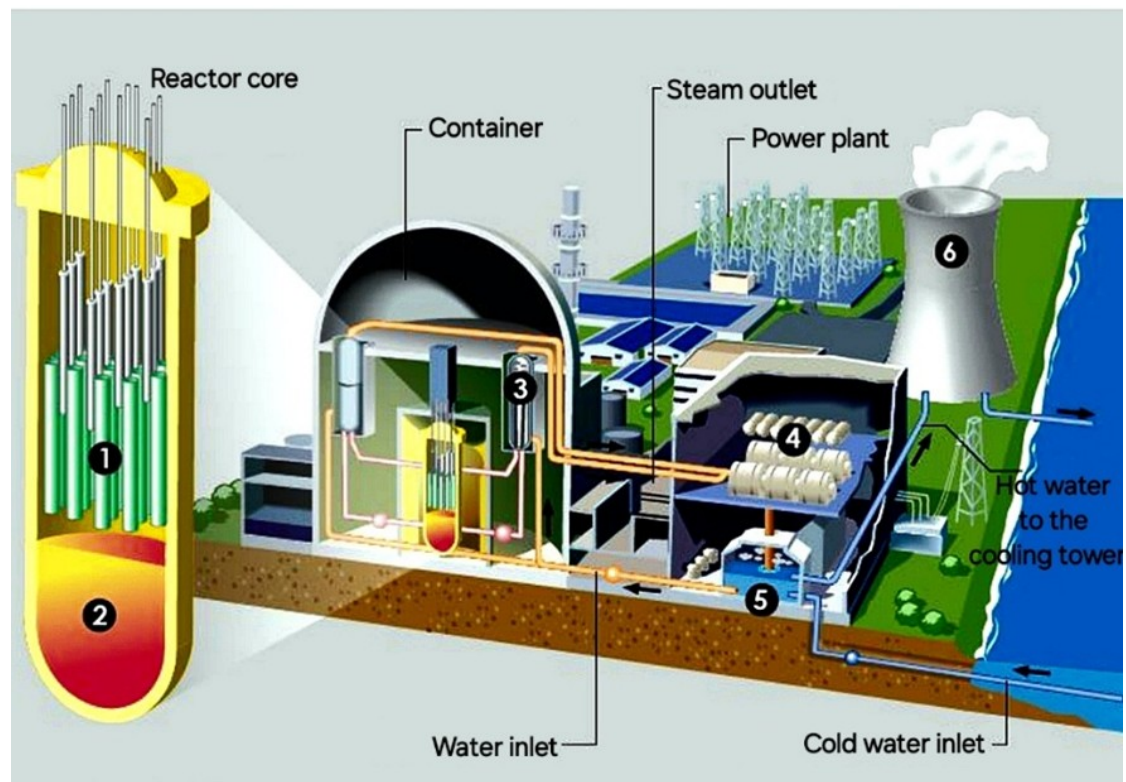


Figure 2: Illustrative scheme of a Pressurized Water Reactor: (1) core; (2) moderator/coolant; (3) steam generator; (4) turbines; (5) capacitor; (6) cooling tower.

The operational sequence of a nuclear reactor can be summarized as follows (refer to Figure 2) [7][8]:

1. The fuel (green) heats the pressurized water. Control rods (gray) absorb neutrons to regulate or halt the fission process.
2. The fuel and control rods are surrounded by pressurized water, which functions both as a moderator and a coolant.
3. The heated water from the reactor is pumped through a heat exchanger, where it generates high-pressure steam in the secondary circuit.
4. The steam drives a turbine to generate electricity.
5. A condensation system removes the latent heat, converting the exhaust steam from the turbine back into water, which is then recirculated by the steam generator.
6. The water circulating in the condenser is typically passed through a cooling tower, where heat is dissipated into the atmosphere [7][10].

Generations of Nuclear Reactors

At the dawn of the nuclear era, starting in the second half of the twentieth century, a wide variety of nuclear technologies were developed and tested, differing primarily in fuel type, moderator, and coolant medium. This marks the First Generation (Gen I) of nuclear reactors [10]. Over the following decades, advancements and refinements led to the development of subsequent reactor generations, as illustrated in Figure 3.

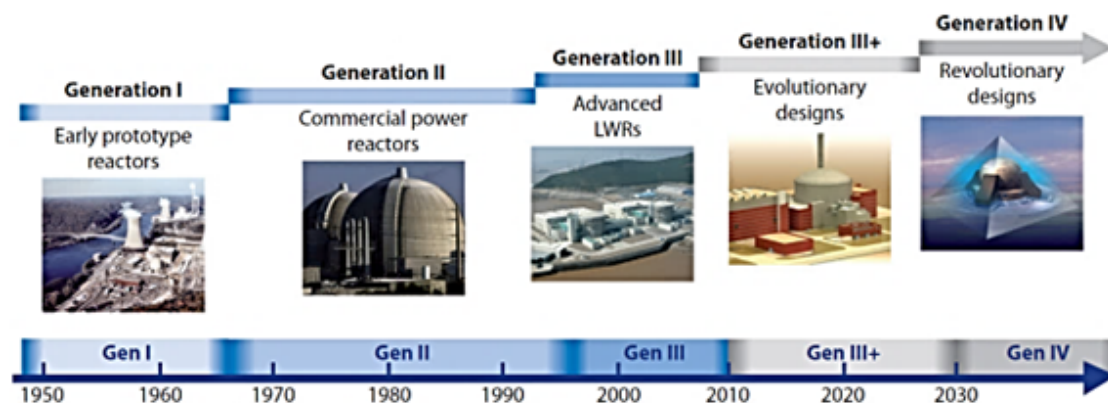


Figure 3: Generation of nuclear fission power plants. The time intervals correspond to the design and early implementations of several generations of reactors.

With the onset of the demonstration and commercial phase in the 1960s (Beginning of the Second Generation, Gen II), only a few of these technologies became dominant, establishing themselves as key reactor types [10][8]. Today, nearly all of the 439 operational nuclear reactors worldwide fall into three main categories:

- Pressurized Water Reactors (PWR)
- Boiling Water Reactors (BWR)
- Pressurized Heavy Water Reactors (PHWR)

The drive to increase reactor power output (up to few gigawatts of thermal energy per reactor) has played a crucial role in nuclear development, enabling economies of scale that have significantly reduced the impact of capital investment costs on the overall cost of energy production, thereby improving economic viability [10].

From the 1990s onward, the development of Third Generation (Gen III) and Generation III+ reactors introduced significant safety improvements, primarily through the ever-increasing integration of passive safety systems. These systems do not require human intervention or external power sources, relying instead on natural physical phenomena for emergency response [10][8]. The combination of enhanced safety and improved economic competitiveness has driven the success of these reactors, which today represent the primary commercially available designs for new nuclear installations worldwide [10].

At the turn of the 21st century, the international nuclear community laid the foundation for the development of Fourth Generation (Gen IV) reactors, designed to achieve even higher standards in terms of safety, sustainability, economic efficiency, and non-proliferation [10][11]. Approximately 100 experts from Generation IV International Forum (GIF) evaluated over 130 reactor designs and selected 6 advanced reactor concepts that best align with these objectives (Figure 4) [11]:

1. Gas-Cooled Fast Reactor (GFR)
2. Lead-Cooled Fast Reactor (LFR)
3. Molted Salt Reactor (MSR)
4. Supercritical Water-Cooled Reactor (SCWR)
5. Sodium Cooled Fast Reactor (SFR)
6. Very High-Temperature Fast Reactor (VHTR)

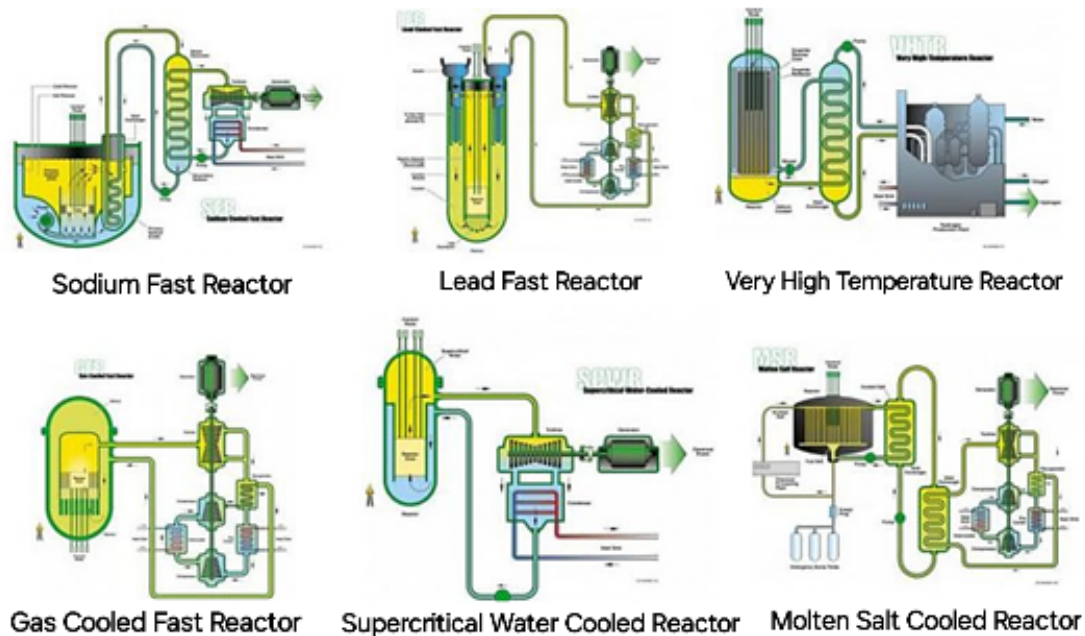


Figure 4: Plant diagram of the 6 Generation IV fission reactor technologies.

Some of these technologies (GFR, LFR, MSR, SFR) employ a coolant with minimal neutron moderation capability, classifying them as fast reactors. This characteristic allows for the maximization of sustainability and safety objectives [12][13][11]. Several of these designs have well-established historical backgrounds and technological experience, with notable startups and major industry players considering them for commercialization and next-generation nuclear deployment [8].

2.1.3 LFR: The Leading Gen IV Technology

Among the Gen IV reactor concepts, many organizations, particularly within the European Union, recognize the Lead-Cooled Fast Reactor (LFR) as one of the most promising, advanced, and closest to commercialization[14][13][11]. Alongside the Sodium-Cooled Fast Reactor (SFR), the LFR is one of the few Gen IV designs with prior operational experience, dating back to its early applications in submarine propulsion during the 1950s and 1960s in the Soviet Union, the United States, and the United Kingdom [15][16].

The LFR possesses several key attributes that align with Gen IV objectives and long-term sustainability goals [9][11]:

- **Fuel Cycle and Waste Management:** As a fast reactor, the Lead-cooled Fast Reactor (LFR) enables a closed fuel cycle through the use of fast neutrons, which

can induce fission in Uranium and Plutonium isotopes contained in spent nuclear fuel. This is made possible by the use of lead as a coolant, a material with very low neutron moderation compared to water, thereby preserving a hard neutron spectrum. Consequently, the LFR can efficiently burn spent fuel, minimizing nuclear waste production and reducing long-term radiotoxicity through advanced reprocessing techniques.[17][18].

- **Economic Efficiency:** the high heat transfer efficiency of liquid lead allows for a compact and simplified reactor design. The high operating temperature enables additional applications, such as industrial heat supply [14][19][20].
- **Safety Features:** lead coolant is chemically inert, eliminating risks associated with steam explosions or hydrogen production (as in water-cooled reactors). Its high thermal capacity provides passive cooling, significantly reducing the risk of core damage during accidents. Lead offers effective radiation shielding, minimizing radiation exposure risks [21][7].
- **Non-proliferation benefits:** as a fast reactor, the LFR can operate using Mixed Oxide Fuel (MOX), a blend of Uranium and Plutonium, which makes plutonium extraction for weaponization significantly more challenging [22].

The high neutron fluence characteristic of fast reactors presents significant technological challenges related to materials performance (i.e., Displacement Per Atom, DPA, effect on fuel cladding and structural reactor materials), which currently limit the operational lifespan within the reactor [17]. Additionally, the use of liquid lead introduces further technological hurdles, primarily concerning corrosion, erosion, and chemical control of lead, as well as core integrity studies, instrumentation, and inspection techniques, along with the reliability of lead recirculation pumps [18]. The most advanced solutions currently under study or in experimental phases include the implementation of lead oxidation control techniques, the development of specialized metal alloys, and/or the application of protective coating layers at the lead interface, all of which are considered promising candidates for effectively addressing these challenges [14][19][17].

2.1.4 ALFRED

Concept of the ALFRED project

Among the many LFR design solutions and models studied worldwide, the one called “ALFRED” – Advanced Lead Fast Reactor Demonstrator – is considered the reference one at European level [14][19][23]. Its Research and Development (R&D) action is currently maintained and supported by an international consortium made by Italian (Ansaldo Nucleare and ENEA), Romanian (RATEN), and Belgian (SCK CEN) Organizations [20]. To date, the ALFRED’s R&D roadmap aims to establish a research infrastructure (RI) being built and to be built in Romania, as well as complementing the existing European facilities. The RI, covers all experimental aspects necessary to achieve the highest levels of Technology Readiness Level (TRL) for the LFR technology [17]. The guiding concept of the project is the ALFRED reactor itself, that is foreseen to be built in Romania around ~2040: an innovative nuclear reactor designed to demonstrate the revolutionary potential of LFR technology and subsequently support the safe and sustainable operation of future reactors [18][21]. ALFRED is therefore of fundamental importance and must be conceived based on criteria and specifications derived from the project’s objectives, rigorously designed to integrate safety and flexibility, and fully qualified for its implementation [9][11]. It is underlined that the ALFRED’s design, specifications and operational stage’s approach are currently under review: this means that the information reported in the subsequent paragraph shall be intended as purely indicate and subject to changes in the near future. Furthermore, these potential changes are expected not to impact the validity of the work performed in the present study [20].

ALFRED Design

The inspiring vision of the ALFRED project translates into a set of ambitious objectives, with the ALFRED reactor as its central element. The reactor design embodies this vision, guided by high-level criteria, with safety as the primary focus and demonstrative capabilities as the main objective [14][19][23]. ALFRED’s safety approach follows the guidelines of the Generation IV International Forum and aims to eliminate any possibility of radiological release that could pose a threat to the population and environment [9][11].

The demonstrative goal is twofold:

1. To serve as a demonstrator/precursor of the Generation IV LFR concept.

2. To act as a prototype for a small modular reactor (SMR) based on LFR technology for near-term deployment [20].

These objectives are further supported by additional safety and demonstration criteria, from which more specific criteria for option selection and design are derived [17].

To achieve these objectives simultaneously, the reactor's sizing has been linked to the Staged Approach for the demonstrator, allowing the system to operate under different conditions, starting from low power and low temperature and gradually processing to the operating conditions expected for a commercial reactor. This process is supported by the reactor itself, which provides scientific evidence and operational experience to justify safe operation to regulatory authorities [24]. Table 1 outlines ALFRED's operating conditions under the Staged Approach[20].

	Stage 0	Stage 1	Stage 2	Stage 3
	Commissioning	Low Temperature	Medium Temperature	LFR prototype
Core inlet temperature (°C)	390	390	400	400
Core outlet temperature (°C)	390	430	480	520
Core thermal power (MW)	0	100	200	300
Live steam pressure (bar)	—	170	175	180
Live steam temperature (°C)	—	420	435	450

Table 3: ALFRED Staged Approach in operation.

General overview of the reactor

The first ALFRED design originated from early studies conducted within the European LEADER project. Since then, it has undergone several revisions to incorporate scientific advancements and optimize the plant configuration from a thermohydraulic perspective [19][20].

The overall architecture of ALFRED's Reactor Cooling System (RCS) follows a pool-type design with an azimuthal periodicity of 120° [17][13]. The hot lead from the core outlet, located in the central area of the inner vessel (IV), is extracted by three symmetrically arranged reactor cooling pumps (RCPs) and discharged into an upper annular region known as the hot pool (HP) [18][20]. From there, the lead flows through three symmetrically arranged steam generators (SGs), where it is cooled by transferring heat to the power conversion system under normal conditions or to the primary decay heat removal system (DHR) in accident scenarios [17][7].

Upon exiting the steam generators, the lead descends into a second plenum known as the cold pool (CP). In parallel with the SGs, three emergency heat exchangers, called dip-coolers (DCs), are connected to a redundant and diversified passive decay removal safety system (E-DHR) [19][20]. An internal structure (IS) separates the hot pool and the cooling pumps, ensuring the integrity of the primary components. The IS is equipped with a baffle, which prevents the immediate return of lead to the core by forcing it to rise vertically, pass through openings at the top of the baffle, and descend into the annular gap between the IS baffle and reactor vessel (RV) [17]. Upon reaching the plenum at the bottom of the RV, the lead passes through the radial support of the inner vessel (IV) before entering the core [17].

The pool-type configuration establishes a physical separation between the hot and cold regions of the reactor, minimizing the amount of lead at maximum temperature and preventing its direct contact with the RV [19][13]. The fluid motion is forced multiple times to descend and ascend within the reactor, creating a predominant flow in each region of the Reactor Cooling System, engaging the entire lead mass, maximizing its effective thermal capacity, and preventing stagnant regions [18][20]. The perforations in the IS baffle prevent thermal stratification and hot spots in the upper regions near the cover gas (CG), ensuring uniform temperature distribution both under normal forced circulation operation and under accidental natural circulation conditions [17].

The entire Reactor Cooling System is enclosed within a safety vessel (SV), which ensures that in the event of an RV failure, the lead level remains above the active core region and the connection sections, thereby guaranteeing natural circulation for core cooling [20][7].

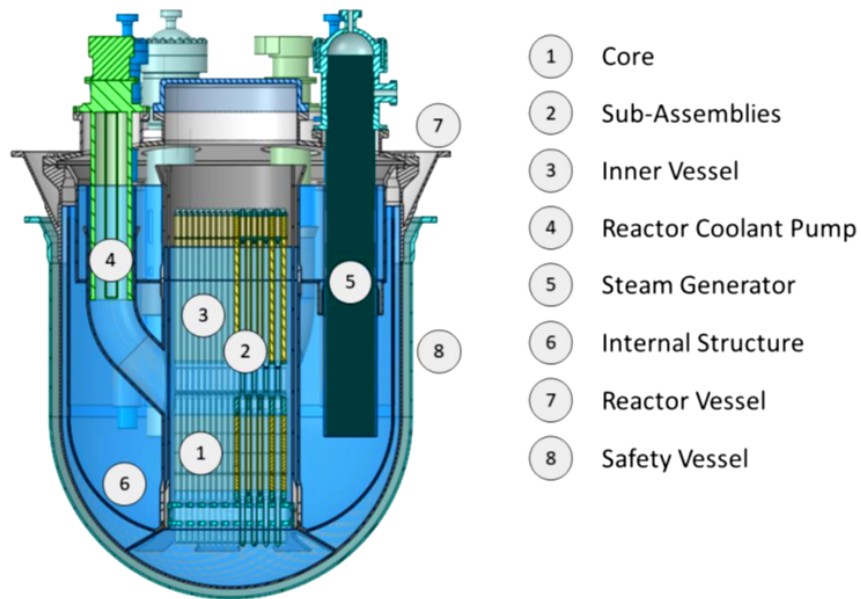


Figure 5: General system architecture of the ALFRED reactor coolant system. The figure shows the geometric configuration of some of the major components of the RCS together with the internal structures that guide the motion of the fluid.

Reactor Vessel

The reactor vessel (RV) has a cylindrical shape with hemispherical bottom. The upper section is connected via a Y-junction to the reactor support ring through a conical skirt that supports the entire weight of the RCS, including the reactor cover. All internal components are attached to the cover through standard circular flanges. The cover is bolted to the RV flange and sealed [19][20].

A truncated cone is designed to be welded to the hemispherical bottom, serving as a radial constraint for the internal structure. AISI 316 LN (or AISI 316 L9) is considered the preferred material due to its good compatibility with the coolant [17][18]. The RV has no nozzles below the free lead level (all penetrations are through the cover). The RV is designed for a minimum operational lifetime of 40 years, with a maximum expected operating temperature not exceeding 400°C [19][20]. It is here just specified that, thanks to this limit in operating temperature, it is sufficient to apply proper oxygen control strategy to protect materials from lead corrosion, thus preventing the need for coatings the materials [17].

Feasibility studies are currently underway to define the most suitable strategy for manufacturing, transporting and delivering the RV and SV, which represent the reactor's largest components [20].

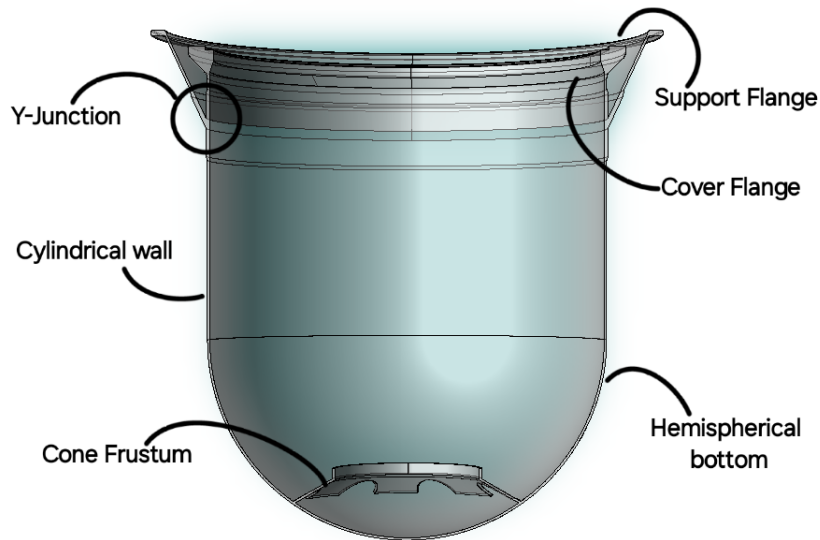


Figure 6: Cutaway of the ALFRED reactor vessel.

Internal Structure

The internal structure (IS) directs fluid flow, separates hot and cold regions, and houses other key components, ensuring sealed connections and allowing their removal if needed. The IS is supported by the conical trunk and connected to the reactor vessel flange at its interface with the reactor cover [17][19].

Since replacing the IS would require complete disassembly of the Reactor Coolant System, it is designed to withstand Stage 3 conditions and is not classified as a safety component. Consequently, periodic inspections requiring component extraction are not necessary [20].

The connection between the IS and main equipment, such as steam generators (SGs) and reactor coolant pumps (RCPs), is achieved through hydraulic or mechanical seals. These seals allow relative movements due to temperature differences and facilitate component replacement [17].

The IS is designed for a lifespan of at least 40 years. To protect against lead corrosion, in addition to oxygen control, a coating strategy using Al_2O_3 is planned. The coating will be applied through chemical vapor deposition (CVD) or pack cementation (PC). Given that the IS is not easily removable, the coating must be applied from the start of operations (Stage 0) [17][18].

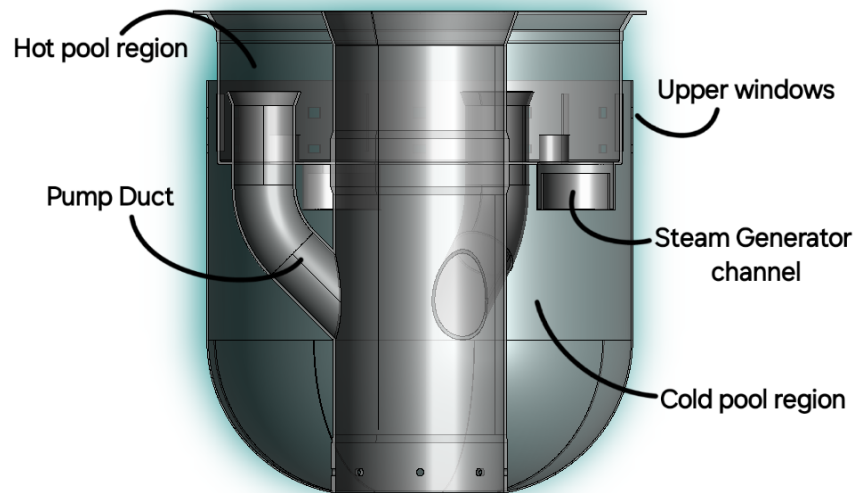


Figure 7: Cutaway of ALFRED internal steel structures.

Core and Fuel Handling

The Staged Approach poses a challenge for core design: one of the key criteria is having a single core configuration suitable for all operational phases of ALFRED. Additionally, the need to protect mechanical structures from the corrosive effects of lead increases as the coolant temperature rises[17][13].

- Stage 1: No additional protection strategy is required beyond oxygen control.
- Stage 2: The cladding will be coated with Al_2O_3 using pulsed laser deposition (PID).
- Stage 3: Coatings will be applied to all core surfaces due to the higher operating temperatures [17].

The core consists of fuel assemblies (FAs), control rods (CRs), safety devices (SDs), a test assembly, and a dummy assembly. It is housed within the inner vessel (IV), which supports and constrains it. The IV can be extracted after removing all sub-assemblies (S/As). The same corrosion protection considerations as for the internal structure apply to the IV, but its design lifetime is reduced to approximately 20 Years to neglect irradiation effects [17][19].

A diagrid (core support plate) ensures the correct positioning and support of all S/As and contributes to flow distribution. The coolant enters the fuel elements through holes in the lower part of a “spike” and flows through a bundle of fuel pins enclosed in a hexagonal tube (wrapper). Each FA contains 126 fuel pins arranged in a triangular lattice, with a central position reserved for additional in-core instrumentation [23].

The fuel selected for ALFRED is mixed uranium-plutonium oxide (MOX). The cladding and structural materials of FAs are made of a specialized austenitic stainless steel, Austenitic Improved Material 1 (AIM1). A high burnup of up to 100 MWd/kgHM¹ is expected. In later operational stages, the cladding and eventually all FA structures, will be coated with Al₂O₃ [17][19].

At the core center, a dedicated in-pile test section is reserved for irradiation qualification of coated FAs during Stages 1 and 2 or for advanced FA designs during and after Stage 3. Around the active region, 102 dummy assemblies are positioned [17].

The core is completed by 12 control rods (CRs) and 4 safety devices (SDs):

- CRs consist of absorber pin bundles that enter the core from the bottom, using boron carbide enriched in ¹⁰B as the absorber material.
- SDs provide a diversified and redundant shutdown system, with highly enriched boron carbide and the absorber. The absorber can enter the core via two mutually exclusive passive insertion mechanisms, both leveraging buoyancy for bottom-up insertion [19][13].

The transfer of FAs between the external environment and the RCS is performed using specially designed flask, ensuring the safe movement of both fresh and irradiated fuel while keeping it submerged in a lead inventory [17].

¹A burnup quantifies how much energy is extracted from a given amount of nuclear fuel. Therefore, MWd stands for Megawatt-days (a measure of energy produced) and kgHM stands for Kilograms of Heavy Metal (the initial mass of fissile/fertile material, such as uranium and plutonium)

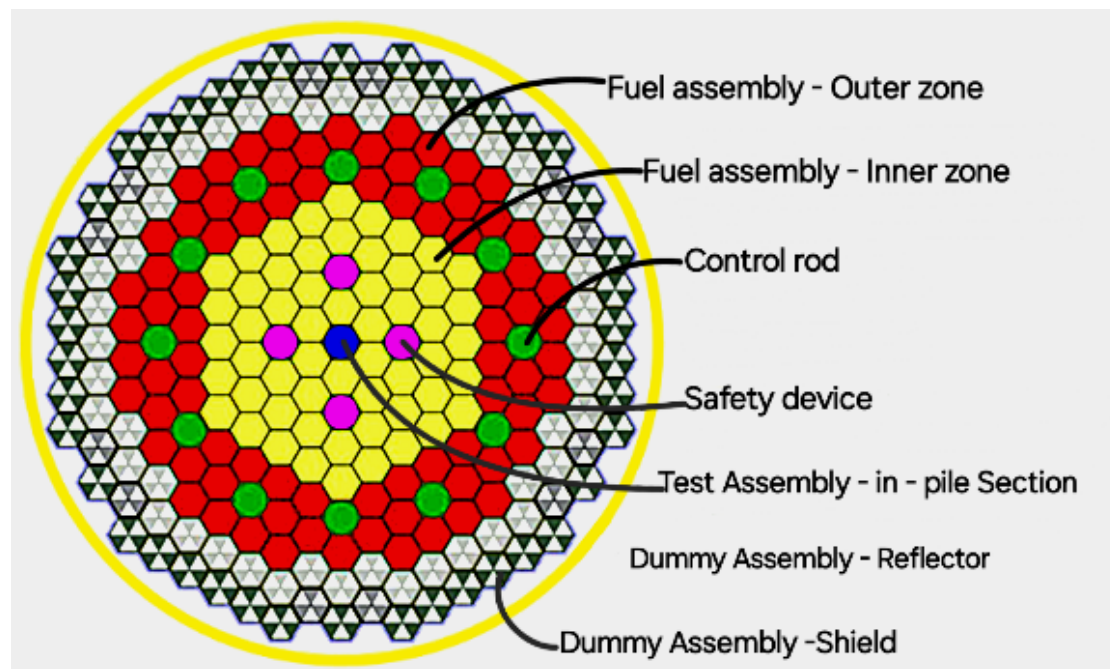


Figure 8: Simplified section of ALFRED core.

Steam Generators and Power Conversion System

The steam that transfers thermal energy to the Power Conversion System (PCS) interfaces with the Reactor Coolant System (RCS) through three bayonet tube bundle Steam Generators (SGs), symmetrically immersed in the primary pool. SG concepts based on bayonet tubes have been studied and experimentally tested. Initially, the option of double-wall tubes was considered, but it was later abandoned in favor of single-wall tubes, with the containment function entrusted to the Internal Structure baffle [19][17]. Table 2 provides relevant data on the ALFRED SGs, specifically regarding its operation in Stage 2. The material selected for Stages 1 and 2 is AISI 316L, while for Stage 3, coatings or new corrosion-resistant materials are to be qualified. Figure 9 illustrates some details of the SG [20].

Parameter	Value	Unit
Number of SGs	3	—
Number of tubes (each)	880	—
Primary side temperatures (inlet/outlet, Stage 2)	480/400	°C
Primary side (Lead) mass flow rate	5615.2	Kg/s
Secondary side temperatures (inlet/outlet, Stage 2)	335/425	°C
Secondary side (water) mass flow rate (Stage 2)	44.3	Kg/s
Material (Stage1 and 2)	AISI 316L	—

Table 4: A table with 3 columns and 7 rows

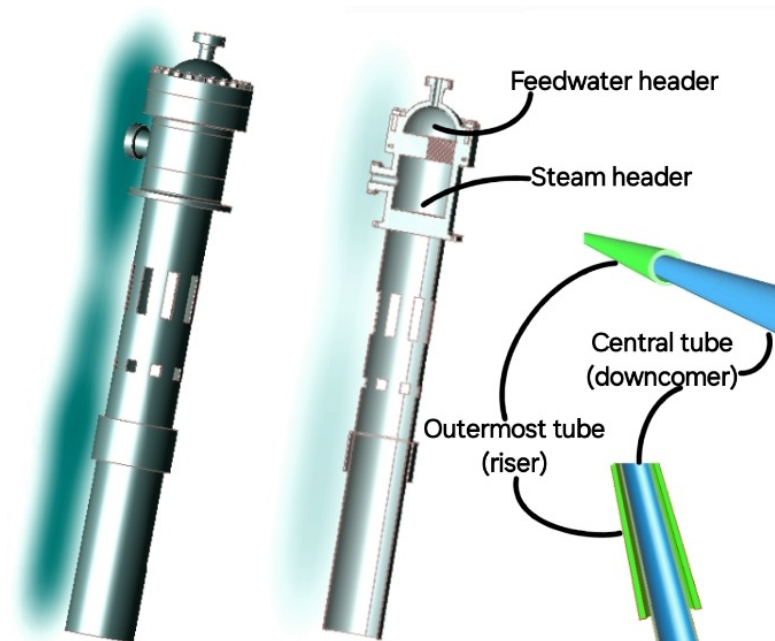


Figure 9: View (left), cross-section (middle) and details of the ALFRED steam generator.

Reactor Coolant Pumps

The Reactor Coolant Pumps (RCPs) are currently under design, leveraging experience gained from operational experimental facilities. The RCPs are housed within an IS duct connecting the core outlet plenum to the Hot Pool (HP) and are exposed to the high temperatures of the hot Lead. Protection methods against the corrosive and erosive attack of molten Lead are therefore required. Their installation in the IS ducts ensures ease of extraction. The design incorporates the critical requirements of low hydraulic resistance when the impeller is locked, facilitating natural circulation in accidental conditions. The RCPs are bolted to the reactor cover using standard circular flanges and are equipped with an inverter-driven motor. Table 3 presents key data on the RCPs. The main material used is AISI 316L or AISI 321H, with protection ensured through aluminization by diffusion [17][13][20].

Parameter	Value			Unit
	Stage 1	Stage 2	Stage 3	
Nominal flow rate	1908			m ³ /h
Nominal head	1.5			m
Minimum/maximum flow rate	900/1980			m ³ /h
Lead velocity (max/bulk)	10/2			m/s
Bulk material	AISI 316L or AISI 321H			—
Lead protection mean	Aluminization by diffusion coating			—
Design lifetime	5	5	20	years
Rotational speed	289			rpm
Hydraulic efficiency	73			%
Power supply	108.15			kW
Motor supply	200			kW

Table 5: Main data of the ALFRED reactor coolant pump.

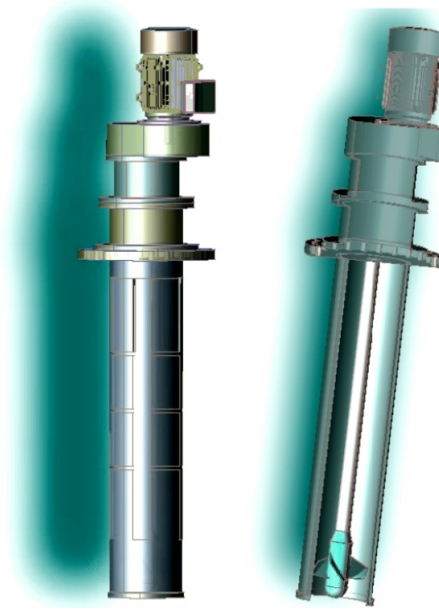


Figure 10: View (left) and cross-section (right) images of the ALFRED coolant pump.

2.2 Main characteristics of the fission chambers

2.2.1 Generic fission chambers

Fission chambers are specialized neutron detectors that provide real-time measurements of neutron flux. They specialize in the monitoring and control of nuclear reactors, ensuring safe and efficient operation. [5][25].

A generic fission chamber is composed of two coaxial electrodes where at least one electrode, generally the inner one (anode) is coated with fissile or fertile materials² from a few micrograms to few grams. The chamber is generally filled with a pressurized inert gas at few atmospheres, typically argon at 1.5 bar, to minimize secondary ionization and parasitic contributions and to avoid gas escaping out of the chamber. The inter-electrode gap can be from tens of microns to few millimeters. When the neutrons interact with the nuclei of the fissile deposit atoms, they likely undergo fission generating two heavily charged ions emitted in two almost opposite directions [25][26].

²Fissile isotopes, like ^{238}U and ^{239}Pu , are the ones that undergo fission with low-energy (thermal) neutrons, thus sustaining fission chain reaction. Fertile isotopes, like ^{235}U and ^{232}Th , do not undergo fission when interacting with low-energy neutrons but can be converted into fissile materials through neutron absorption.

One product stops either in the fissile layer or in the chamber wall, the other exits from the deposit and ionize the fill gas along its trajectory, creating electron-ion pairs. The range of direct current applied should be high enough to collect all the charges and low enough to avoid secondary ionization. If these conditions are met, the fission chamber can act like an ionization chamber operating in the saturation regime, and so its signal, i.e., the counting rate, is proportional to the fission rate and consequently to the neutron flux. In this situation, the signal becomes dependent only on the chamber characteristics and the ambient flux while almost insensitive to the applied voltage [5][27][28]. The gamma photons, that directly ionize the filling gas, also generate a signal whose suppression is one of the biggest concerns in the case of modeling of fission chambers [28].

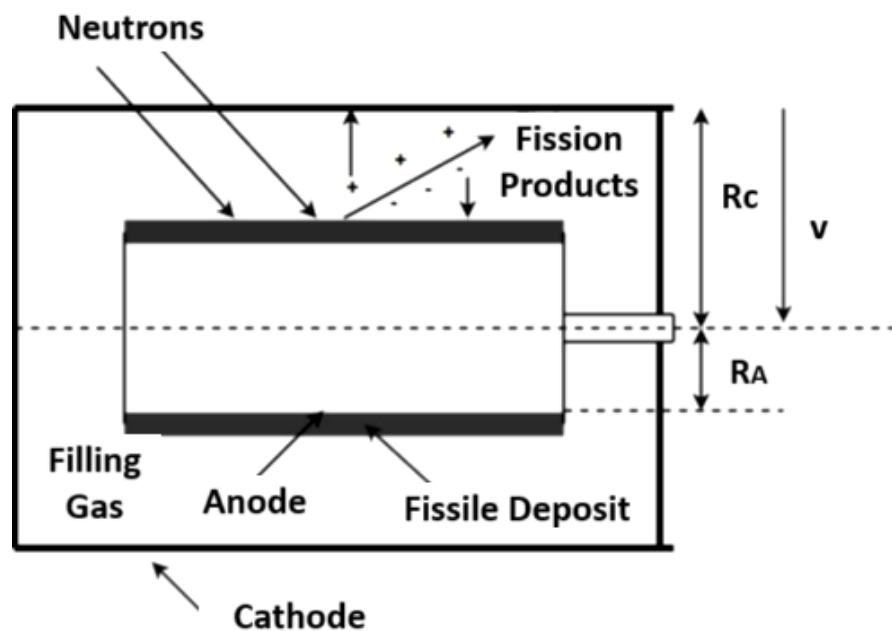


Figure 11: Fission chamber scheme in which the principal general characteristics are depicted.

Three modes of operation

A great advantage of fission chambers in case of use as in-/out-core instrument is that it facilitates the tracking of flux amplitude over a large dynamic range corresponding to about 15 decades of reactor operation. A fission chamber can be operated in three different modes, i.e., pulse, Campbelling (or Mean Square Voltage, MSV, or fluctuation), and current. These three modes constitute a wide dynamic range depending

on the neutron flux magnitude of the system and on the fission rate of the fissile material of the chamber[5][25][26].

At ambient low neutron fluxes, the fission rate is so low that each electronic pulse induced by a nuclear fission can be counted event by event. The event rate, being closely related to the fission rate, produces a signal which is a series of well separated pulses to trigger a counter, therefore, the fission chamber can operate in “pulse mode”. Monitoring a quantity proportional to the flux is much easier in this mode as the average delay between two pulses is much larger than the pulse duration. It is just about finding an optimum discriminator level to eliminate the background noise in the current pulse while measuring the counting rate [27][28].

As the neutron flux increases, the fission rate becomes sufficiently large that pulses inside the chamber overlap and can no longer be separated or processed event by event. This pile-up generated by the high fission rate calls for a current mode acquisition and the characteristics of the overall current needs to be measured in this case. According to the Campbell theorem, if the basic neutron detection process is Poissonian, the moments of this type of stochastic process depend on the event rate. In other words, the fission rate in this case is proportional to the first two statistical moments of current, i.e., average and variance. So, the “current mode” corresponds to the measurement of average current and the “Campbelling mode” corresponds to the current variance [28].

Current mode poses a challenge to neutron detection because it comes with significant gamma contribution (usually 1- 10% of the signal depending on the geometry) and allows no straightforward way for gamma discrimination. This mode is based on the first part of Campbell’s theorem which states the average value of the current from a random current pulse source is proportional to the average pulse rate and thus charge produced per event is proportional to the pulse height. To keep track of gammas in current mode sometimes a simultaneous irradiation of a deposit-less chamber is utilized.

The Campbelling mode (or Mean Square Voltage, MSV), representing the second moment or cumulant (variance), offers a much better discrimination against the gammas. In this mode the signal or the variance of the current is proportional to the average pulse rate and to the square of the charge produced per event which in turn is related to the square of the pulse height. The average number of charge pairs created by a single fission product is much larger than that produced by a single gamma ray. Thus, the measurement of the variance of the detector current suppresses effectively the contribution of the low-amplitude gamma-induced pulses if a suitable bandwidth is chosen. The Campbelling mode is of much interest not only for noise reduction from the signal, but also for signal processing over a wide measurement range of 10 – 15 decades and taking advantage of higher order statistics to extract additional information on the de-

tection process quality [5][27][25][26].

2.3 Fission chambers Suitable for LFR applications

The instrumentation for measuring neutron flux available worldwide is primarily designed for thermal neutrons since most power reactors are Light Water Reactors (LWRs), where the monitored neutron energy spectrum is dominated by the thermal contribution. Consequently, the technical specifications of neutron monitors generally relate to measuring particle fluxes within a thermal spectrum. When monitoring neutron fluxes with varying energy spectra, the instrument's performance within their specific experimental setup should be evaluated through direct measurements, corrective calculations, or simulations. This paragraph discusses the state of the art in neutron instrumentation for measuring fast neutron fluxes in high-temperature environments, *i.e.*, the main characteristics of the LFR, based on manufacturer-provided data for thermal spectra [29][25][28].

Beyond the chemical aggressiveness of lead, temperature—approximately 420°C under nominal operating conditions for the in-core applications—represents the primary challenge for neutron instrumentation, limiting both technological and commercial feasibility. The necessity to withstand accidental conditions, where temperatures may exceed the operational limits of neutron probes—with current high-temperature fission chambers reaching a maximum of 600°C—further complicate the issue [17][5][28].

Fast reactors exhibit neutron fluxes at full power that are two orders of magnitude higher (10^{16} n/cm² s compared to 10^{14} n/cm² s) than those in thermal reactors, necessitating instrumentation capable of covering a broader neutron flux range, from zero to nominal power. The most critical challenge arises at the extremes of this range: an insufficient neutron population at startup, leading to signals below detection threshold (blind window), and excessive neutron bombardment near nominal power, which could rapidly degrade the sensitive material. In such cases, shielding or repositioning may be needed [26][28].

A single instrument is rarely sufficient; however, certain fission chambers can cover up to 15 decades of neutron flux by combining their different operating modes. Considering this premise, neutron instrumentation can be categorized into three groups based on the reactor power range [5][25]: Start-up range ($10^2 - 10^6$ n/cm² s): predominantly gamma background; neutron detector operates in pulse mode. Intermediate range ($10^6 - 10^{12}$ n/cm² s): comparable gamma and neutron background levels; detectors function in pulse mode with compensated chambers or in Campbell mode. Power range ($10^{12} - 10^{16}$ n/cm² s): negligible gamma background; detector operates

in current mode without the need for gamma discrimination. A lead-cooled fast reactor (LFR) requires continuous in-core monitoring due to its large dimensions and high enrichment levels, making radial and axial internal mapping essential for reactor analysis safety. Given the operating conditions of LFRs, several manufacturers of fission chambers (Centonic, Photonis, etc.) offer models potentially applicable to the ALFRED reactor. Table 4 presents the characteristics extracted from the technical specifications for measuring a thermal spectrum that will be updated for the specific neutron spectra of potential ALFRED installations using the procedure described later [28][29].

Model	Max operating Temperature (°C)	Sensitivity		Dimension (mm)	
		Pulse[cps/nv]	current[A/nv]	diameter	length
CFUC06	600	1.0	2×10^{-13}	48	412
CFUE24	400	1×10^{-2}	1×10^{-15}	7	150
CFUE32	600	1×10^{-3}	1×10^{-16}	7	150
CFUF43	350	—	1×10^{-17}	4.7	86
CFUR43	350	—	3×10^{-18}	3	42
CFUZ53	350	—	5×10^{-18}	1.5	49
CFUR64	400	8×10^{-6}	9.2×10^{-19}	3	42

Table 6: Reference Photonis fission chamber characteristics commercially available, applicable to the reactor ALFRED.

As previously mentioned, fission chambers can operate in pulse mode, Campbelling mode, and current mode, depending on the neutron flux level.

- Pulse mode is used for low neutron populations, and inherently discriminates against gamma and alpha background radiation. However, high gamma fluxes can interfere with the electronics and reduce the maximum count rate measurable without losing proportionality. The referenced Photonis fission chambers support a maximum gamma dose of 10^4 Gy/h.
- Campbelling mode and current mode are typically used in reactors with high neutron fluxes, where pulse mode operation is no longer feasible. The main challenges in Campbelling and current mode are related to the significance of the current signal, which can be affected by interference such as:
 - Alpha current: gas ionization due to alpha particles emitted by the fissile layer.
 - Gamma current: indirect gas ionization caused by photons from the reactor or the decay of fission products in the fissile layer (which increases with burn-up).

- Leakage current: ohmic losses in the insulator (typically alumina, Al_2O_3), which worsen significantly with temperature (at 600°C , leakage can be 10^4 times higher than at 20°C) [28][27].

There is a low threshold for a useful current signal, above which the current is proportional to the fission rate and neutron flux. An upper limit is determined by the increase in charge density in the gas, which may cause anode shielding effects and loss of proportionality. These limits depend on geometry, applied voltage, chamber sensitivity, and electronics. Table 5 provides the neutron flux ranges for Pulse Mode and Current Mode in the previously mentioned fission chambers [29].

Model	Neutron Flux Range(nv)		Gamma Flux
	Pulse Mode	Current Mode	
CFUC06	$1 - 10^5$	$10^4 - 10^{10}$	$< 10^{-8} - 10^{-7}$
CFUE24	$10^2 - 10^8$	$10^8 - 10^{12}$	$< 10^{-8} - 10^{-7}$
CFUE32	$10^3 - 10^8$	$10^9 - 10^{13}$	$< 10^{-8} - 10^{-7}$
CFUF43	–	$10^{10} - 10^{14}$	$< 10^{-8} - 10^{-7}$
CFUR43	–	$10^{11} - 1.5 \times 10^{14}$	$< 10^{-8} - 10^{-7}$
CFUZ53	–	$2 \times 10^{11} - 10^{14}$	$< 10^{-8} - 10^{-7}$
CFUR64	$10^6 - 10^{11}$	$10^{12} - 10^{15}$	$< 10^{-8} - 10^{-7}$

Table 7: Neutron flux ranges (nv stands for thermal neutron flux in $\text{cm}^{-2} \text{s}^{-1}$) for the Photonis fission chambers in pulse and current modes present in Table 4.

An ideal fission chamber should cover all neutron flux decades through different operating modes. However, optimizing for one mode may compromise performance in others. A significant issue is gas pressure: pulse and Campbelling modes require high pressure, whereas current mode requires lower pressure. A potential solution, alternative to the use of different fission chamber models, could be a single “dual-pressure” chamber with two separate sections [25][5][29].

Performance Calculation of Instrumentation Applicable in ALFRED

The neutron characteristics of fission chambers, as reported in Table 4, refer to the measurement of a thermal neutron spectrum. In Light Water Reactors (LWRs), detector primarily monitor thermal neutrons regardless of their location, affecting only the magnitude of the measured response but not the efficiency or sensitivity of the instrument. In fast reactors, however, the average energy of the neutron spectrum can vary significantly between the reactor core center and its periphery. Consequently, the detector sensitivity is no longer constant (as in LWRs) because the average cross-section

of the reactor used for neutron detection changes with energy. As a result, the detector's sensitivity and response are intrinsically linked to its installation location. To correct neutron sensitivity values and update them for installation conditions in ALFRED, a correction factor has been calculated based on the spectrally weighted average cross-section of the local neutron spectrum:

$$\int_E \phi(\mathbf{r}, E) \cdot \sigma_i(E) dE = \int_E p(\mathbf{r})\psi(E) \cdot \sigma_i(E) dE \sim \bar{\sigma}_i(\mathbf{r}) \int_E p(\mathbf{r})\psi(E) dE \quad (1)$$

where:

- $\phi(\mathbf{r}, E)$ represents the local neutron flux as a function of energy E and position \mathbf{r}
- $\sigma_i(E)$ is the microscopic cross-section of the reaction of interest for energy E
- $p(\mathbf{r})$ is a spatial weighting factor related to the neutron distribution
- $\psi(E)$ is the spectral shape factor of the neutron spectrum.

The problem can be formalized by considering that the generic detector response (R) is proportional to both the magnitude ($p(\mathbf{r})$) and the spectrum ($\psi(E)$) of the local neutron flux:

$$R \propto \bar{\sigma}_i(\mathbf{r}) \int_E p(\mathbf{r})\psi(E) dE \quad (2)$$

By considering two positions with the same flux magnitude but different energy spectra (thermal and fast), and taking their ration, we obtain the Energy Spectrum Correction Factor (ESCF):

$$\begin{cases} R_{\text{thermal}} \propto \bar{\sigma}_i(\mathbf{r})|_{\text{thermal}} \int_E p(\mathbf{r}) \psi(E)|_{\text{thermal}} dE \\ R_{\text{fast}} \propto \bar{\sigma}_i(\mathbf{r})|_{\text{fast}} \int_E p(\mathbf{r}) \psi(E)|_{\text{fast}} dE \end{cases}$$

$$\text{ESCF}(\mathbf{r}) = \frac{R_{\text{fast}}}{R_{\text{thermal}}} = \frac{\bar{\sigma}_i(\mathbf{r})|_{\text{fast}} \int_E p(\mathbf{r}) \psi(E)|_{\text{fast}} dE}{\bar{\sigma}_i(\mathbf{r})|_{\text{thermal}} \int_E p(\mathbf{r}) \psi(E)|_{\text{thermal}} dE} = \frac{\bar{\sigma}_i(\mathbf{r})|_{\text{fast}}}{\bar{\sigma}_i(\mathbf{r})|_{\text{thermal}}} \quad (3)$$

If we consider that $\bar{\sigma}_i(\mathbf{r})|_{\text{thermal}}$ refers to factory test conditions with thermal neutron ($\bar{\sigma}_i(\mathbf{r})|_{\text{thermal}} = \bar{\sigma}_i|_{\text{thermal}}$), the equation becomes:

$$\text{ESCF}(\mathbf{r}) = \frac{\overline{\sigma}_i(\mathbf{r})|_{\text{fast}}}{\overline{\sigma}_i(\mathbf{r})|_{\text{thermal}}}. \quad (4)$$

Using Equation 4, the sensitivity of the probe to fast neutron fluxes ($S|_{\text{fast}}(\mathbf{r})$) can be derived from the sensitivity to thermal neutron fluxes ($S|_{\text{thermal}}$) through the following relation:

$$S|_{\text{fast}}(\mathbf{r}) = S|_{\text{thermal}} \cdot \text{ESCF}(\mathbf{r}) \quad (5)$$

The ESCF value that can be used in the specific application for the ALFRED reactor was evaluated through Monte Carlo simulations in previous work available from literature. In this work, the ESCF value was calculated using the MCNPX code, where the numerator is obtained from an input deck of the ALFRED reactor for a specific position \mathbf{r} , and the denominator is computed separately for a Maxwell-Boltzmann thermal neutron spectrum at T=293K (Figure 12).

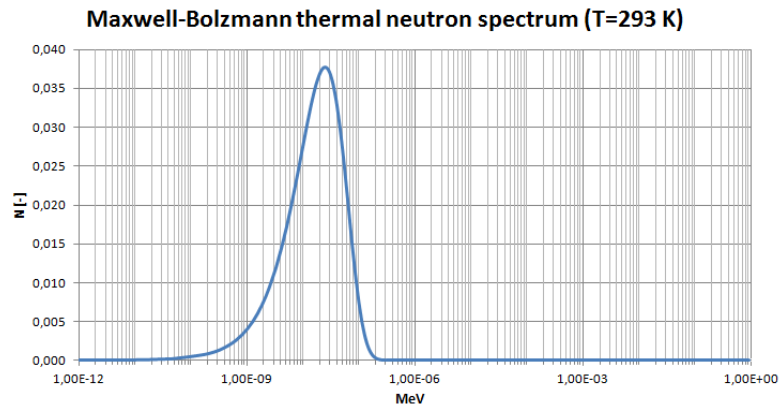


Figure 12: Thermal spectrum used for the estimation of the correction factor in Equation 4.

This method provides a preliminary sensitivity estimate without requiring a detailed device model in MCNPX, a complex process that demands experimental tuning. The updated sensitivity along with the local neutron flux magnitude, allows for an assessment of stress conditions, aging effects (burn-up), and an estimate of device lifespan.

Therefore, with the values found with Equation 5, the expected electrical response can be evaluated as follows:

$$R|_{\text{fast}}(\mathbf{r}) = p(\mathbf{r}) \cdot S|_{\text{fast}}(\mathbf{r}) \quad (6)$$

and the estimated probe lifespan ($t(\mathbf{r})$) can be obtained by dividing the updated fluence threshold by the local neutron flux, as described by:

$$t(\mathbf{r}) = \frac{E_{\text{th}}}{\text{ESCF}(\mathbf{r}) \cdot p(\mathbf{r})} \quad (7)$$

However, additional factors such as gamma dose limits must also be considered. Despite the simulation providing preliminary evaluations, it is essential to validate the selections through experimental measurements [29].

3 Methodology

The determination of neutron and photon distribution outside the Reactor Vessel and their characterization was done through Monte Carlo method by using a demo version of the TopMC code developed by FDS [30]. The methodology aimed to define a model specifically targeted at assessing the applicability of fission chambers in the presence of gamma radiation. It was structured on modeling and simulation, ensuring a progressive refinement of the quality of the results obtained. The overall approach was based on three main inputs³:

1. The Monte Carlo “ALFRED Core Model”, already available and ready to be run from previous works [31] (“input 1” in the following);
2. The 3D model of the ALFRED Reactor Vessel and Inner Structures (“input 2” in the following);
3. The fission chambers data sheets (“input 3” in the following).

The methodological approach adopted for modeling and characterize the neutron and photon distributions within the ALFRED Reactor was developed in a systematic and modular manner, as illustrated in the diagram in Figure 13. The main flowchart is the yellow-highlighted one; on each step of it, secondary flow diagrams follow, describing the methodology in more detail. A brief description of the main flowchart is reported below, whereas further details as well as descriptions of the secondary ones are provided in the following sub-sections.

³Details on the inputs are reported in Appendix I.

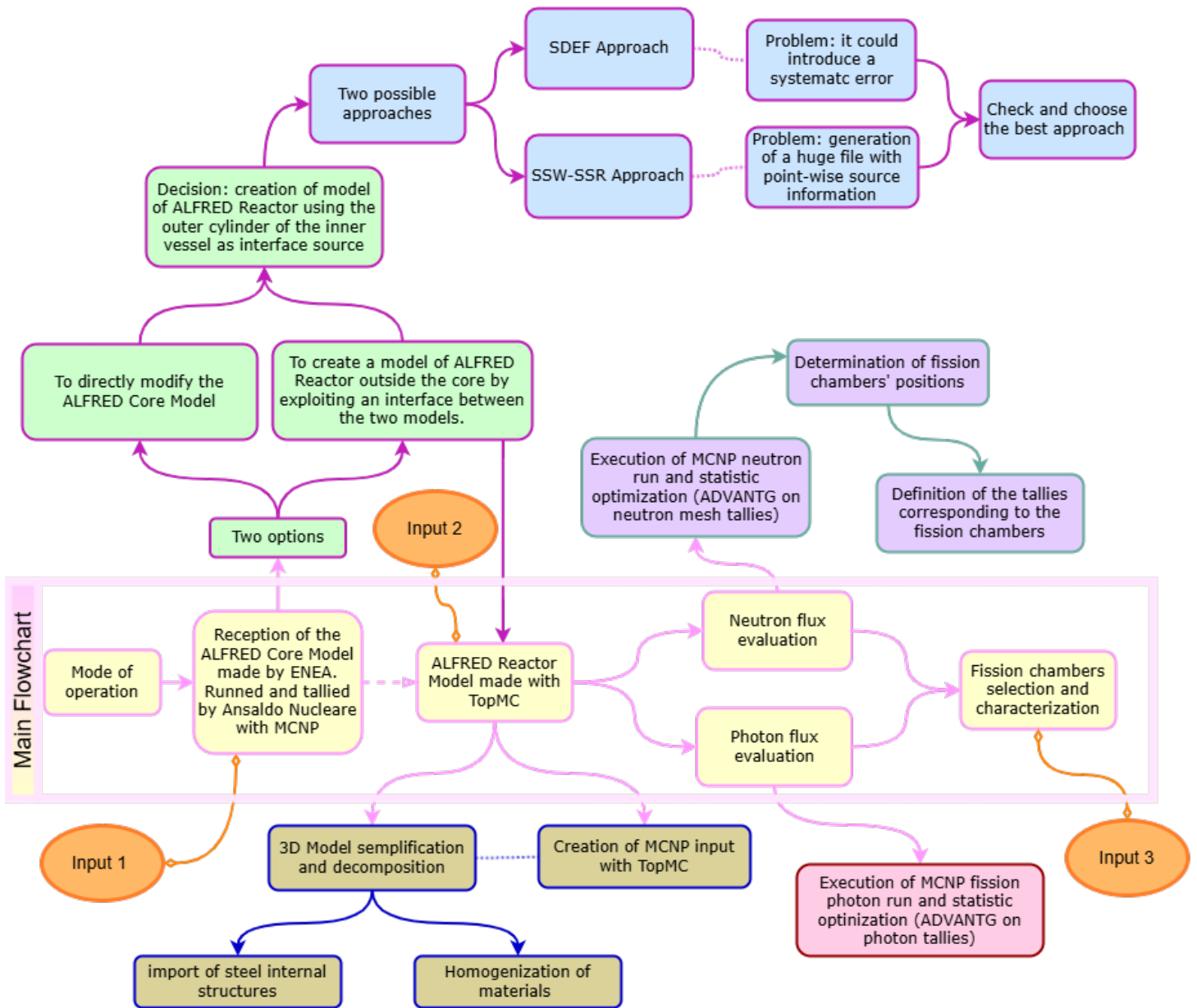


Figure 13: Scheme of the methodology.

In the initial phase, the reference model of the ALFRED Core only (input 1), developed by ENEA and ready for the MCNP Monte Carlo code [32], was considered. It has detailed definition of the core elements (e.g., fuel and control/safety bars), thus providing realistic simulation of both fission's neutrons and photons. It was tallied and run by Ansaldo Nucleare through MCNP, so that the corresponding neutron and photon spectra could be characterized in the present work. At the same time, an analysis of the

reactor's mode of operation was carried out, essential for correctly setting the operational conditions of the simulations.

Subsequently, it became necessary to integrate in the analysis the geometry of the ALFRED's Internal Structures and Vessels, being not available in the ALFRED Reactor Core model. To do so, it was decided to perform creation of the corresponding Monte Carlo geometrical model (to be subsequently run with TopMC to propagate the fission's neutrons and photons throughout the vessel's outer region) applying the so-called "Monte Carlo CAD importing capability" which is available through well-known computer codes like McCad/Salome [33] or TopMC itself – both were successfully studied, tested and used in the present work. This process was based on the set of 3D CAD models of ALFRED Reactor Vessel and Inner Structures (input 2), and required preliminary steps of model simplification, decomposition, components' homogenization as well as careful handling of materials, and interfaces to preserve the essential physical representation while avoiding excessive computational complexity.

Both (1) the integration of the ALFRED's Internal Structures and Vessels in the already available Monte Carlo ALFRED's Core Model or (2) the creation of a new Monte Carlo model with these structures were in principle doable. Since, as explained below in subsection 3.1.1, the latter was pursued, the definition of the corresponding interface source represented a central phase of the work, during which two alternative approaches in turn were explored for setting the initial particle conditions. The final choice considered the advantages and disadvantages of both in order to mitigate potential systematic errors and time consumption.

As the Monte Carlo input dataset was completed, TopMC simulations were launched for the analysis of neutron fluxes/spectra in various locations close to the external surface of the ALFRED's Safety Vessel. Particular attention was devoted to the definition of tallies corresponding to the positions of the fission chambers to accurately estimate their response to different radiation components.

In parallel, the evaluation of the photon fluxes/spectra in the same locations, considering the components arising from fission processes, made possible the subsequent selection and characterization of the fission chambers best suited to the expected operational conditions, based on the information available from input 3.

It is important to specify that all the results obtained and reported in the present work are normalized in the hypothesis that ALFRED Reactor is running at 100 MWth. It should be emphasized that all the absolute quantities reported (neutron fluxes, fission rates, and so on) are directly proportional to the thermal power of the reactor and

therefore can be trivially scaled to any reference thermal power desired.

3.1 Modeling Approach

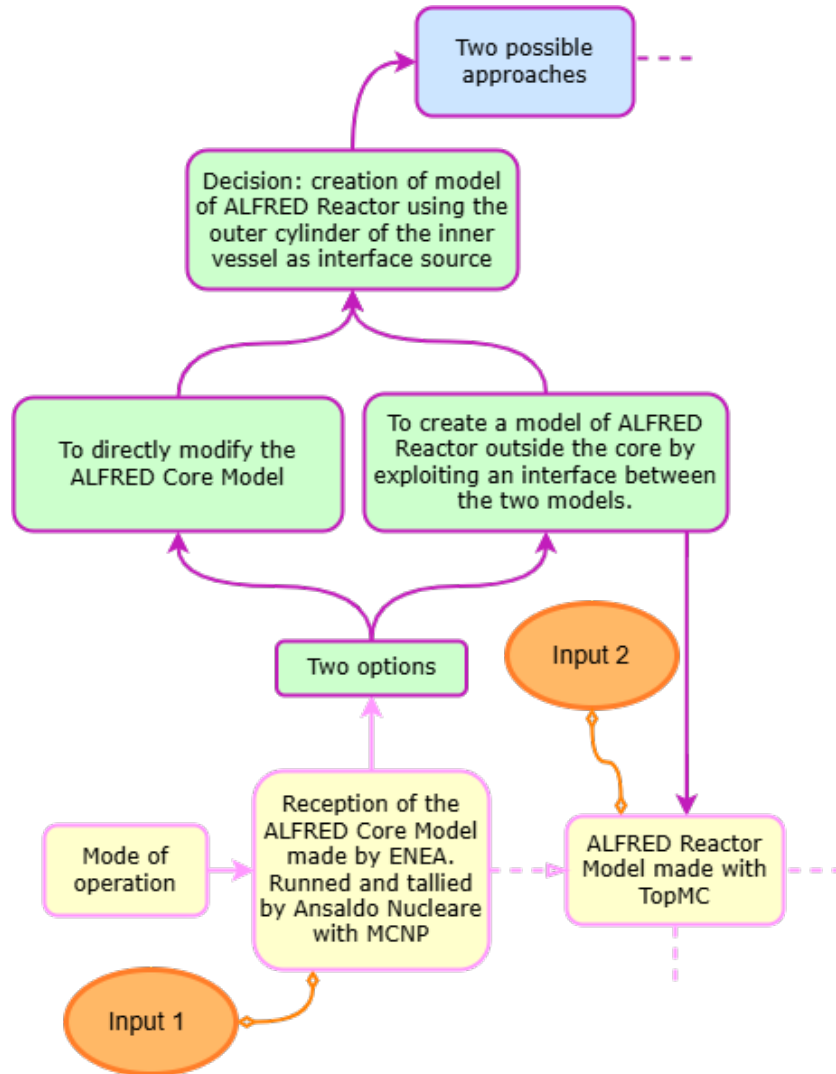


Figure 14: Modelling approach scheme.

Given the complexity and level of detail of the ALFRED Core Model developed by ENEA, it was necessary to identify an efficient method for integrating the Internal Structures and Vessels in the Monte Carlo model without compromising the coherence of the simulations.

To this end, two alternative strategies were considered for integrating the structures located outside the inner vessel:

- **Direct modification of the “ALFRED Core model”:**
This approach involved incorporating the additional structural components into the existing model, directly modifying the original geometry external to the core. Accordingly to this option, a single coherent structure would be ensured, avoiding the need to manage interface (i.e., source term) between the two different models. But, it would increase the geometric and computational complexity. Furthermore, modifying a validated model could compromise the quality and reliability of the results.
- **Development of a new model with a source interface (the “ALFRED Reactor Vessel model”):**
The alternative involved the construction of a new model from scratch representing only the outer shell of the inner vessel. This would require creating an interface source with the ALFRED Core model.
Under this alternative, the integrity of the original ALFRED Core Model is preserved, allowing the definitions of internal geometries to remain unchanged. Additionally, it enabled a more modular simulation management, facilitating future modifications or adjustments. Conversely, it required a preliminary phase of interface development and validation, ensuring a physically accurate correspondence between the two domains.

In light of these considerations, the decision was made to proceed with the new “ALFRED Reactor Vessel model” in order to minimize the impact on the ALFRED Core Model and increase the flexibility of the analyses.

This methodological choice proved particularly effective, allowing for a structured and controlled integration of the sources and optimizing computational time, while maintaining a high degree of accuracy in the representation of the physical phenomena under investigation.

The creation of the simplified interface laid the groundwork for the next stage of the study, focused on managing the initial conditions of the particles and carrying out the simulations. In particular, it became necessary to clearly define the operational method of the source and to establish an effective procedure for the propagation of neutron and photon fluxes through the computational domains.

In conclusion and summary, since it was decided for the present work to built from scratch the new ALFRED Reactor Vessel model, a two step approach was applied in

terms of Monte Carlo simulations:

- Step 1: Monte Carlo simulation (made by Ansaldo with MCNP) of the ALFRED Core Model, providing the information on fission's neutrons and photons at the interface with the new ALFRED Reactor Vessel model. In the present work, this output information was analyzed and properly prepared as source term for the next Step 2;
- Step 2: Monte Carlo simulation (made entirely for the present work with TopMC) of the ALFRED Reactor Model, evaluating the fission's neutrons and photons fluxes/spectra in the potential locations of the fission chambers outside the ALFRED Safety Vessel.

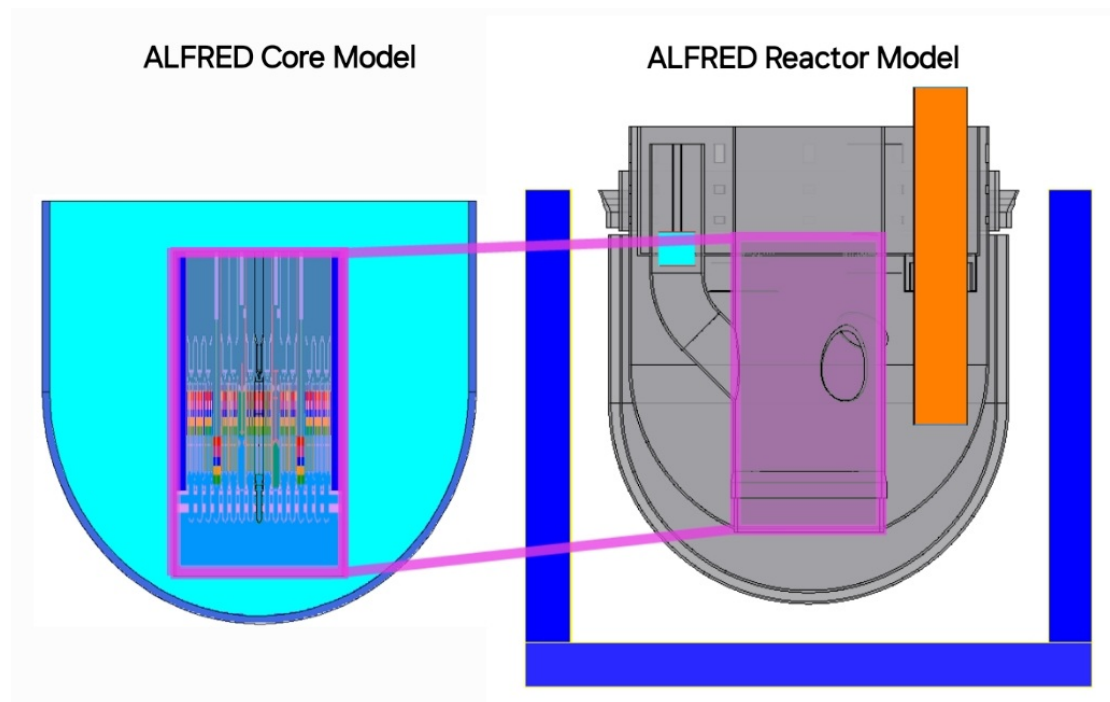


Figure 15: Interface identification in both the ALFRED Core Model and the ALFRED Reactor Model (Courtesy of ENEA and Ansaldo Nucleare).

3.1.1 Source definition

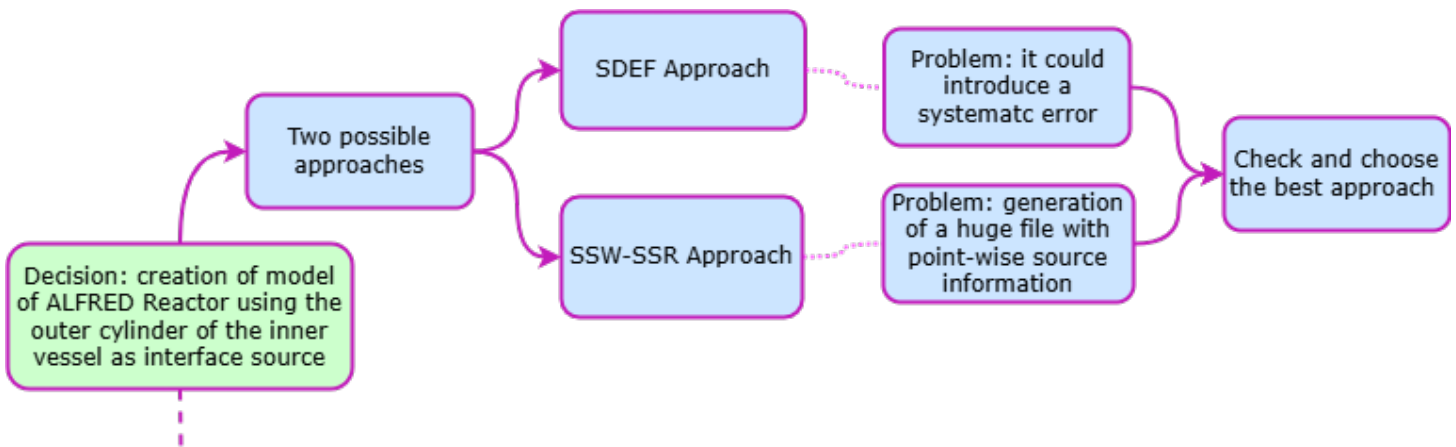


Figure 16: Scheme for the Source definition process.

Because of the need for the definition of the source interface between the ALFRED Core model and the new ALFRED Reactor Vessel model, the focus shifted to identifying the most appropriate methodology for setting the initial particle conditions (i.e., the source specification) for the TopMC simulations.

In this context, again, two alternative approaches were considered, considering the capabilities of the Monte Carlo codes in defining the source terms:

- **SDEF Approach:**

This technique implicated the definition of a fission neutron and photon current tally (F1 tally [34]) coincident with the external cylinder of the inner vessel in the ALFRED Core Model, and the definition of a correspondent cylindrical SDEF source [35] in the ALFRED Reactor Model. This method allowed the depiction of a source geometry, positioned at the interface between the two models, that aimed to reproduce the expected spatial and directional characteristics of the neutron and photon flux leaving the core.

The cylindrical SDEF approach was implemented by assigning a source surface with axial symmetry, defined by a radius, height, and axial position compatible with the exit boundary of the detailed core in the ALFRED Core Model. For the neutron analysis, the SDEF was implemented with an axial subdivision of 60 cm pitch (see Figure 17), while for photon analysis, no axial segmentation has been performed. The parameters used for the source geometry were calibrated to reflect the physical dimensions of the interface surface.

In addition to the spatial configuration, the source description included a detailed

energy spectrum for neutrons and photons, derived from the MCNP runs conducted on the ALFRED Core Model. These reference simulations were used to extract the angular and energy distributions of the particles at the interface, which allowed the cylindrical source to reproduce, with reasonable accuracy, the spectral content of the emitted radiation.

Among the advantage of this approach, the most notable is the ease of definition of the source term which is simple to modify, making it suitable for parametric studies or sensitivity analyses. However, some limitations emerged during the validation phase. In fact, as a limitation of the MCNP code, the SDEF card allows the definition of distribution for just one of the two polar angles (i.e., the zenithal angle). Therefore, a homogeneous distribution is defined on the azimuthal angle by default. Since it does not necessarily reflect reality, the simplification of the angular and spatial emission profiles may lead to systematic errors in the final results. Furthermore, the user-dependent definition of the energy binning in the F1 tallies can substantially influence the approximation of the interface energy spectra, thus constituting an additional and distinct source of systematic error.

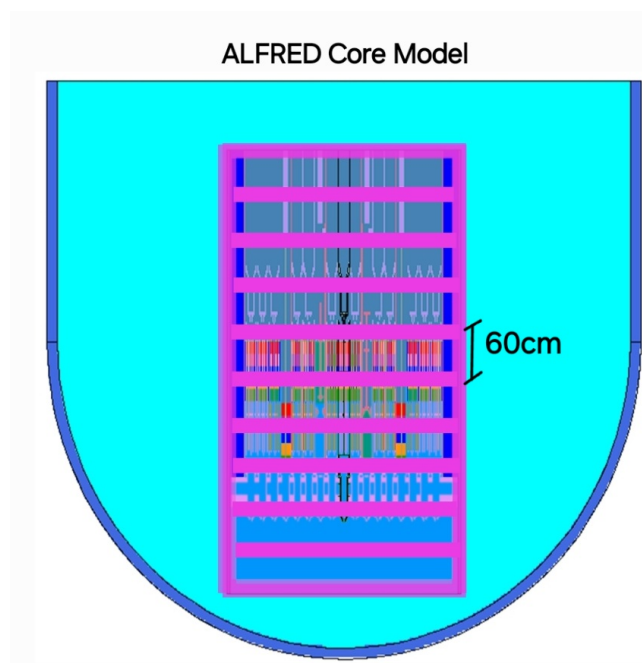


Figure 17: Scheme for the Source definition process (Courtesy of ENEA and Ansaldo Nucleare).

- **SSW-SSR Approach:**

This option is available in both the Monte Carlo codes (MCNP and TopMC) used

in the present work. It relies on the fact that, as an interface source is identified within the same Monte Carlo model and/or between different models, the point-wise information⁴ of each particle crossing the surface in the initial run is saved in a file that can be read in the subsequent run as source term. This method is called Surface Source Write (SSW) and Surface Source Read (SSR), respectively [36].

In order to ensure a physically accurate and computationally robust representation of the radiation fields propagating from the reactor core to the external structures, this strategy consists of decoupling the simulation domain into two distinct but physically linked stages. In the first (i.e., SSW) simulation, the detailed ALFRED Core Model was employed to simulate the transport of neutrons and photons up to the predefined boundary surface located at the interface between the core and the external domain. At this interface, all particle tracks crossing the surface were recorded in an SSW file.

Subsequently, in the second simulation in the ALFRED Reactor Model, the previously generated SSW file is used as source term via the SSR card, effectively restoring the exact spatial, energetic, and directional distributions observed at the core boundary. The SSR definition ensured a faithful continuation of the transport process without the need to approximate particle source properties. Anyway, this method is not without challenges. The generation and management of the SSW file can lead to large data volumes, especially in high-fidelity simulations. Furthermore, file handling and statistical convergence require thoughtful planning: particle histories captured in the SSW file must be sufficient in number and diversity to avoid introducing statistical bias in the downstream simulation.

Taking into consideration all the positive and negative aspects of these two options, the actual choice between the two is postponed in the chapter of the Results, after the data analysis and the evaluation of the systematic error introduced by the SDEF Approach. If the systematic error results significant, the option of choice would be the SSW-SSR Approach otherwise, the SDEF Approach would be preferred, chiefly because less time- and data-consuming.

⁴This includes comprehensive information on the particles' position, energy, direction and type at the moment of crossing, thus capturing the full phase space of crossing particles.

3.2 Reactor model simplification and input creation

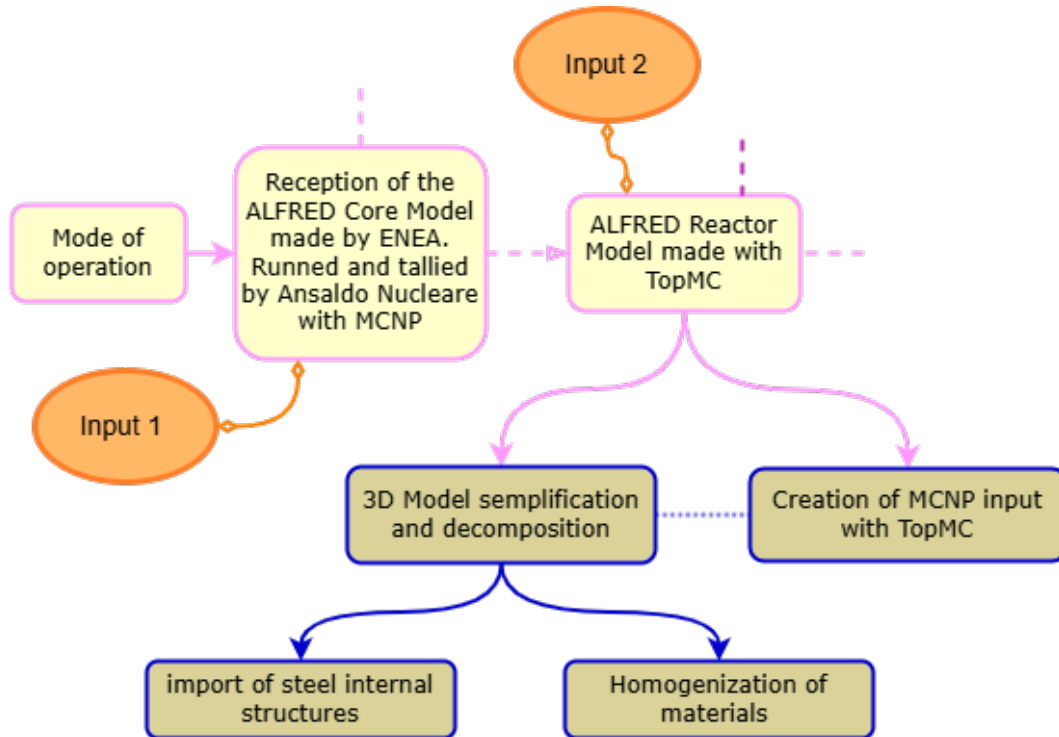


Figure 18: Scheme of the process for the ALFRED Reactor Model simplification and input creation.

As already anticipated previously, given the complexity of the ALFRED Core Model and the computational burden associated with high-fidelity neutron and photon transport simulations, a new ALFRED Reactor Vessel Model was created from scratch through CAD-importing approach for Monte Carlo codes. A set of systematic simplification, decomposition and component homogenization processes were carried out to enable the integration of the core with its surrounding environment. This phase was essential to ensure compatibility between the reactor model and the available computational resources, while maintaining an adequate level of physical fidelity for the study's objectives.

The starting point for this activity, as it is reported above, was the reference geometry of the ALFRED Core Model, developed by ENEA and validated by Ansaldo Nucleare through Monte Carlo simulations. While the core region was retained in its validated configuration, modifications were introduced to represent the structures located outside the inner vessel in a simplified yet physically consistent manner.

The ALFRED Reactor Model has been modelled in two stages. The first step consisted in the CAD importing of the realistic steel (AISI 316L) internal structures (i.e., the Inner Vessel, the Reactor Vessel, the Safety Vessel, and all the empty tubes that normally host the other components of the reactor); this was done consistently both with Salome/McCAD's as well as with the TopMC's dedicated Graphical User Interface.

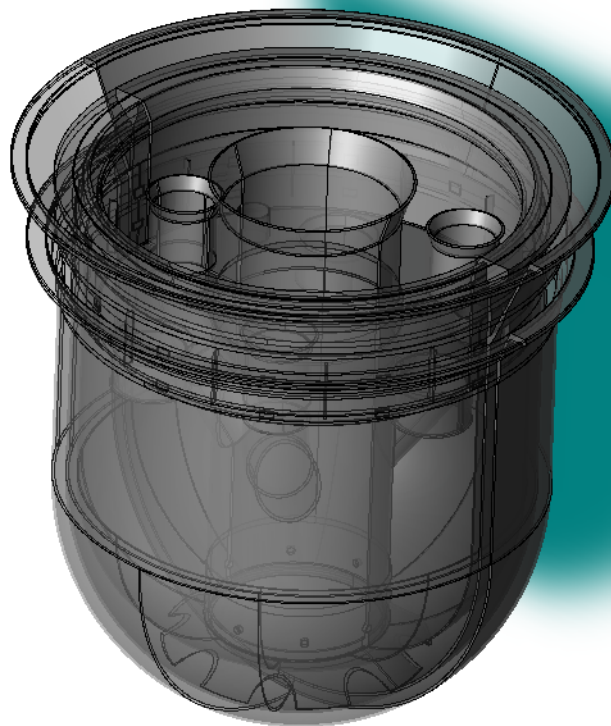


Figure 19: ALFRED Reactor Model with the CAD imported parts.

Attention was paid to the simplification process of the 3D CAD model, primarily focused on preserving key structural features and material distributions that significantly influence radiation transport, while removing excessive detail not essential for global flux estimations. Such modifications were implemented with caution to avoid introducing geometric artifacts that could lead to spurious neutron leakage or artificial flux discontinuities. Moreover, it was decided to simplify the model definition of some fine-gained geometric elements with homogenized representations: namely, this was done for the Steam Generator, the Pump Propeller, and the Deep Coolers. After the analysis and data taking from existing models of the components with both McCAD/Salome and

TopMC visualizers, the best way to model them was:

- Steam Generator: A cylinder filled with a homogeneous material composed of Lead, Steel, and Water/Vapor⁵.
- Pump Propeller: A steel hollow tube with a hollow cylinder filled with a homogeneous material of Lead and Steel⁶.
- Deep Coolers: they are not modelled because they would influence the radiation transport in the same way as the Steam Generator.

Finally, the shielding concrete has been also created to conclude the exterior of the reactor, so that eventual back-scattered radiation could simulate more realistically the neutron and photon fluxes/spectra. In parallel with the geometric simplification, a review of the material specifications was undertaken to align them with the simplified geometry. Where appropriate, materials were homogenized using volume-weighted averaging techniques, particularly in non-critical shielding regions. The neutron cross-section libraries were selected to match the temperature and composition of the original detailed model, ensuring consistent interaction probabilities.

Material cards were verified to preserve relevant physical properties such as hydrogen content (for moderation), density, and heavy metal composition, all of which are critical to the accurate simulation of neutron attenuation and photon production.

Finally it must be emphasized that, since the 3D input CAD model only has structural components, the definition of all the internal volume of the Reactor Vessel as created by both McCAD/Salome and TopMC is filled by void. Hence, as a final step, it was necessary to manually modify the Monte Carlo dataset to insert the lead material in this volume.

⁵Details about the calculations and results of them for the actual composition are reported in the Results chapter, Steam Generator section.

⁶Details about the calculations and results of them for the actual composition are reported in the Results chapter, Pump Propeller section.

3.3 Neutron flux evaluation

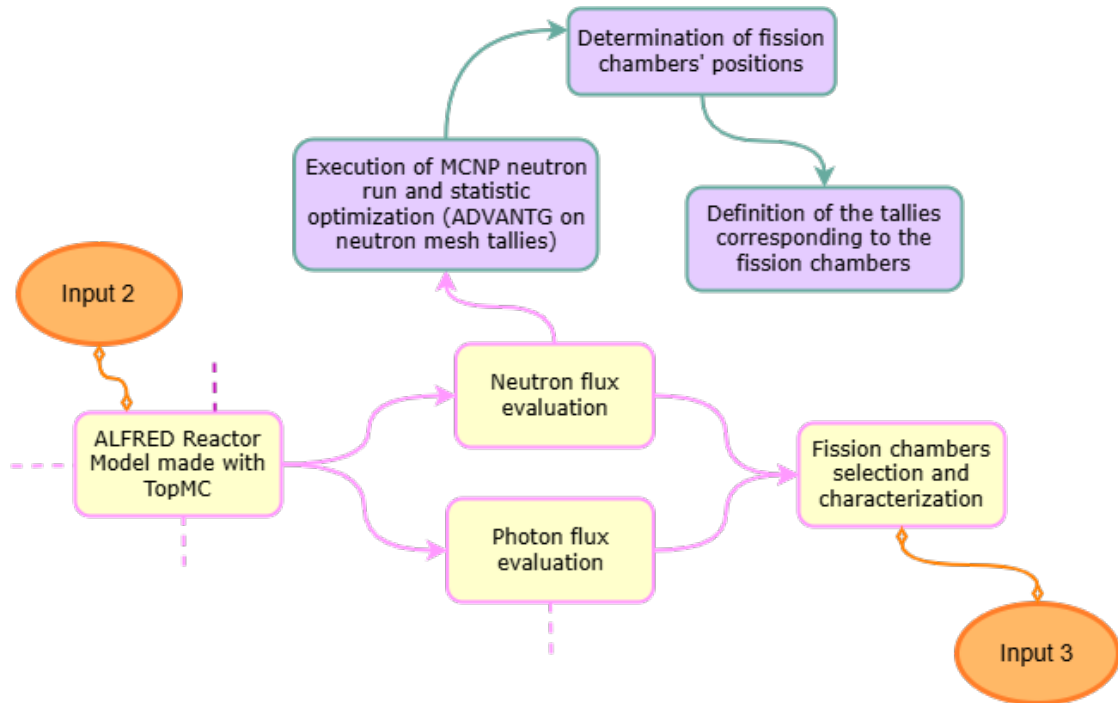


Figure 20: Neutron flux evaluation process scheme.

Following the completion of the source definition and the setup of the simulation geometry, the focus of the analysis shifted to the evaluation of the neutron flux within the external regions of the ALFRED Reactor, with particular emphasis on the locations designated for the installation of fission chambers. This phase aimed to accurately characterize the spatial and energetic distribution of the neutron field, in order to assess detector response and optimize positioning for monitoring purposes.

The Monte Carlo evaluation of the neutron flux was optimized in terms of statistics through the weight window variance reduction technique [37], which details are reported in Appendix II. This was performed by Ansaldo Nucleare using ADVANTG [38], and later used with TopMC as an input file for the final simulations, on neutron mesh tallies covering all the region of interest from the source to the tallied locations (i.e., the locations where the fission chambers are supposed to be placed).

In order to reduce the time needed to perform the variance reduction process with the ADVANTG calculations, the whole simulation domain of the ALFRED Reactor Model was divided into two parts with the optimization mesh tallies: the first one corresponding to an upper cylinder enclosing the upper part of the reactor up to a few centimeters

inside the concrete shielding, and the other one corresponding to a cylinder, covering the hemispherical part of the vessel as well as circumscribing the lower part of the reactor up to a few centimeters inside the concrete shielding.

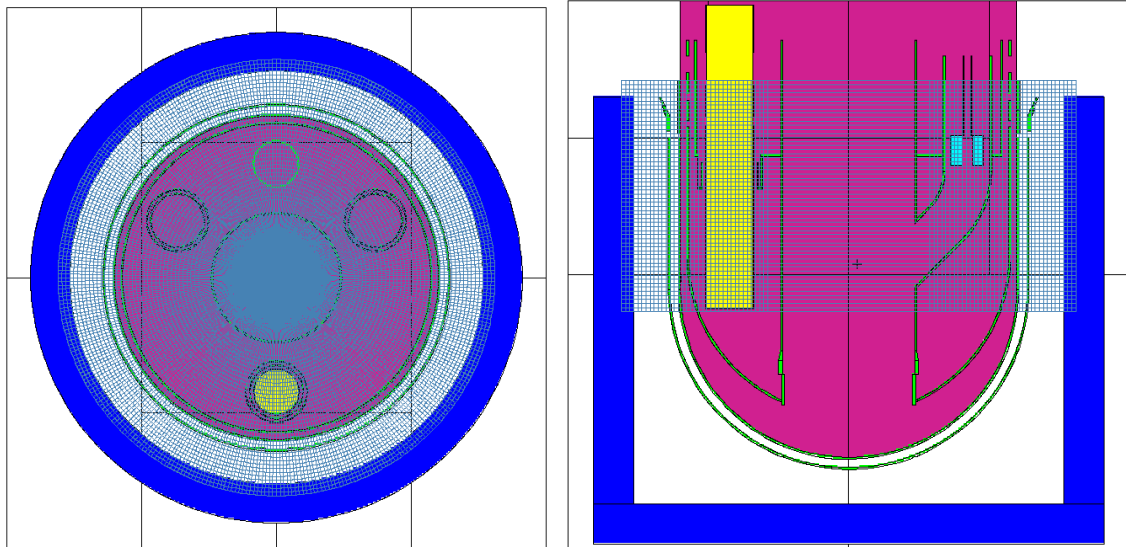


Figure 21: Upper mesh tallies of ADVANTG (Courtesy of Ansaldo Nucleare).

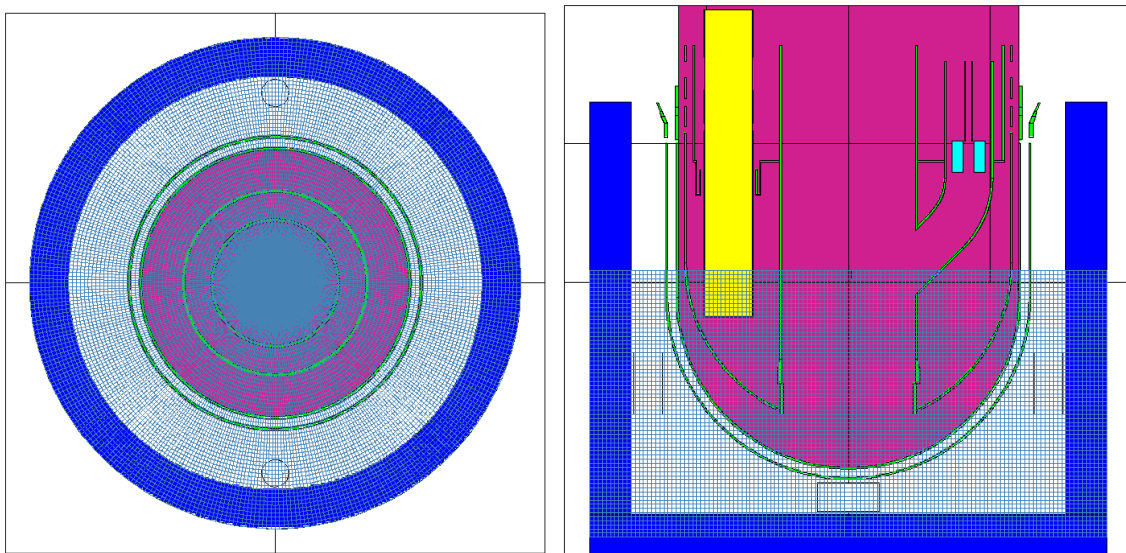


Figure 22: Lower mesh tallies of ADVANTG (Courtesy of Ansaldo Nucleare).

The placement of the fission chambers was carefully determined to ensure coverage

of all regions where significant variations in neutron flux were expected, while avoiding redundant instrumentation. A total of nine positions were selected based on their relevance to the reactor's structural and operational configuration. It is emphasized that, in order to limit to the scope of the present work, it was deemed unnecessary to define the geometry of the fission chambers in detail in the Monte Carlo model. In fact, it was decided that the only needed information was just on the neutron energy spectra, which can be simulated through the definition of cylindrical and void cells where the averaged energy spectrum can be evaluated with the track-length estimator tallies (F4 type⁷ [34]). All the tallies were defined within the annular region located between the safety vessel and the outer concrete shielding, thereby allowing effective monitoring of the external radiation field without being too exposed to the reactor heat. Specifically, F4 tallies were positioned along three vertical lines aligned with the core axis: one corresponding to the steam generator, another to the pump propeller, and a third intersecting only lead external to the core. Additional F4 tallies were placed under the bottom of the vessel, directly beneath the steam generator axis, and along the pump propeller axis at the same vertical level as the lowest detector. All the F4 neutron tallies were discerned in 100 logarithmic energy bins between 10^{-12} and 10^1 MeV. The Monte Carlo simulation was performed with the set of ENDF/B-VII.1 nuclear data libraries [39].

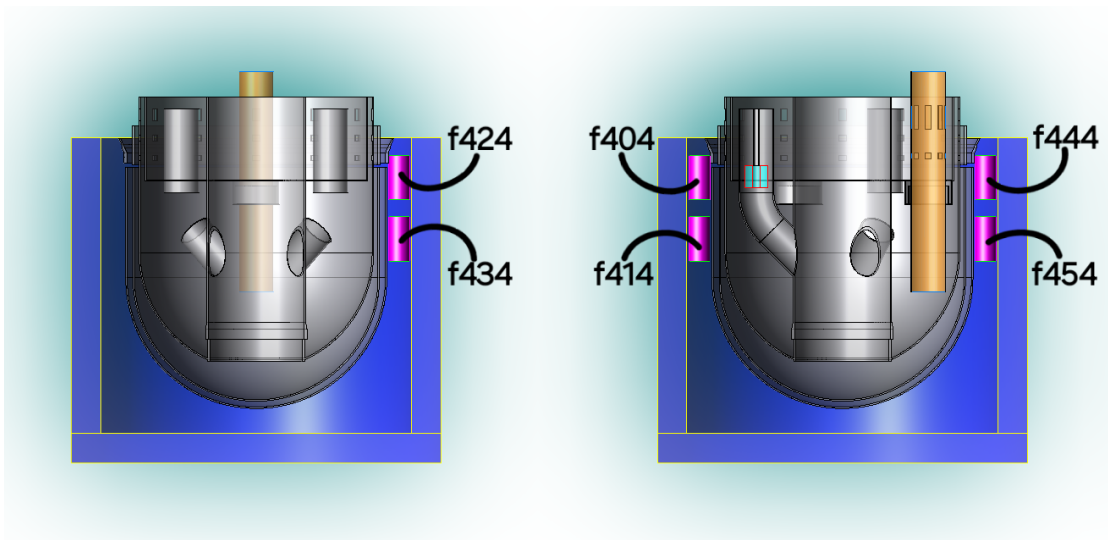


Figure 23: Fission chambers position in the upper part of the reactor.

⁷This means that the significant assumption made for the present work is that the presence of the real fission chamber's materials does not significantly impact on the local neutron energy spectra. Further assessments, not in scope of the present work, may be considered to properly verify it.

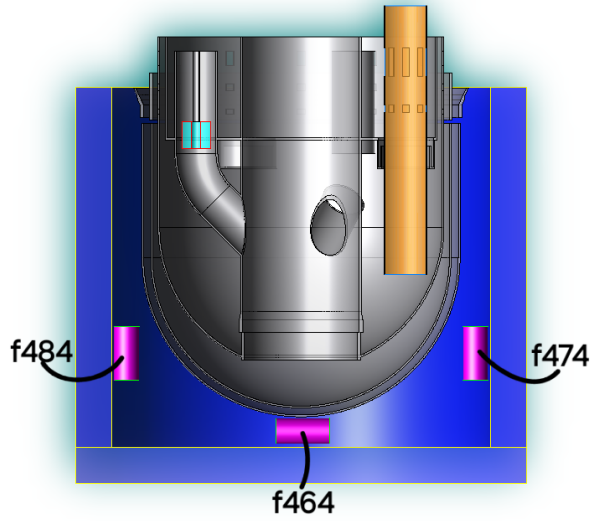


Figure 24: Fission chambers positions in the lower part of the reactor.

3.4 Photon flux evaluation

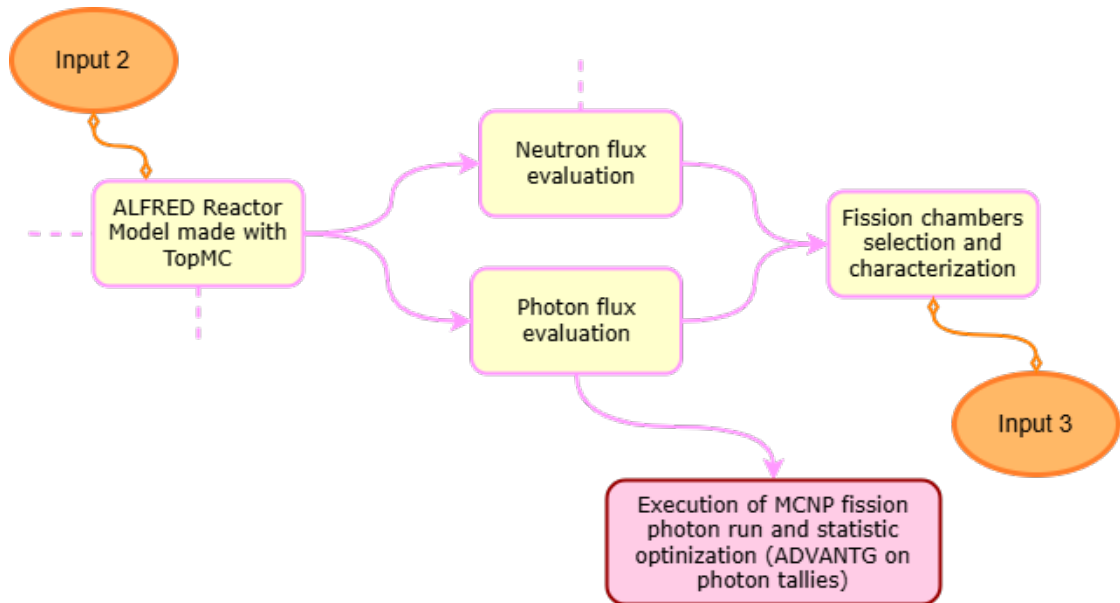


Figure 25: Photon flux evaluation process scheme.

Photon flux (and/or dose rate) represents the most important background contribution that may blind the fission chambers' response. In principle, photons come from 2

distinct sources: (1) direct (prompt) fission photons and (2) photons due to neutron activation of nearby materials – like, primarily, reactor safety vessel’s steel. In the present work, the focus was limited to fission photons only, since the evaluation of the activation photons usually requires more complicated techniques and/or other simulation codes than pure Monte Carlo ones⁸.

By experience and because of the lead’s high photon attenuation capability, it was a-priori suggested that the prompt fission photons give negligible contribution with respect to the natural background in all the suggested location of the fission chambers considered in the present work. To validate this sentence, it was decided to apply a very simplified simulation approach, again with the Monte Carlo method. A very simple model was created with TopMC, consisting of a parallelepiped-shaped (a slab) with a section equal to $20 \times 20 \text{cm}^2$ and a thickness conservatively equal to the shortest possible photon path through the lead. On one side of the slab, the photon source density evaluated as described in Section 3.1.1 was defined, so that the simulation dataset is representative of the real situation. The photon dose rate was evaluated on the other side of the slab with proper definition of F4 tally multiplier card [41]. It was deemed necessary to assess that the fission photon’s dose rate after the slab is below or equal to 10% of the background radiation level (i.e., approximately $10^{-8} - 10^{-7}$ Gy/h), thereby validating the initial suggestion.

⁸Although the presence, in the real case, of activation photons cannot be overlooked, it was decided to leave this evaluation to future research developments. These may rely, for example, on the so called “Rigorous Two Step Approach - R2S”, that can be done both with TopMC as well as with MCNP code coupling the latter with 0-dimensional activation codes.[40]

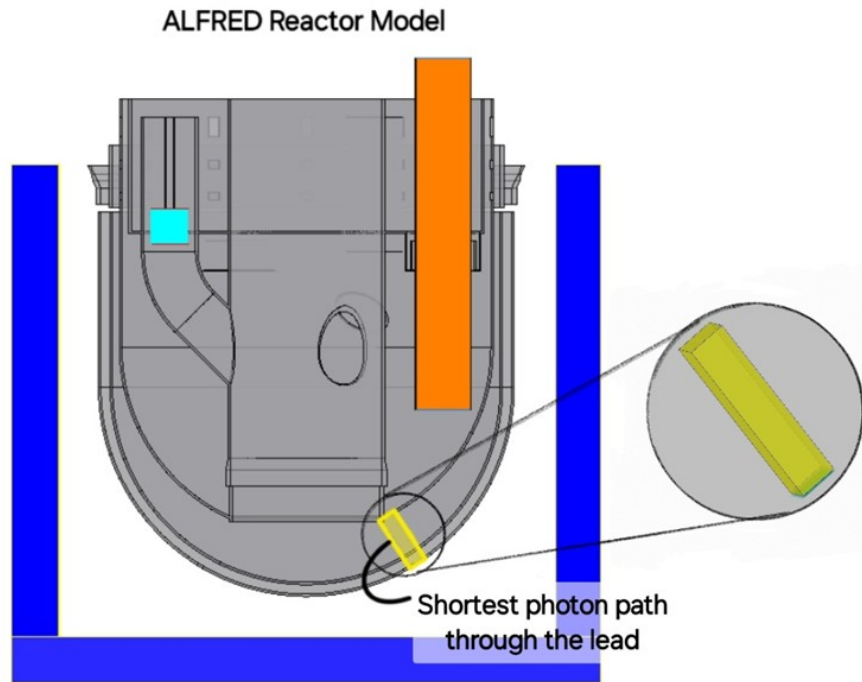


Figure 26: Alfred Reactor Model with the shortest photon path through the lead highlighted (left) and the volume of the second simulation (right).

3.5 Fission chambers characterization

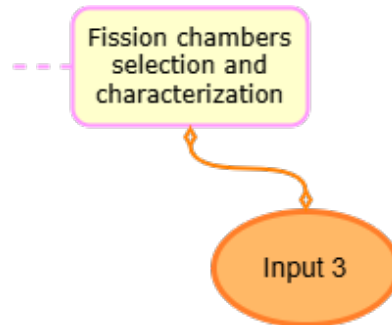


Figure 27: Characterization of fission chambers scheme.

As demonstrated in Section 3.4, the fission chambers do not exhibit a significant response to photon-induced signals, validating their exclusive sensitivity to neutrons in mixed radiation environments.

The analysis of neutron fluxes at the nine tally positions (Section 3.3) enables the determination of each chamber's operational mode based on the localized flux intensity.

Furthermore, these flux spectra, divided into 100 energy bins, allow for an accurate, energy-dependent calculation of the Energy Spectral Correction Factor (ESCF) at each position, as formalized in the first part of Equation 3:

$$\text{ESCF}(\mathbf{r}) = \frac{R_{\text{fast}}}{R_{\text{thermal}}} = \frac{\int_E \phi(\mathbf{r}, E) \cdot \sigma_i(E) dE|_{\text{fast}}}{\int_E \phi(\mathbf{r}, E) \cdot \sigma_i(E) dE|_{\text{thermal}}} \quad (8)$$

where, in first approximation we assumed the thermal energy interval as $10^{-12}\text{MeV} < E < 10^{-7}\text{MeV}$ and the fast one as $10^{-7}\text{MeV} < E < 10^1\text{MeV}$.

Endowed with this precise ESCF, the chamber sensitivities to both fast and thermal neutron spectra can be derived. The fast spectrum sensitivity via Equation 5:

$$S|_{\text{fast}}(\mathbf{r}) = S|_{\text{thermal}} \cdot \text{ESCF}(\mathbf{r}), \quad (9)$$

and the thermal spectrum sensitivity by referencing tabulated values provided in Appendix I.

This methodology ensures a rigorously qualified, spectrum-resolved characterization of fission chamber performance.

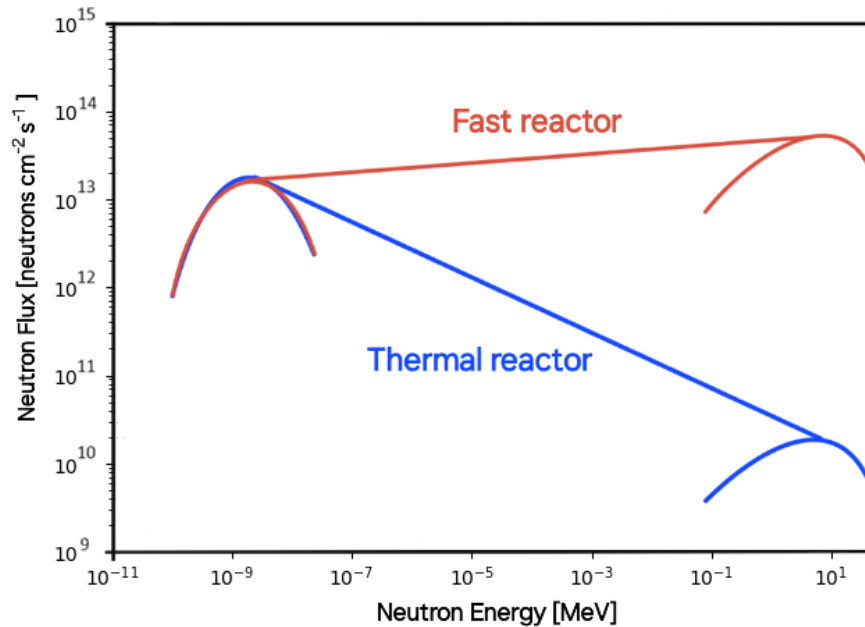


Figure 28: Representative graph of the Fast reactor spectrum and the Thermal one.

4 Results

This chapter presents and discusses the results obtained in the framework of the simulation-based analysis. The discussion is organized into four main sections, each addressing a key aspect of the modeling and transport calculation process.

The first section (Section 4.1) focuses on simplifying the reactor model, highlighting the geometric and material approximations adopted to enable efficient and traceable Monte Carlo simulations, while preserving the physical fidelity of the system. It then deals with the characterization of the source interface, where the impact of the chosen configuration and particle sampling strategy on the overall transport accuracy is evaluated.

The second section (Section 4.2) presents the neutron flux results, comparing the outcomes obtained using the direct SDEF source approach with those derived from the SSR/SSW interface method. This comparison provides insight into the strengths and limitations of each technique in reproducing the neutron distribution in the target domain.

The third section (Section 4.3) reports the photon flux results, with a focus on the photon transport through lead and the evaluation of the dose arriving to the tallies.

Finally, the fourth section (Section 4.4) reports the last data analysis and final discussion about the fission chamber characterization and deployment in LFRs.

4.1 Reactor Model simplification

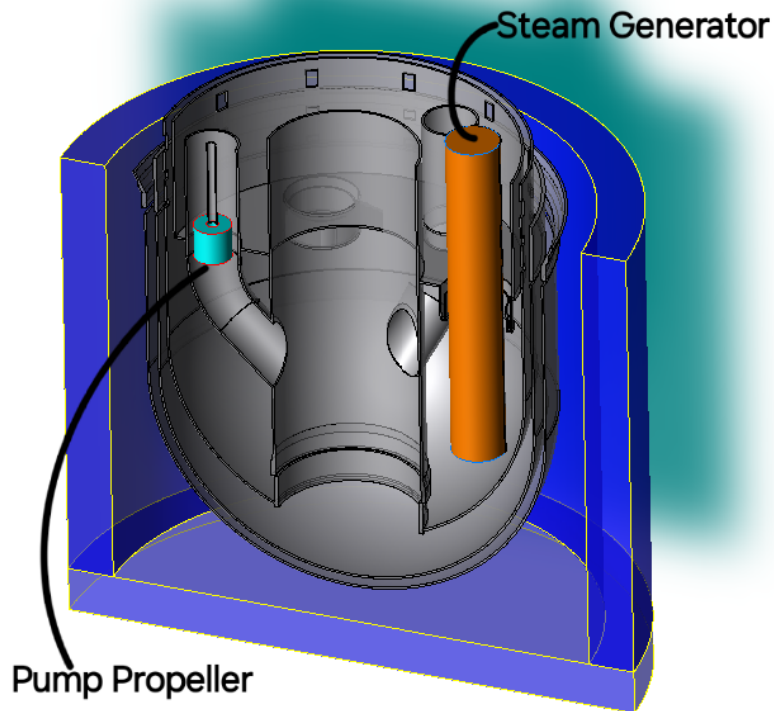


Figure 29: ALFRED Reactor Vessel Model with the CAD imported parts, the concrete shielding, and the homogenized components.

As it has been explained in the section 3.1, it was decided to built from scratch the new ALFRED Reactor Vessel model. After the CAD importing of the realistic steel internal structures and the creation of the shielding by intersecting a cylinder with a plane having the same thickness of concrete, it was necessary to understand how to model and homogenize in the more correct way the Steam Generator and the Pump Propeller.

In order to do so, an accurate analysis of the existent 3D models of the two components has been performed using TopMC, starting with the Steam Generator one.

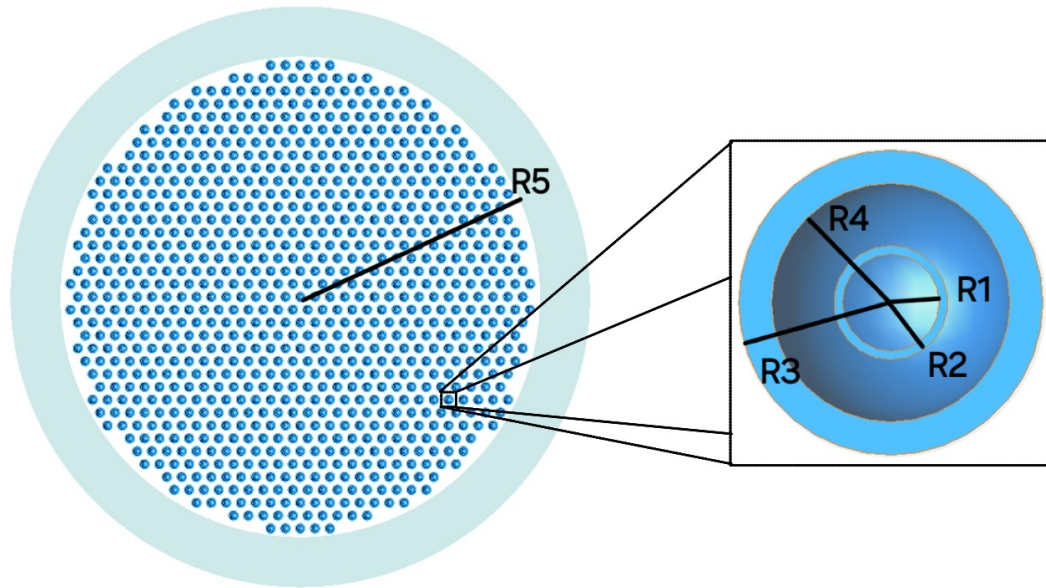


Figure 30: Meridian section of the Steam Generator with a zoom on the right.

To simplify the geometric modeling of the steam generator while preserving its neutron interaction characteristics, the entire structure is represented as a single equivalent homogeneous cylinder with radius $R5$, corresponding to the outer boundary of the generator's cross-section excluding its steel boundary. This homogenization allows for a substantial reduction in computational complexity while maintaining accurate physical behavior for reactor physics analyses.

The internal structure of the Steam Generator consists of 880 identical heat-exchange assemblies, each composed of two concentric tubes designed to channel water and steam. These are surrounded by structural steel and fully embedded in a liquid lead matrix. Each assembly is composed of four concentric cylindrical regions:

- Region 1: inner water-filled tube (radius $R1$)
- Region 2: steel shell surrounding the water tube (radius $R2$)
- Region 3: outer concentric annulus including steel, vapor, and water (radius $R3$)
- Region 4: same as Region 3 but without steel (radius $R4$)
- Region 5: external radius of the entire steam generator.

Given that the Steam Generator is uniform along its axial (longitudinal) direction—*i.e.*, the internal structure and material distribution are constant along the height—homogenization

can be performed in two dimensions, on the transverse circular cross section. This means that instead of averaging over the entire 3D volume, it is sufficient to calculate area fractions of each material within the circular slice shown in Figure 30. To do this, the material area totals in the whole generator are computed:

- Water : $A_{\text{H}_2\text{O}} = \pi R_1^2$
- Steel: $A_{\text{steel}} = \pi(R_2^2 - R_1^2) + \pi(R_3^2 - R_4^2)$
- Vapor: $A_{\text{vapor}} = \pi(R_4^2 - R_2^2)$
- Lead: $A_{\text{Pb}} = \pi R_5^2 - 880(A_{\text{H}_2\text{O}} + A_{\text{steel}} + A_{\text{vapor}})$

and the homogenized composition of the Steam Generator was computed using these fractions:

$$f_i = \frac{A_i}{A_{\text{total}}} \text{ for } i \in \{\text{H}_2\text{O}, \text{vapor}, \text{steel}, \text{Pb}\}$$

with $A_{\text{total}} = \pi R_5^2$. Finally, since the exact dimensions of the components under study cannot be disclosed, material fractions are provided as a representative indication of the homogenization process:

$$f_{\text{H}_2\text{O}} = 0.74, f_{\text{vapor}} = 0.033, f_{\text{steel}} = 26.02, f_{\text{Pb}} = 73.17 .$$

After that, an analogous homogenization procedure was applied to the pump in order to obtain a representative material composition suitable for simulation purposes.

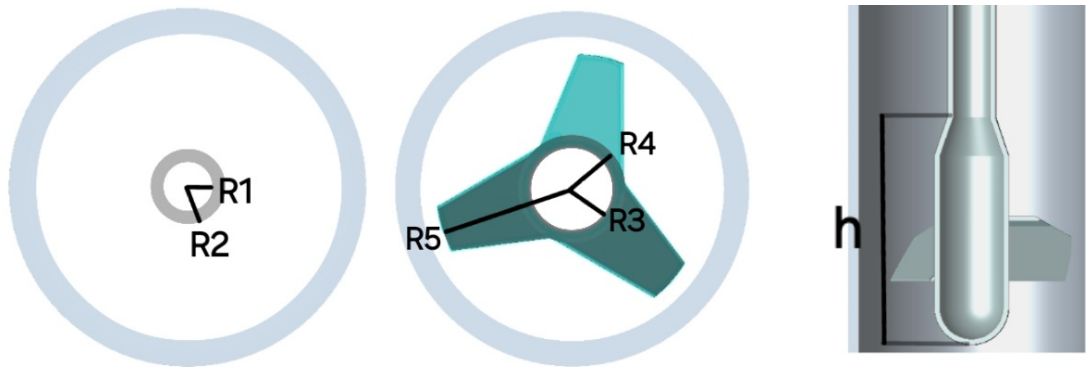


Figure 31: Meridian sections of the Pump Propeller: in correspondence with the tube (left) and in correspondence with the propeller (center), and longitudinal section of the propeller part (left).

To accurately represent the pump geometry in a simplified model suitable for neutron analysis, the component was divided into two main regions: the propeller section, which plays a significant role in neutron transport, and the outer tube, which consists solely of structural steel and void. The outer tube was excluded from the homogenization process because it was simply modeled as a hollow steel cylinder.

The propeller region, shown in the center image of Figure 31, is characterized by a complex internal geometry. However, to reduce the computational effort while preserving essential material properties, the region was homogenized into another hollow cylinder extending axially over a height h , as shown in the right image of Figure 31.

The homogenization is based on the circular cross-section of the propeller region, leveraging the axial uniformity of the geometry. The cross-section is divided into concentric regions:

- Region 1: inner void channel (radius R_3)
- Region 2: steel hollow tube region (radius R_4)
- Region 3: steel hollow tube region including the paddle blades (Radius R_5).

The region to be homogenized is the annular volume between R_3 and R_5 , where both steel pipe and the propeller blades are located. To simplify the representation of the complex blade geometry, the paddle region is approximated as being composed of:

- 1/3 of the paddle thickness (innermost portion): made of steel
- 2/3 of the paddle thickness (outermost portion): made of lead,

this corresponds to assigning the paddle region a radial partition, which is translated into area contributions assuming cylindrical symmetry.

Therefore, after defining $\Delta R = R_5 - R_3$, the material area totals are:

- Steel: $A_{\text{steel}} = \pi[(R_4 + 1/3\Delta R)^2 - R_4^2] + \pi(R_4^2 - R_3^2) = \pi[R_4 + 1/3\Delta R]^2 - R_3^2]$
- Lead: $A_{\text{pb}} = \pi[R_5^2 - (R_5^2 - (R_4 - 1/3\Delta R)^2)]$

and the homogenized composition of the Pump Propeller was computed using these fractions:

$$f_i = \frac{A_i}{A_{\text{total}}} \text{ for } i \in \{ \text{vapor, steel, Pb} \}$$

with $A_{\text{total}} = \pi(R_5^2 - R_3^2)$. As previously, since the exact dimensions of the components under study cannot be disclosed, material fractions are provided as a representative indication of the homogenization process:

$$f_{\text{steel}} = 3.11, f_{\text{pb}} = 96.89 .$$

4.1.1 Source interface characterization

In light of the considerations made in the Methodology chapter, the decision was made to proceed with the development of the new “ALFRED Reactor Vessel model” with a source interface.

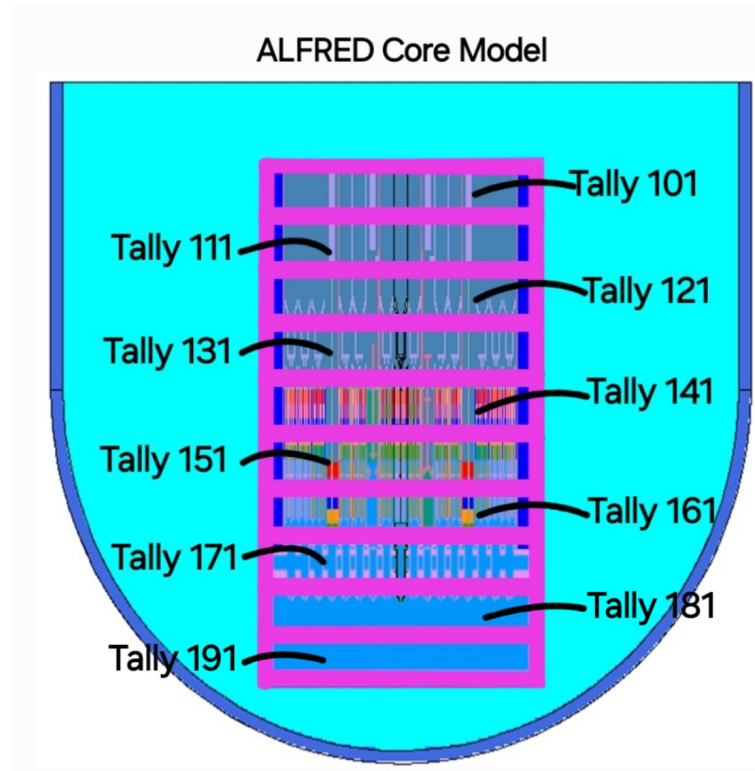


Figure 32: Interface in the ALFRED Core Model with tallies identification.

In this section, the normalized results of the Monte Carlo simulation (made by Ansaldo with MCNP) of the ALFRED Core Model are shown in graphs, while the relative tables can be found in Appendix III. Please note that the neutron flux values reported on the ordinate of the following graphs are not divided by the width of the corresponding energy bin or by lethargy, but represent the actual neutron flux value (neutrons $\text{cm}^{-2} \text{s}^{-1}$) divided by the total one. These provide the information on fission's neutrons and photons at the interface with the new ALFRED Reactor Vessel Model.

Neutron energy spectrum ALFRED Core Model

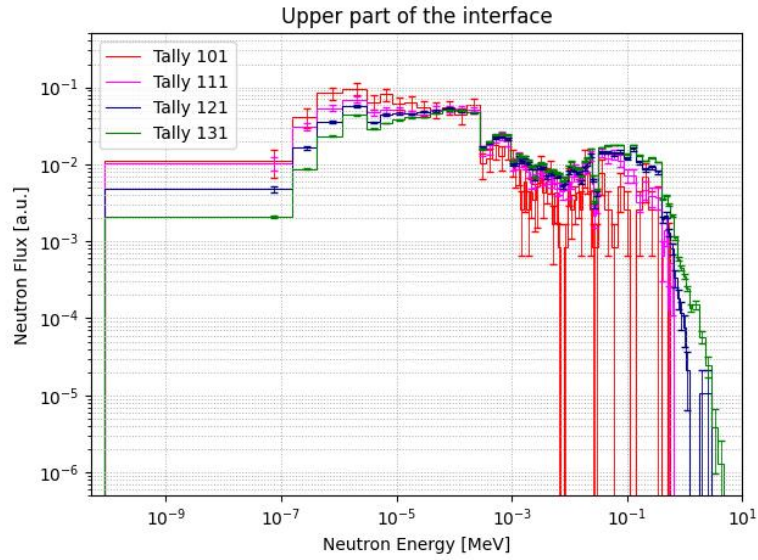


Figure 33: Graph (logarithmic scale) of the Neutron Flux vs Energy of the upper part of the interface between the ALFRED Core Model and the ALFRED Reactor Vessel Model.

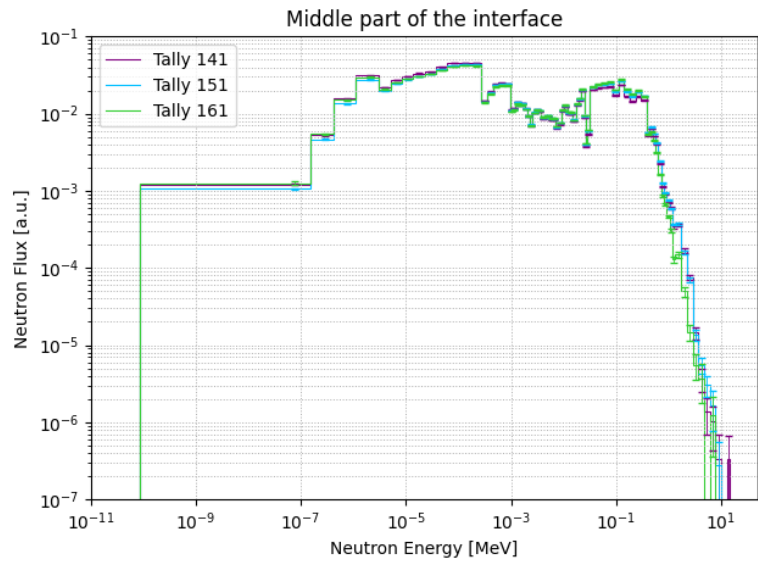


Figure 34: Graph (logarithmic scale) of the Neutron Flux vs Energy of the middle part of the interface between the ALFRED Core Model and the ALFRED Reactor Vessel Model.

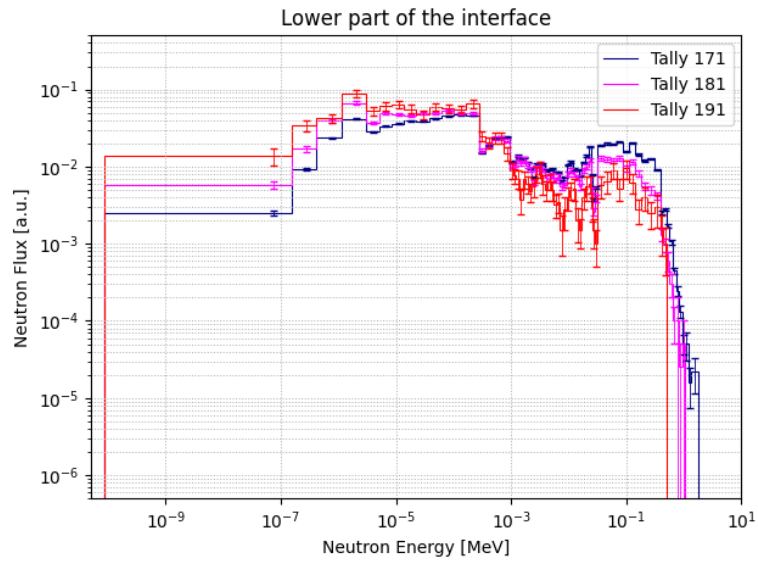


Figure 35: Graph (logarithmic scale) of the Neutron Flux vs Energy of the lower part of the interface between the ALFRED Core Model and the ALFRED Reactor Vessel Model.

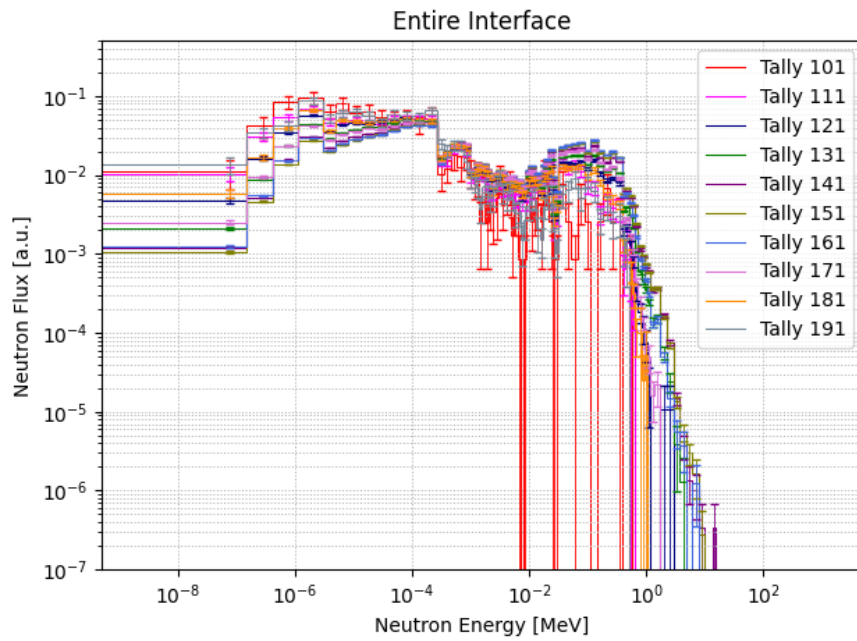


Figure 36: Graph (logarithmic scale) of the Neutron Flux vs Energy of the entire interface between the ALFRED Core Model and the ALFRED Reactor Vessel Model.

In conclusion, the neutron energy spectra observed at the core-vessel interface of the ALFRED Reactor Vessel model, as depicted in the preceding graphs, clearly reflect the characteristic feature of a fast reactor environment. Specifically, the spectrum is characterized by two prominent features:

- The first is a low-energy peak associated with thermal neutrons, typically around 10^{-8} MeV. Although ALFRED is designed as a fast reactor, some degree of thermalization is still observed, due also to minor interactions with structural materials impurities, leading to a residual thermal component in the spectrum.
- More significantly, a second, broader peak appears in the intermediate-to-fast energy range, between 0.1 and 1 MeV. In ALFRED, where a heavy material like lead is used as the coolant, neutron moderation is minimal. Lead has a relatively low neutron moderating power due to its high atomic mass and low scattering cross section, meaning that fission neutrons are not significantly slowed down. As a result, the fast component remains clearly visible.

The dual peak structure observed is therefore a signature of the reactor's fast neutron environment, with minimal spectral softening. This behavior is consistent with the design goals of ALFRED, which aims to maximize fast neutron flux.

Photon energy spectrum ALFRED Core Model

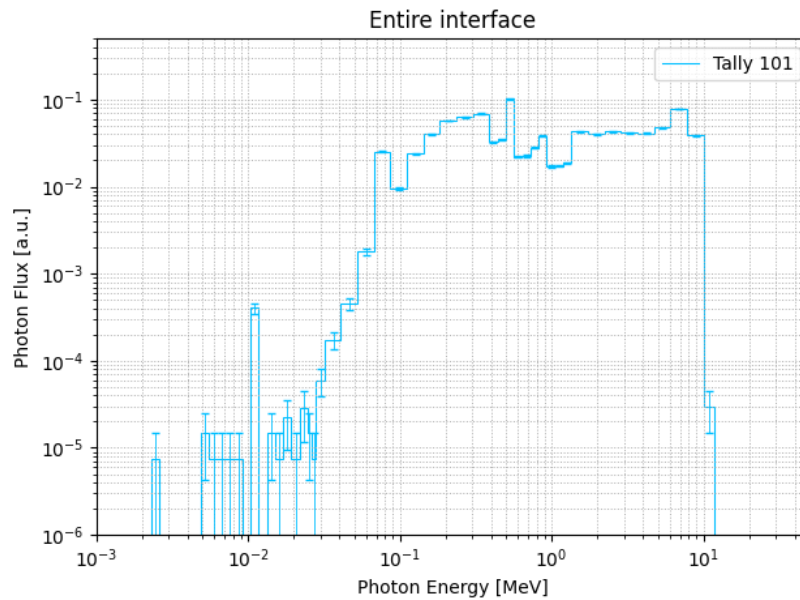


Figure 37: Graph (logarithmic scale) of the Photon Flux vs Energy of the entire interface between the ALFRED Core Model and the ALFRED Reactor Vessel Model.

4.2 Neutron fluxes results

This section presents the results of the neutron energy measurements obtained during the simulations performed both with SDEF and SSR/SSW approaches.

As already reported in the chapter of the Methodology, in order to reduce the time needed to perform the variance reduction process, the whole simulation domain of the ALFRED Reactor Vessel Model was divided into two parts, one above the other (see Figure 21 and Figure 22), with the relative weight meshes.

The following graphs (the relative tables can be found in the Appendix III) summarize the simulated neutron energy normalized values across the tallies showed in Figure 23 and Figure 24.

4.2.1 Results of the SDEF Approach

Upper part of the ALFRED Reactor Vessel Model

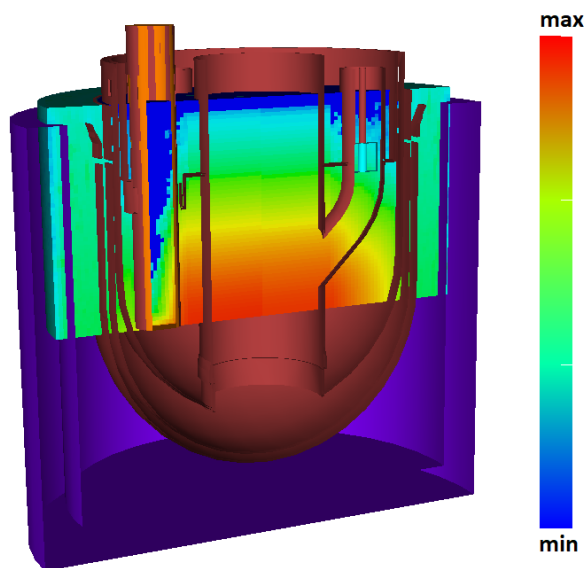


Figure 38: Behavior of the total neutron flux in the upper part of the ALFRED Reactor Vessel Model with the SDEF approach.

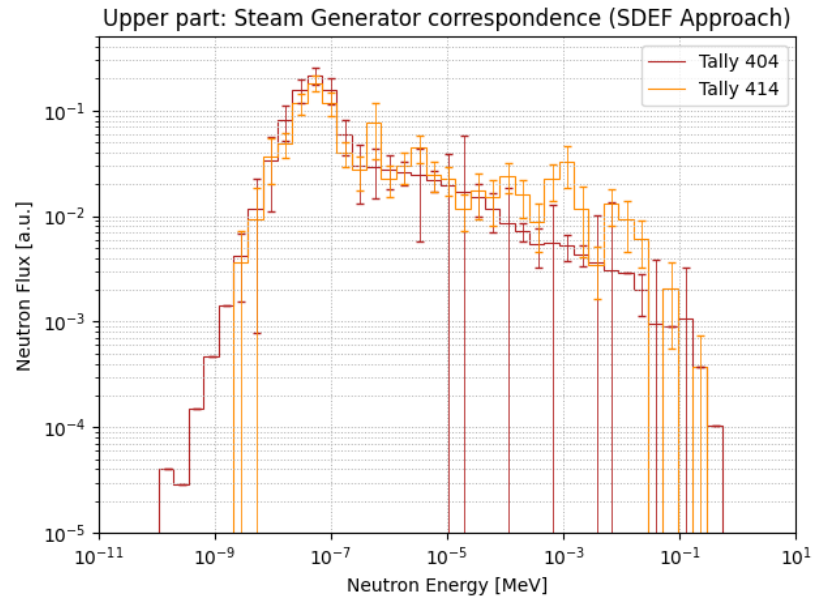


Figure 39: Graph (logarithmic scale) of the normalized Neutron Flux vs Energy simulated with the SDEF Approach, in the two Tallies in correspondence of the Steam Generator.

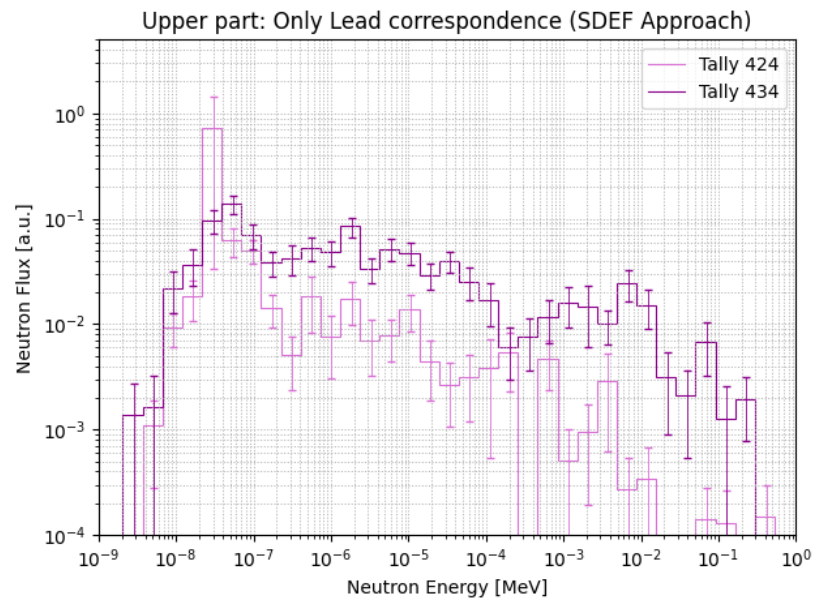


Figure 40: Graph (logarithmic scale) of the normalized Neutron Flux vs Energy simulated with the SDEF Approach, in the two Tallies in correspondence of only pure Lead.

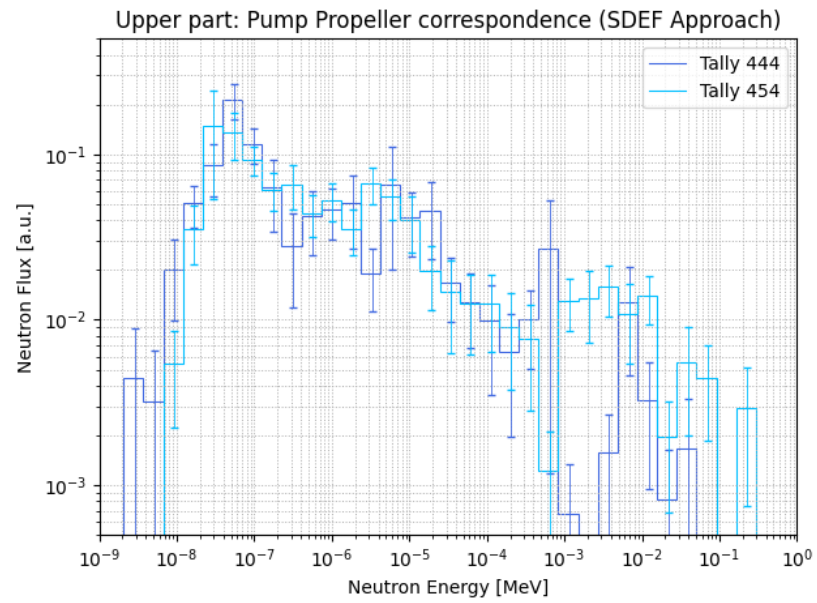


Figure 41: Graph (logarithmic scale) of the normalized Neutron Flux vs Energy simulated with the SDEF Approach, in the two Tallies in correspondence of the Pump Propeller.

Lower part of the ALFRED Reactor Vessel Model

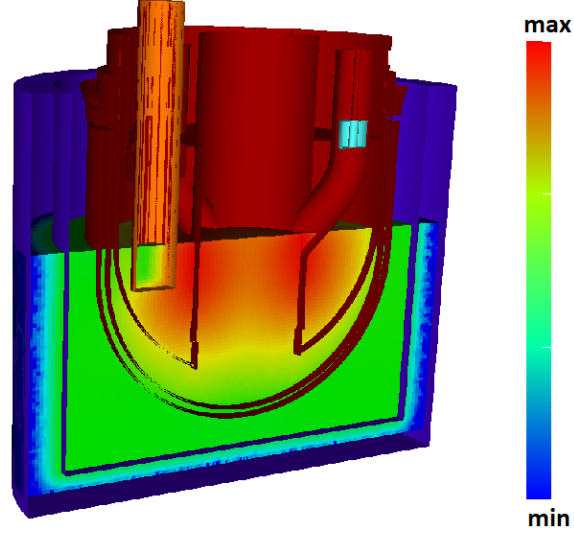


Figure 42: Behavior of the total neutron flux in the lower part of the ALFRED Reactor Vessel Model with the SDEF approach.

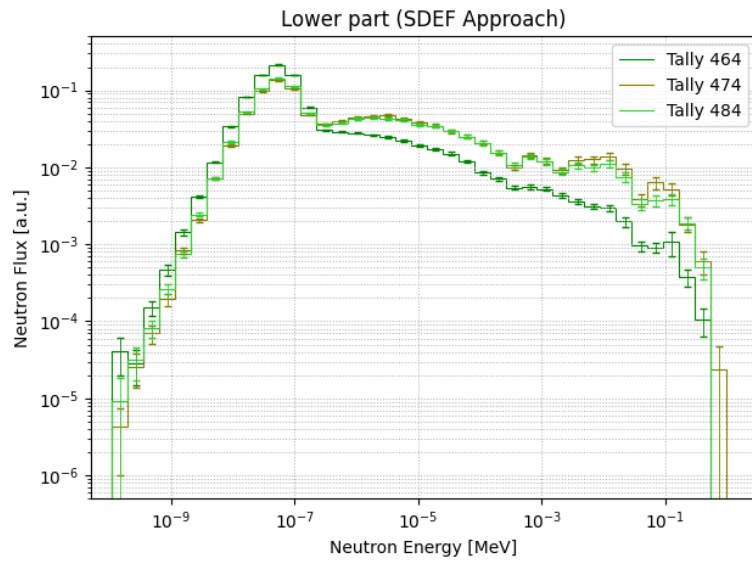


Figure 43: Graph (logarithmic scale) of the normalized Neutron Flux vs Energy simulated with the SDEF Approach, in the three Tallies in the lower part of the reactor.

4.2.2 Results of the SSR/SSW Approach

Upper part of the ALFRED Reactor Vessel Model

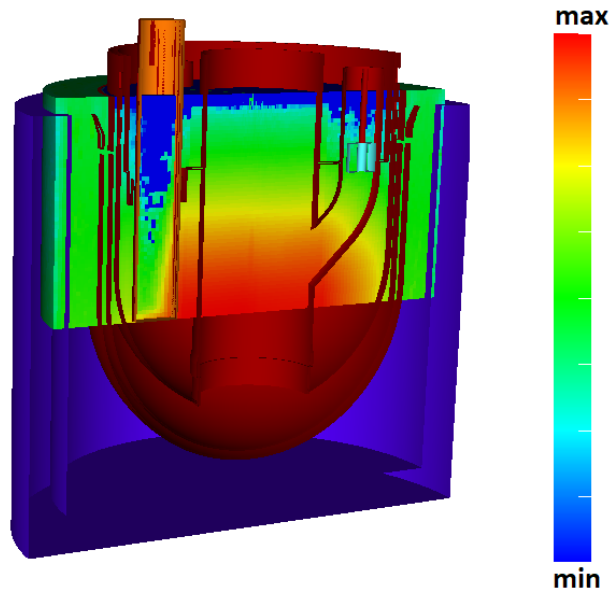


Figure 44: Behavior of the total neutron flux in the upper part of the ALFRED Reactor Vessel Model with the SSR/SSW approach.

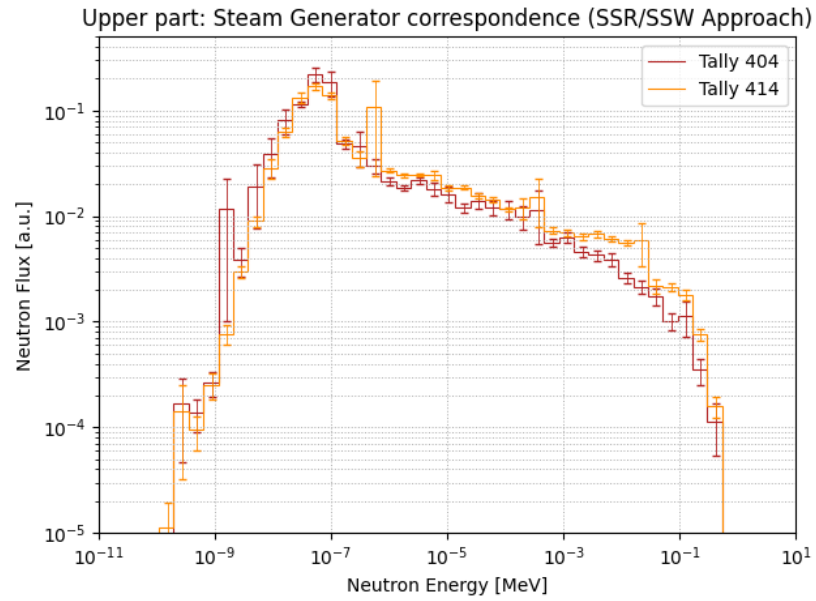


Figure 45: Graph (logarithmic scale) of the normalized Neutron Flux vs Energy simulated with the SSR/SSW Approach, in the two Tallies in correspondence of the Steam Generator.

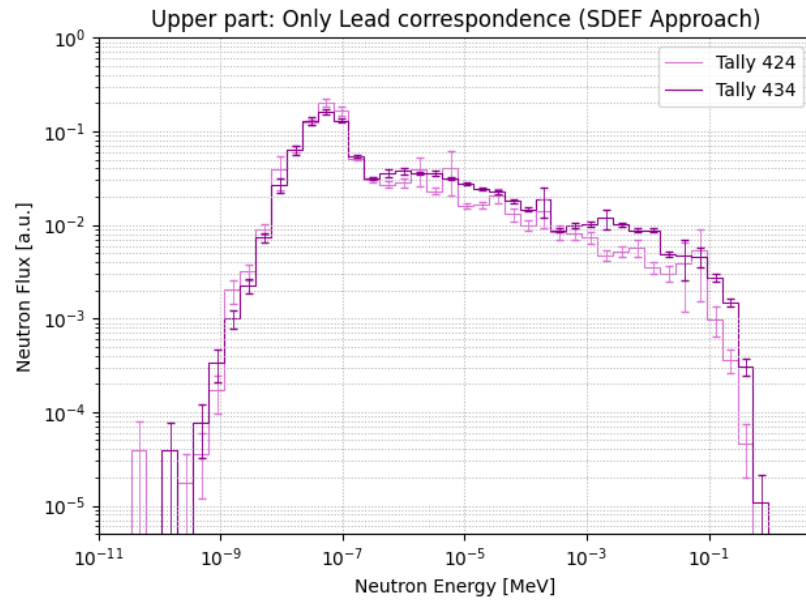


Figure 46: Graph (logarithmic scale) of the normalized Neutron Flux vs Energy simulated with the SSR/SSW Approach, in the two Tallies in correspondence of pure Lead.

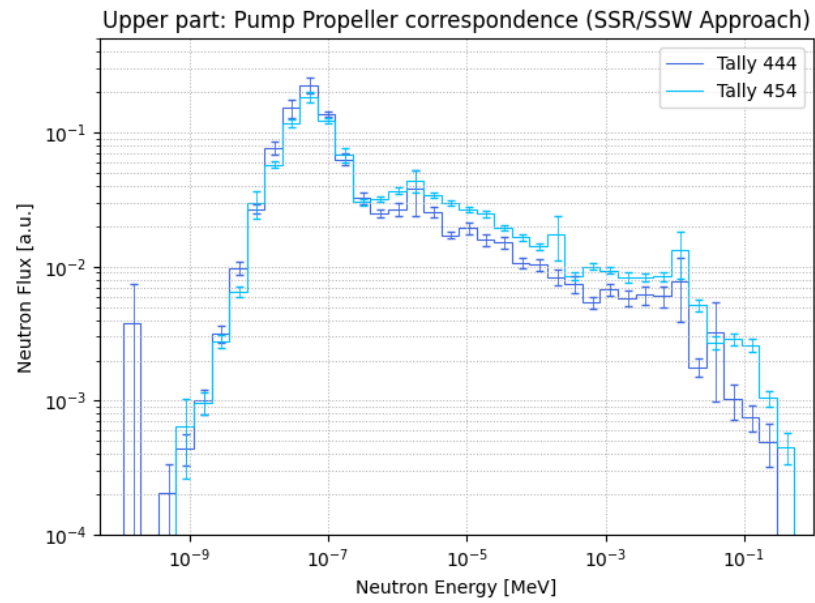


Figure 47: Graph (logarithmic scale) of the normalized Neutron Flux vs Energy simulated with the SSR/SSW Approach, in the two Tallies in correspondence of the Pump Propeller.

Lower part of the ALFRED Reactor Vessel Model

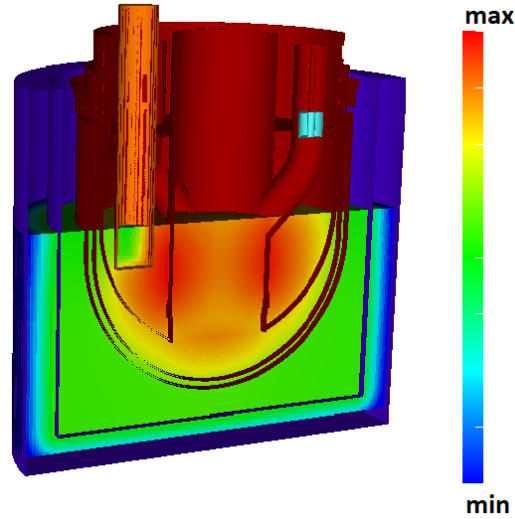


Figure 48: Behavior of the total neutron flux in the lower part of the ALFRED Reactor Vessel Model with the SSR/SSW approach.

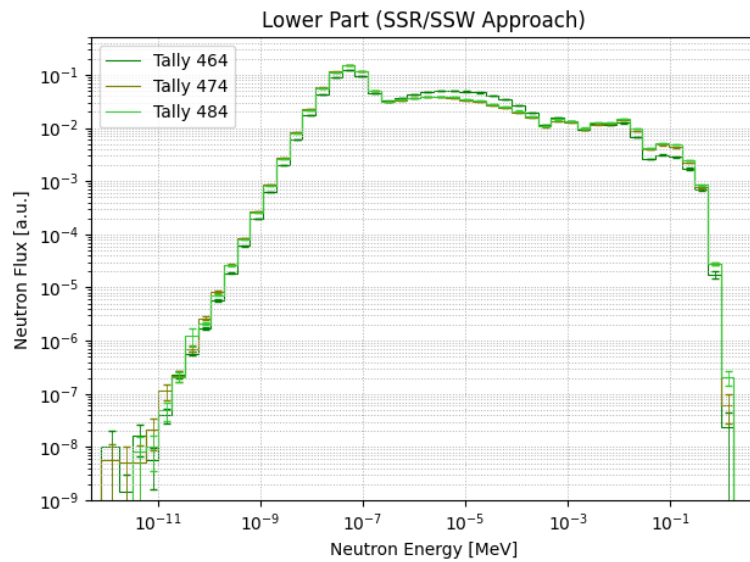


Figure 49: Graph (logarithmic scale) of the normalized Neutron Flux vs Energy simulated with the SSR/SSW Approach, in the three Tallies in the lower part of the reactor.

4 RESULTS

In order to assess whether the error introduced by the SDEF approach is significant, a compatibility analysis was performed by comparing the values of the total neutron flux (i.e., energy integrated) obtained using both methods. Although the values cannot be explicitly reported here, the table 8 below presents the ratio between these values alongside the corresponding value of the associated statistic standard deviation (σ).

Tally	Ratio [neutron/cm ² s]	σ
404	1,73E+00	1,4E-01
414	1,68E+00	1,9E-01
424	1,01E+00	6,0E-02
434	8,45E-01	2,3E-02
444	9,42E-01	4,9E-02
454	7,83E-01	2,6E-02
464	1,07E+01	9,1E-02
474	2,22E+00	3,6E-02
484	3,40E+00	5,6E-02

Table 8: Number of tallies, relative ratios of the total neutron fluxes of both approaches, and σ uncertainties obtained by doing the sum in the quadrature of the relative flux errors and then multiplying it by the ratio values.

Given that the value of the ratios is not compatible with 1 (within a standard deviation) in all cases except in the Tally 424 case, we conclude that the systematic error introduced by the SDEF approach is statistically significant. Therefore, the conclusions will be drawn based on the data obtained from the SSR/SSW approach.

4.3 Photon fluxes results

As previously explained in the chapter of Methodology, to test the contribution with respect to the natural background in all the suggested location of the fission chambers depicted in Figure 23 and Figure 24, it was decided to apply a very simplified Monte Carlo simulation approach. The simulation was performed in a parallelepiped-shaped model representing the shortest photons path inside the lead (see Figure 28), in order to evaluate the fission photon's dose rate arriving at the fission chambers.

In this section the simulation results are presented in the following contour plot and graph (see Appendix III for the data table).

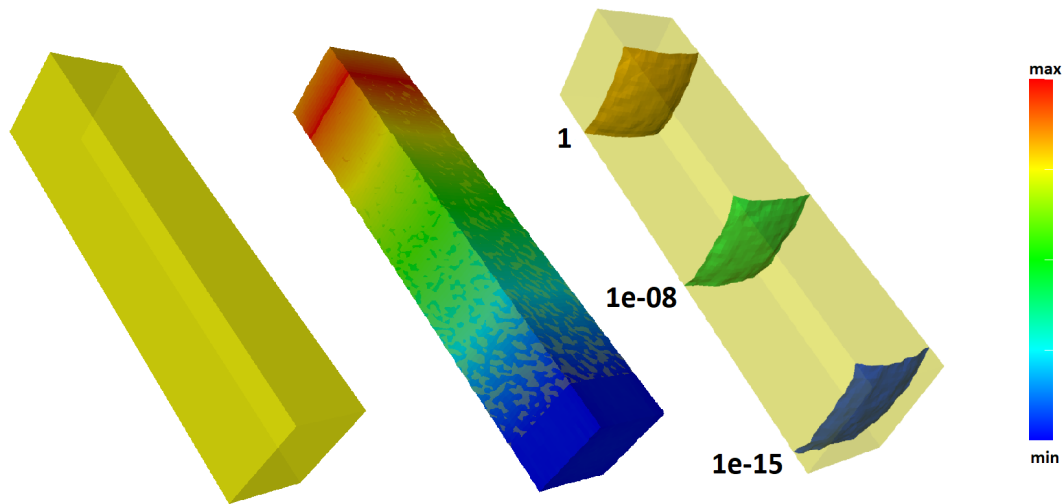


Figure 50: Representation of the shortest photon path through the lead (left), of the mesh used in photon simulation (middle) and the contour plot (right) of the background radiation level (10^{-8} Gy/h), the result of the photon simulation (10^{-15} Gy/h) and a reference value (1 Gy/h).

The TopMc processor automatically determines the energy-to-dose conversion factor thereby enabling the calculation of dose as a function of the depth (see table in the Appendix). In graph 51, the trend of the dose as a function of lead thickness is presented. The results are consistent with expectations, as the photon flux attenuation with increasing lead thickness follows an approximately negative exponential law, which is clearly reflected in the observed behavior of the graph.

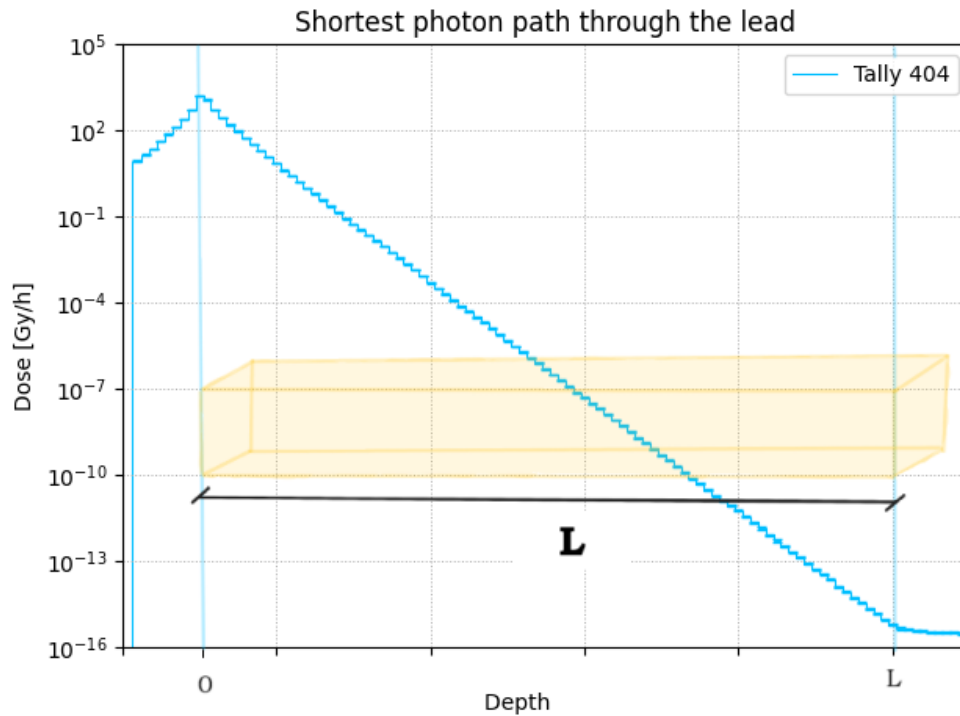


Figure 51: Graph of the Photon Dose vs Depth obtained by the simulation with the SDEF Approach in correspondence of the shortest path through lead. Since the real depth cannot be disclosed, the depth values are not defined numerically.

Finally, after these considerations, the *a priori* suggestion that prompt fission photons give a negligible contribution with respect to the natural background in all the suggested locations of the fission chambers considered in the present work was confirmed. The result was that the photon dose irradiated in the fission chambers is much lower (10^{-15} Gy/h) than the natural background ($\sim 10^{-8}$ Gy/h), making the problem of binding them nonexistent.

4.4 Fission chamber characterization results

Building on the findings presented in the previous sections of Chapter 4, it has been established that photon fluxes do not pose a risk of saturating or blinding the fission chambers under the conditions studied. As a result, the focus of the analysis can be confidently restricted to the neutron spectra component summarized in Figure 53.

With this consideration in mind, the main objective of the final phase of the study is to provide a comprehensive characterization of the fission chambers that were preliminarily selected in Chapter 2, based solely on their maximum allowable operating temperature. For each of these detectors and for each investigated position within the reactor model, key performance parameters are reported and analyzed. These include: the expected neutron flux range, therefore, the corresponding mode of operation, the fast-to-thermal flux ratio, the energy spectrum correction factor (ESCF), the sensitivity to the thermal and fast neutron spectrum, and the total sensitivity (i.e., thermal plus fast). The thermal sensitivity values are derived from the manufacturer's technical datasheet, while the remaining parameters are evaluated based on simulation results and spectral analyses.

By comparing the data obtained from the simulations with the technical specifications of the detectors, it is possible to infer the mode of operation of each individual fission chamber. This can be done by examining the average thermal spectrum flux recorded in the tallies. The following table summarizes these deductions and includes the relevant information extracted from the simulation output files for the purposes of this analysis.

Manufacturer	Model	Neutron flux range (nv)	Mode	$S _{\text{thermal}}$ [A/nv]
Photonis	CFUC06	$> 10^4 - 10^{10}$	–	2×10^{-13}
Photonis	CFUE24	$10^8 - 10^{12}$	Current	1×10^{-15}
Photonis	CFUE32	$10^9 - 10^{13}$	Current	1×10^{-16}
Photonis	CFUF43	$10^{10} - 10^{14}$	Current	1×10^{-17}
Photonis	CFUR43	$10^{11} - 1.5 \times 10^{14}$	Current	3×10^{-18}
Photonis	CFUZ53	$2 \times 10^{11} - 10^{14}$	Current	5×10^{-18}
Photonis	CFUR64	$10^{12} - 10^{15}$	Current	9.2×10^{-19}

Table 9: Characterization of the fission chambers: deduced and tabulated data. All fission chamber models operate in Current Mode, aside from the CFUC06, which can not withstand the neutron flux present in the studied environment.

As discussed in Section 3.5, the formula employed to calculate the ESCF does not involve approximations with respect to the definition of the detector response. However, due to the energy binning of the flux, the integral in the theoretical expression is

4 RESULTS

replaced by a discrete summation in the actual computation:

$$\text{ESCF}(\mathbf{r}) = \frac{R_{\text{fast}}}{R_{\text{thermal}}} = \frac{\int_E \phi(\mathbf{r}, E) \cdot \sigma_i(E) dE|_{\text{fast}}}{\int_E \phi(\mathbf{r}, E) \cdot \sigma_i(E) dE|_{\text{thermal}}} \sim \frac{\sum_i \phi_i \sigma_i|_{\text{fast}}}{\sum_i \phi_i \sigma_i|_{\text{thermal}}} \quad (10)$$

To determine this conversion factor, the flux values recorded in each tally (ϕ_i) were combined with the ^{235}U (material with which the fission chambers are made) cross sections (σ_i), as tabulated on the JANIS Web Application [42], using the same energy binning scheme.

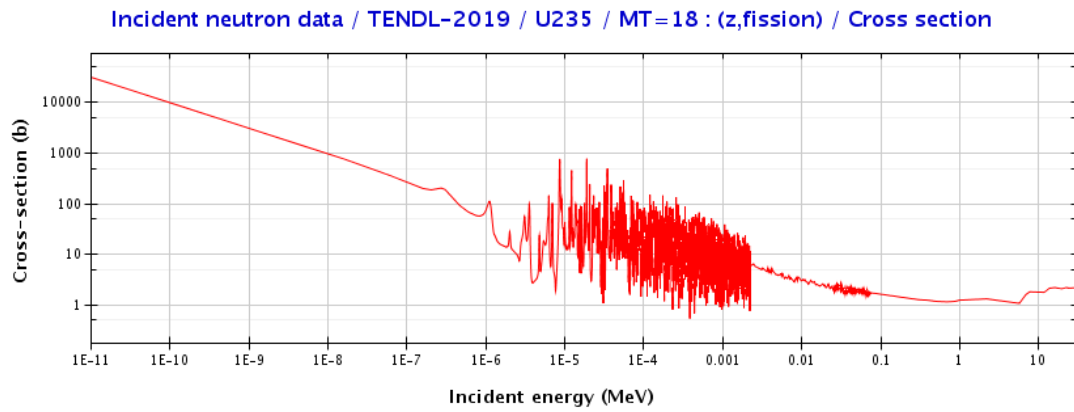


Figure 52: Neutron induced ^{235}U fission cross section vs Neutron Energy.

The table below reports both the fast-to-thermal flux ratios (note that individual flux values cannot be disclosed directly; therefore, the ratio is provided as a representative quantity) and the ESCF values for each tally.

Tally	Fast/Thermal fluxes ratio	ESCF(r)
404	2,19E-01	5%
414	3,01E-01	7%
424	3,32E-01	6%
434	4,62E-01	11%
444	2,72E-01	6%
454	4,46E-01	11%
464	6,39E-01	3%
474	5,91E-01	10%
484	8,85E-01	9%

Table 10: Characterization of fission chambers: position dependent quantities.

4 RESULTS

At this stage, it was possible to characterize each individual fission chamber by specifying: the sensitivity to the thermal spectrum (as tabulated), the sensitivity to the fast spectrum, calculated according to Equation 5, and the total sensitivity as the sum of the two components. While the thermal spectrum sensitivity values are provided in Table 9 above, the following tables report the sensitivity to the fast spectrum at each tally position (since the ESCF is position-dependent and the fast spectrum sensitivity varies accordingly, it also changes with r) and the total sensitivity.

Photonis: CFUE24									
Tally	404	414	424	434	444	454	464	474	484
$S_{fast}(r)$ [A/nv]	5,00E-17	7,00E-17	6,00E-17	1,10E-16	6,00E-17	1,10E-16	3,00E-17	1,00E-16	9,00E-17
$S_{total}(r)$ [A/nv]	1,05E-15	1,07E-15	1,06E-15	1,11E-15	1,06E-15	1,11E-15	1,03E-15	1,10E-15	1,09E-15

Photonis: CFUE32									
Tally	404	414	424	434	444	454	464	474	484
$S_{fast}(r)$ [A/nv]	5,00E-18	7,00E-18	6,00E-18	1,10E-17	6,00E-18	1,10E-17	3,00E-18	1,00E-17	9,00E-18
$S_{total}(r)$ [A/nv]	1,05E-16	1,07E-16	1,06E-16	1,11E-16	1,06E-16	1,11E-16	1,03E-16	1,10E-16	1,09E-16

Photonis: CFUF43									
Tally	404	414	424	434	444	454	464	474	484
$S_{fast}(r)$ [A/nv]	5,00E-19	7,00E-19	6,00E-19	1,10E-18	6,00E-19	1,10E-18	3,00E-19	1,00E-18	9,00E-19
$S_{total}(r)$ [A/nv]	1,05E-17	1,07E-17	1,06E-17	1,11E-17	1,06E-17	1,11E-17	1,03E-17	1,10E-17	1,09E-17

Photonis: CFUR43									
Tally	404	414	424	434	444	454	464	474	484
$S_{fast}(r)$ [A/nv]	1,50E-19	2,10E-19	1,80E-19	3,30E-19	1,80E-19	3,30E-19	9,00E-20	3,00E-19	2,70E-19
$S_{total}(r)$ [A/nv]	3,15E-18	3,21E-18	3,18E-18	3,33E-18	3,18E-18	3,33E-18	3,09E-18	3,30E-18	3,27E-18

Photonis: CFUZ53									
Tally	404	414	424	434	444	454	464	474	484
$S_{fast}(r)$ [A/nv]	2,50E-19	3,50E-19	3,00E-19	5,50E-19	3,00E-19	5,50E-19	1,50E-19	5,00E-19	4,50E-19
$S_{total}(r)$ [A/nv]	5,25E-18	5,35E-18	5,30E-18	5,55E-18	5,30E-18	5,55E-18	5,15E-18	5,50E-18	5,45E-18

Photonis: CFUR64									
Tally	404	414	424	434	444	454	464	474	484
$S_{fast}(r)$ [A/nv]	4,60E-20	6,44E-20	5,52E-20	1,01E-19	5,52E-20	1,01E-19	2,76E-20	9,20E-20	8,28E-20
$S_{total}(r)$ [A/nv]	9,66E-19	9,84E-19	9,75E-19	1,02E-18	9,75E-19	1,02E-18	9,48E-19	1,01E-18	1,00E-18

Finally, it can be affirmed that all the fission chambers selected in Chapter 2, except the CFUC06, have proven suitable for deployment in the 9 positions identified in Chapter 4 (see Figure 23 and Figure 24) outside the ALFRED reactor.

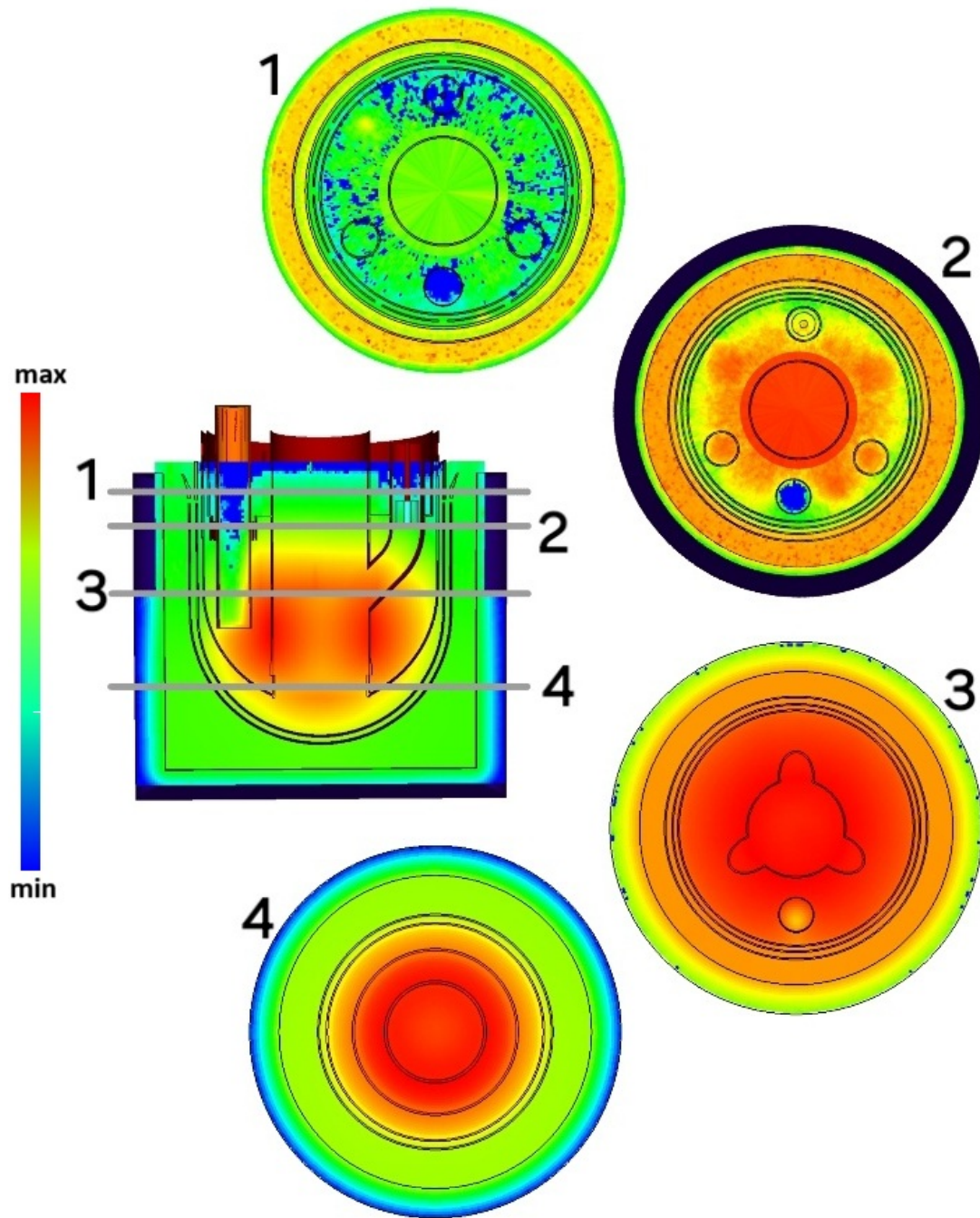


Figure 53: Behavior of the total neutron flux in the ALFRED Reactor Vessel Model with the SSR/SSW approach.

5 Conclusions

This thesis investigated the applicability of various Photonis fission chambers for neutron flux monitoring in the outer regions of the ALFRED reactor vessel, a key component in the development of Lead-cooled Fast Reactor (LFR) technology. The work was grounded in detailed Monte Carlo simulations, which aimed to replicate the neutron and photon environments encountered in peripheral reactor positions and to assess detector performance under those specific conditions.

The results of the neutron flux simulations revealed a distinct energy spectrum consistent with fast reactor characteristics: a dominant fast component with residual thermalization effects due to interactions with structural materials. This spectral behavior, observed across nine key positions within the reactor model, was fundamental in determining the detectors' operational response and in deriving the Energy Spectrum Correction Factor (ESCF). The ESCF enabled recalibration of the manufacturer-reported thermal sensitivities to better reflect the actual fast-spectrum environment of ALFRED.

Importantly, the photon flux analysis confirmed that gamma radiation at the considered positions remains well below critical thresholds, with dose rates in the order of 10^{-15} Gy/h, several orders of magnitude below natural background levels. This finding ensured that the detectors' responses could be interpreted as dominantly neutron-induced, simplifying both their design requirements and expected signal interpretation.

Each fission chamber was then characterized in terms of thermal and fast neutron sensitivity, total sensitivity, and feasible operating mode (pulse, Campbelling, or current), considering local flux intensities. The detector models characterized in the tables of Section 4.4, demonstrated a consistent response across the expected neutron flux ranges, with current-mode operation deemed viable in all cases apart from CFUC06. The ESCF values, ranging up to 11%, highlighted the non-negligible impact of spectral shifts on detector calibration and the need for correction in fast neutron environments.

From a practical perspective, the simulation data confirmed that almost all selected detectors can be effectively deployed at the identified positions outside the reactor vessels. The characterization tables provide actionable guidance on matching each detector to specific neutron flux regions within ALFRED, accounting for both performance and installation constraints.

In conclusion, this work validates the feasibility of using commercially available high-temperature fission chambers for neutron monitoring outside the ALFRED LFR demonstrator. The methodology employed, especially the use of position-dependent ESCF corrections derived from detailed spectral data, contributes a robust framework for future detector design and placement in advanced fast reactor systems. Further experimental validation would strengthen these findings, particularly under operational reactor conditions, but the results herein already provide a solid reference for instrumentation strategies in Generation IV reactor development.

Appendix I

The present Appendix shows some details of the 3 main input information used for this thesis work. It is reminded that the main input information/data was three-fold: (1) the Monte Carlo model of the ALFRED Core and the corresponding neutronic characterization; (2) the 3D geometrical model of the ALFRED Internal Structures; (3) the datasheets of some of the commercially available fission chambers.

Input 1: Monte Carlo ALFRED Core Model

This represents the initial end essential input to the study, as it supplies the neutron and photon spectra of the ALFRED reactor core, which are the focus of the present analysis. As an example of the input information, Figure 54 shows the geometrical model of the ALFRED Reactor Core model as created by ENEA and run by Ansaldo Nucleare. The reader is referred to the body of the present thesis for the detailed explanation of how this input was used.

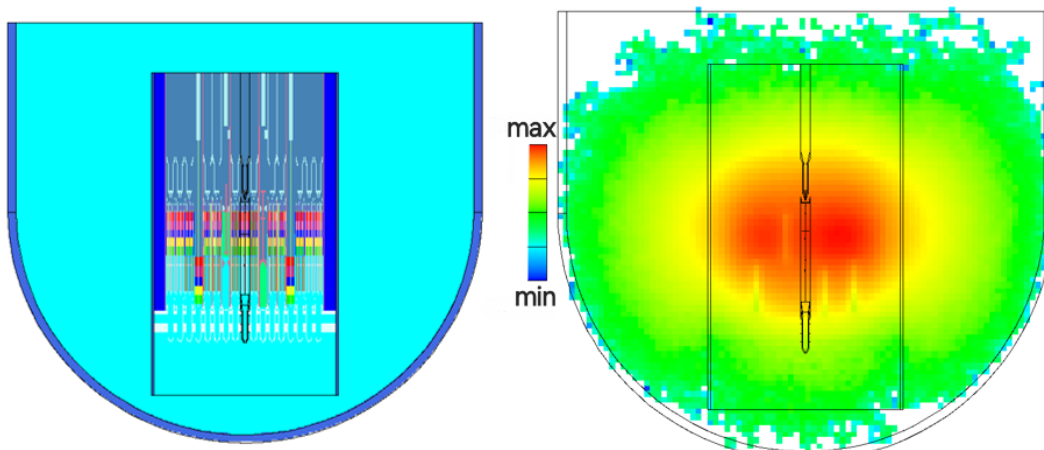


Figure 54: ALFRED Core Model received by ENEA (left) and result of the ALFRED Core Model running by Ansaldo Nucleare (right).

Input 2: The 3D model of the ALFRED Reactor Vessel and Inner Structures

The second input to the study is provided by 3D CAD models of the ALFRED reactor vessel and its internal structures. These models are essential for accurately representing the geometry of the reactor region external to the core. It was used to create the Monte Carlo geometrical model (ALFRED Reactor Vessel) that was run to obtain the neutronic characterization in the peripheral tallies.

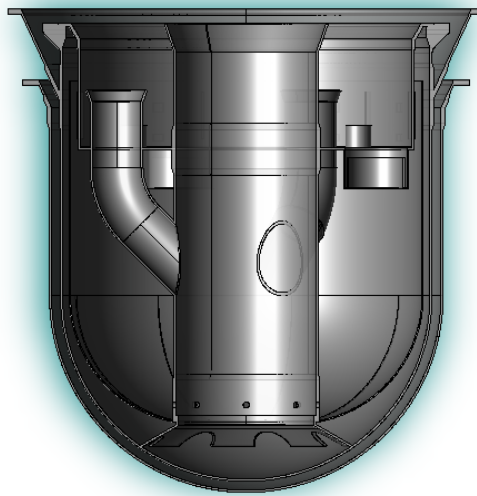


Figure 55: Alfred Reactor Vessel and Inner Structures.

Input 3: The fission chambers data sheets

The third input is represented by the technical datasheets of the fission chambers. These documents provide critical information necessary for identifying and characterizing the detectors most appropriate for the specific conditions addressed in this analysis.

Nuclear Instrumentation

BORON LINED PROPORTIONAL COUNTERS

Thermal neutron detectors / Operating in pulse mode. Watertight HN connectors ensure a high safety of use.

APPLICATIONS

- ◆ Monitoring nuclear reactors in the source range
- ◆ Fuel reprocessing operations
- ◆ Special equipment in reactors (boron-meters)

OPTIONS

- ◆ Integral HN connector
- ◆ Integral mineral insulated cable



Type	Neutron Sensitivity (cps/nv)	Neutron Flux Range (nv)	∅ (mm)	Sensor Length (mm)	Integral Cable (mm)	Max Operating T° (°C)
CPNB28	5	$2 \times 10^{-1} - 4 \times 10^5$	25.4	368	No	200*
CPNB48	10	$1 \times 10^{-1} - 2 \times 10^5$	25.4	60	No	200*
CPNB44	8	$1 \times 10^{-1} - 2 \times 10^5$	48	761	6	200*
CPNB65	25	$5 \times 10^{-2} - 5 \times 10^4$	76.5	727	No	200*
CPNB64	25	$5 \times 10^{-2} - 5 \times 10^4$	76.5	741.5	6	200*
CPNB84	42	$5 \times 10^{-2} - 3 \times 10^4$	82	741.5	6	200*

* This temperature depends on the material used to make the connection tight (inside the mating connector).
nv: thermal neutron flux in $\text{cm}^{-2} \text{s}^{-1}$. cps: counts per second.

FISSION CHAMBERS FOR OUT-OF-CORE

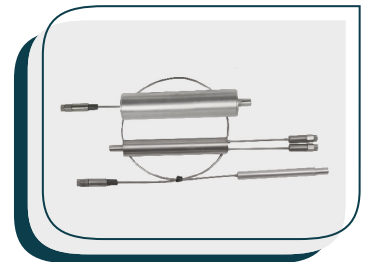
Severe environmental conditions. Watertight HN connectors ensure a high safety of use.

APPLICATIONS

- ◆ Thermal neutron detection
- ◆ Wide range reactor monitoring
- ◆ Waste monitoring

OPTIONS

- ◆ Integral HN connector
- ◆ Integral mineral insulated cable
- ◆ Complete Inconel protection



Type	Neutron Sensitivity (cps/nv)		Neutron Flux Range (nv)		∅ (mm)	Sensor Length (mm)	Integral Cable (mm)	Max Operating T° (°C)
	Pulse Mode (cps/nv)	Current Mode (A/nv)	Pulse Mode	Current Mode				
CFUM11	1×10^{-1}	1×10^{-14}	$10 - 10^7$	$10^7 - 10^{11}$	25.4	227	No	250*
CFUM18	1×10^{-1}	1×10^{-14}	$10 - 10^7$	$10^7 - 10^{11}$	25.4	263	6	250
CFUM21	1×10^{-2}	1×10^{-15}	$10^2 - 10^8$	$10^8 - 10^{12}$	25.4	227	No	250*
CFUM19	0.6	1.2×10^{-13}	$2 - 2 \times 10^6$	$2 \times 10^4 - 2 \times 10^{10}$	48	421	6 + 6	250
CFUP08	0.7	1.4×10^{-13}	$1 - 10^6$	$10^4 - 10^{10}$	76.5	389	6 + 6	250
CFUC06	1	2×10^{-13}	$1 - 10^5$	$10^4 - 10^{10}$	48	412	6 + 6	600
CFUL01	1	2×10^{-13}	$1 - 10^6$	$10^4 - 10^{10}$	48	337	No	250
CFUL08	1	2×10^{-13}	$1 - 10^6$	$10^4 - 10^{10}$	48	384.5	6	250
CFUK09	3	6×10^{-13}	$0.3 - 3 \times 10^5$	$10^5 - 10^{10}$	60	385	No	250*
CFUG08	4	8×10^{-13}	$0.2 - 2 \times 10^5$	$10^5 - 7 \times 10^{10}$	80	419	6	250

* This temperature depends on the material used to make the connection tight (inside the mating connector).
nv: thermal neutron flux in $\text{cm}^{-2} \text{s}^{-1}$. cps: counts per second.

CABLE EXTENSIONS

- ◆ High-immunity mineral insulated extension cables
- ◆ Transmission of low level impulsion signals
- ◆ Under harsh environmental conditions
- ◆ Pulse or current transmission up to 20 bars external pressure

OPTIONS

- ◆ BNC connectors
- ◆ High resistance to radiations and electromagnetic parasitic signals
- ◆ Cable insulator MgO, SiO₂ or Al₂O₃



Type	Mode	Cable		Connector		Characteristic Impedance Ω
		∅ (mm)	Insulator	Type	Insulator	
EXT-BNC	Current	3	Al ₂ O ₃	BNC	PTFE	-
EXT-HN	Pulse	6	MgO	HN	Al ₂ O ₃	50

FISSION CHAMBERS FOR IN-CORE USE

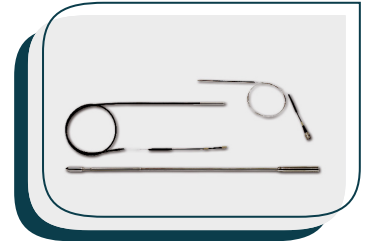
Under severe environmental conditions: high T° - humidity - gamma flux

APPLICATIONS

- ◆ Detection of thermal neutrons in high flux
- ◆ Monitoring of the reactor fuel burn up
- ◆ Start-up, intermediate and power range
- ◆ Flux map measurement

OPTIONS

- ◆ Integral HN connector
- ◆ Integral mineral insulated cable
- ◆ Movable versions with propulsion cable



Type	Neutron Sensitivity (cps/nv)		Neutron Flux Range (nv)		∅ (mm)	Sensor Length (mm)	Integral Cable (mm)	Max Operating T° (°C)
	Pulse Mode (cps/nv)	Current Mode (A/nv)	Pulse Mode	Current Mode				
CFUE24	1 x 10 ⁻²	1 x 10 ⁻¹⁵	10 ² – 10 ⁸	10 ⁸ – 10 ¹²	7	150	6	400
CFUE32	1 x 10 ⁻³	1 x 10 ⁻¹⁶	10 ³ – 10 ⁸	10 ⁹ – 10 ¹³	7	150	6	600
CFUF43	-	1 x 10 ⁻¹⁷	-	10 ¹⁰ – 10 ¹⁴	4.7	86	1	350
CFUR43	-	3 x 10 ⁻¹⁸	-	10 ¹¹ – 1.5x10 ¹⁴	3	42	1	350
CFUZ53	-	5 x 10 ⁻¹⁸	-	2x10 ¹¹ – 10 ¹⁴	1.5	49	1	350
CFUR64	8 x 10 ⁻⁶	9.2 x 10 ⁻¹⁹	10 ⁶ – 10 ¹¹	10 ¹² – 10 ¹⁵	3	42	2.2	400

nv: thermal neutron flux in cm⁻² s⁻¹. cps: counts per second.

GAMMA IONISATION CHAMBERS

MEASUREMENT OF GAMMA RADIATIONS

- ◆ In nuclear power plants
- ◆ In uranium reprocessing plants
- ◆ From ⁶⁰Co sources

OPTIONS

- ◆ Guard ring structure (very low leakage current)
- ◆ Compensation of energy spectrum by metallic filters

Gas characteristics adapted to requirements.

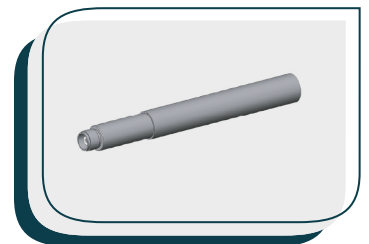


Type	Gamma Sensitivity (A/Gy h ⁻¹ ⁶⁰ Co)	Gamma Flux Range (Gy/h)	∅ (mm)	Sensor Length (mm)	Integral Cable (mm)	Max Operating T° (°C)
CRGJ16	5 x 10 ⁻⁸	10 ⁻⁵ – 50	42.5	189	4+4	250
CRGB10/Xe	7.2 x 10 ⁻⁸	10 ⁻⁵ – 2 x 10 ²	48	137	No	250*
CRGB10/N ₂	6 x 10 ⁻¹⁰	10 ⁻³ – 10 ⁵	48	137	No	250*
CRGA11	1.5 x 10 ⁻¹⁰	3 x 10 ⁻³ – 10 ³	18	234	3+3	350
CRGE10/Xe	4.5 x 10 ⁻¹¹	10 ⁻¹ – 10 ⁶	7	85.5	3	400
CRGE10/N ₂	4.8 x 10 ⁻¹³	10 – 10 ⁸	7	85.5	3	400

* This temperature depends on the material used to make the connection tight (inside the mating connector).

DEVELOPMENTS AND CUSTOMISATION

- ◆ Adapt versions of industrialised product to customer specific requirements
- ◆ Develop new detectors with our dedicated R&D team
- ◆ Theoretical approach, modeling, qualification test
- ◆ Collaboration with the CEA
- ◆ Full control of the complete manufacturing process on site
- ◆ Support from all of the Photonis Group activities - experience and knowledge



nuclearsales@exosens.com



exosens.com

PHOTONIS
EXOSENS GROUP

Appendix II

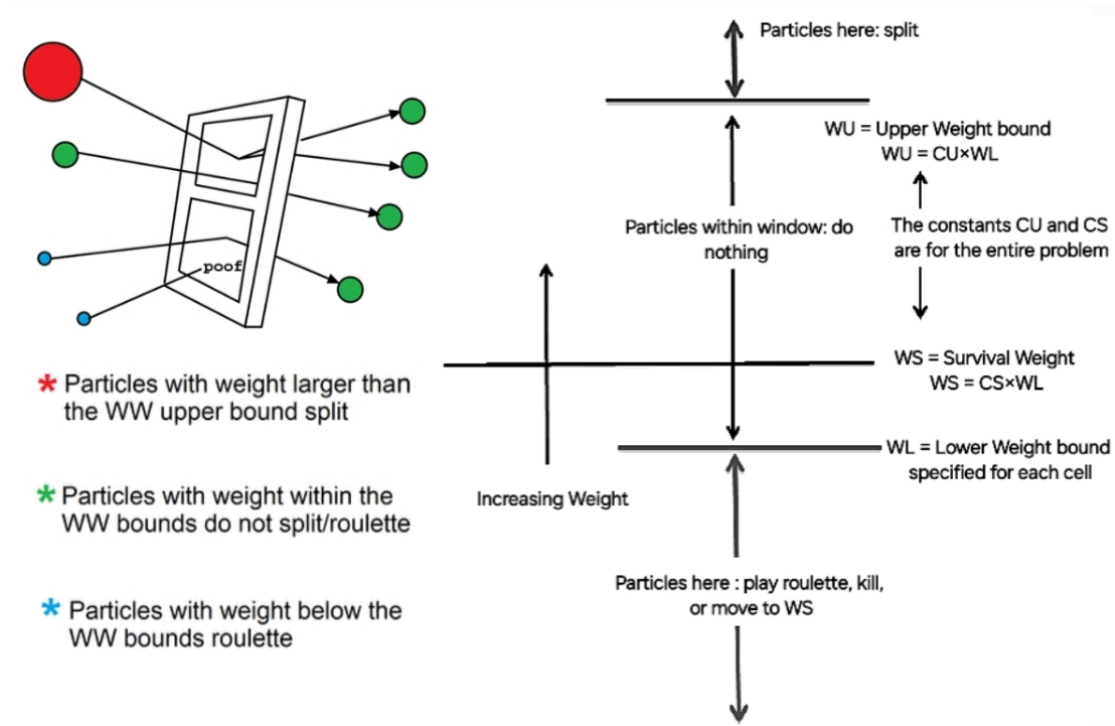
The weight window is a Monte Carlo variance reduction technique that employs phase space splitting and Russian roulette. It operates within specific phase space cells, defined by space-energy, space-time, or space.

For each of those cells, the user specifies a lower weight bound (WL). An upper weight bound (WU) and a survival weight (WS) for Russian roulette are then calculated based on this lower bound and two problem-wide constants, CS and CU , specified on a WWP card. Specifically, $WS = CS \times WL$ and $WU = CU \times WL$. These three weights— WL , WS , and WU —define the acceptable window of particle weights within a given phase space cell.

The purpose of the weight window is to manage particle weight fluctuations, particularly those introduced by other biasing techniques that can cause a particle's weight to increase significantly through "unpreferred" samplings. While individual weight increases might not be critical, their cumulative effect can seriously reduce calculational efficiency and lead to misleading error estimates. The weight window aims to mitigate these issues.

Particles are acted upon based on their weight relative to the window in their current cell:

- If a particle's weight is below the lower bound (WL), Russian roulette is played. The particle is either terminated, or its weight is increased to the survival weight (WS), placing it within the window. This prevents wasting computational effort tracking particles of trivial weight.
- If a particle's weight is above the upper bound (WU), it is split into multiple particles. The weights of the resulting split particles are adjusted so that they fall within the defined weight window. This prevents single particles from accumulating extremely large weights that could disproportionately perturb tallies and ensures subsequent weight multiplications apply only to a fraction of the original weight.
- If a particle's weight is within the window ($WL < W < WU$), no action is taken.



Ideally, the weight window is chosen such that it is inversely proportional to the importance of the phase space cell. Importance is defined as the expected score a unit weight particle will generate from a given point or upon entering a cell. By setting the window inversely proportional to importance, the technique attempts to make the product of the track weight and the mean score (for unit track weight) approximately constant across different tracks. Under these conditions, the calculation's variance is primarily attributable to the variation in the number of contributing tracks rather than the variation in the scores of individual tracks. The constant of inverse proportionality is often set such that source particles begin within the window.

The weight window technique shares similarities with geometry splitting but also has key distinctions:

- The weight window can depend on space, energy, and time, whereas geometry splitting is solely space-dependent.
- Actions in the weight window are based on a particle's absolute weight, while geometry splitting is applied irrespective of weight.
- Geometry splitting uses the ratio of importances across a surface to determine the splitting factor, whereas the weight window uses absolute weight bounds.

- The weight window can be applied at surfaces, collision sites, or both, while geometry splitting only occurs at surfaces.
- Crucially, the weight window can control weight fluctuations introduced by other biasing methods by forcing particles into the defined weight range, whereas geometry splitting preserves these fluctuations.
- Weight windows can be turned off for a cell or energy regime by setting the lower bound (WL) to zero. However, this can activate a weight cutoff game at collisions, potentially killing too many particles.
- Geometry splitting uses a product of importances for repeated structures, unlike the weight window.

Finally, the Weight Window Generator tool automatically estimates weight window importance functions, aiming to simplify the difficult task of manually determining importances through guessing, intuition, or trial and error. The generator estimates cell importance as the total score from particles entering the cell (and their progeny) divided by the total weight entering the cell. It then provides weight windows inversely proportional to these estimates in an output file formatted for use in a subsequent calculation. The generator uses standard MCNP cells or a superimposed mesh grid (cylindrical in this case) for spatial division [37].

Appendix III

Source interface characterization tables

The values present in the following tables are the result of a processing of the data obtained from the simulations that cannot be reported directly.

More precisely:

$$\text{Value} = \frac{\text{single energy data}}{\text{total energy}} \quad \sigma = \text{Value} \times \text{data relative error.}$$

Upper part of the Interface (neutrons) (first part)									
Energy bins [MeV]		Tally101		Tally111		Tally121		Tally131	
from	to	Value	σ	Value	σ	Value	σ	Value	σ
1,00E-12	1,10E-10	0,00E+00							
1,10E-10	1,53E-07	1,11E-02	4,43E-03	1,03E-02	2,05E-03	4,72E-03	3,97E-04	2,09E-03	8,76E-05
1,53E-07	4,14E-07	4,17E-02	1,18E-02	3,09E-02	3,64E-03	1,64E-02	7,89E-04	8,76E-03	2,00E-04
4,14E-07	1,12E-06	8,43E-02	1,48E-02	5,35E-02	4,91E-03	3,51E-02	1,19E-03	2,33E-02	3,47E-04
1,12E-06	3,06E-06	9,62E-02	1,78E-02	6,94E-02	6,19E-03	5,75E-02	1,55E-03	4,35E-02	4,78E-04
3,06E-06	5,04E-06	6,47E-02	1,31E-02	4,68E-02	4,46E-03	3,51E-02	1,06E-03	2,89E-02	3,44E-04
5,04E-06	8,32E-06	8,10E-02	1,53E-02	5,07E-02	4,50E-03	4,39E-02	1,22E-03	3,42E-02	3,69E-04
8,32E-06	1,37E-05	6,22E-02	1,18E-02	5,08E-02	4,46E-03	4,57E-02	1,26E-03	3,78E-02	3,89E-04
1,37E-05	2,26E-05	6,31E-02	1,44E-02	4,55E-02	4,06E-03	4,50E-02	1,19E-03	4,05E-02	4,05E-04
2,26E-05	3,73E-05	5,45E-02	1,17E-02	4,47E-02	4,00E-03	4,83E-02	1,30E-03	4,12E-02	4,08E-04
3,73E-05	6,14E-05	5,11E-02	1,20E-02	5,18E-02	4,63E-03	4,94E-02	1,28E-03	4,56E-02	4,24E-04
6,14E-05	1,01E-04	5,53E-02	1,18E-02	5,23E-02	4,45E-03	5,36E-02	1,35E-03	5,03E-02	4,53E-04
1,01E-04	1,67E-04	4,34E-02	1,02E-02	5,25E-02	4,71E-03	4,97E-02	1,29E-03	5,03E-02	4,53E-04
1,67E-04	2,75E-04	5,88E-02	1,30E-02	5,13E-02	4,55E-03	4,72E-02	1,25E-03	4,79E-02	4,41E-04
2,75E-04	3,54E-04	1,02E-02	3,81E-03	1,53E-02	2,20E-03	1,65E-02	6,34E-04	1,58E-02	2,16E-04
3,54E-04	4,54E-04	1,19E-02	3,81E-03	1,54E-02	2,17E-03	1,92E-02	6,81E-04	1,96E-02	2,41E-04
4,54E-04	5,83E-04	1,79E-02	6,32E-03	2,13E-02	2,40E-03	2,23E-02	7,40E-04	2,45E-02	2,72E-04
5,83E-04	7,49E-04	1,28E-02	4,43E-03	2,37E-02	2,74E-03	2,26E-02	7,61E-04	2,49E-02	2,74E-04
7,49E-04	9,61E-04	1,70E-02	5,52E-03	1,97E-02	2,31E-03	2,15E-02	7,24E-04	2,42E-02	2,71E-04
9,61E-04	1,09E-03	1,11E-02	4,27E-03	9,70E-03	1,51E-03	1,00E-02	4,32E-04	1,11E-02	1,59E-04
1,09E-03	1,23E-03	8,53E-03	3,62E-03	1,03E-02	1,60E-03	1,00E-02	4,32E-04	1,15E-02	1,59E-04
1,23E-03	1,40E-03	8,51E-03	3,18E-03	1,24E-02	1,95E-03	1,22E-02	4,85E-04	1,38E-02	1,78E-04
1,40E-03	1,58E-03	2,56E-03	1,91E-03	1,07E-02	1,50E-03	1,07E-02	4,50E-04	1,26E-02	1,69E-04
1,58E-03	1,80E-03	5,97E-03	3,52E-03	9,95E-03	1,49E-03	1,15E-02	4,72E-04	1,28E-02	1,72E-04
1,80E-03	2,03E-03	2,56E-03	1,91E-03	7,89E-03	1,29E-03	1,03E-02	4,45E-04	1,12E-02	1,59E-04
2,03E-03	2,31E-03	4,26E-03	2,25E-03	5,82E-03	1,07E-03	8,89E-03	4,13E-04	9,29E-03	1,46E-04
2,31E-03	2,61E-03	3,41E-03	2,09E-03	6,20E-03	1,21E-03	6,55E-03	3,48E-04	6,89E-03	1,24E-04
2,61E-03	2,96E-03	5,11E-03	3,61E-03	7,63E-03	1,25E-03	9,06E-03	4,17E-04	9,93E-03	1,50E-04
2,96E-03	3,35E-03	9,37E-03	3,51E-03	8,14E-03	1,32E-03	9,41E-03	4,20E-04	1,06E-02	1,55E-04

Upper part of the Interface (neutrons) (second part)									
Energy bins [MeV]		Tally101		Tally111		Tally121		Tally131	
from	to	Value	σ	Value	σ	Value	σ	Value	σ
3,35E-03	3,80E-03	4,26E-03	2,25E-03	6,59E-03	1,18E-03	8,91E-03	4,22E-04	1,02E-02	1,53E-04
3,80E-03	4,31E-03	5,96E-03	2,82E-03	6,72E-03	1,19E-03	6,84E-03	3,69E-04	8,23E-03	1,36E-04
4,31E-03	4,88E-03	7,66E-03	3,51E-03	6,08E-03	1,18E-03	7,61E-03	3,79E-04	8,40E-03	1,38E-04
4,88E-03	5,53E-03	1,70E-03	1,21E-03	6,85E-03	1,21E-03	7,86E-03	3,91E-04	8,54E-03	1,38E-04
5,53E-03	6,27E-03	4,26E-03	2,56E-03	4,78E-03	9,59E-04	6,97E-03	3,59E-04	7,91E-03	1,34E-04
6,27E-03	7,10E-03	8,52E-04	8,52E-04	4,91E-03	9,50E-04	7,19E-03	3,65E-04	7,70E-03	1,32E-04
7,10E-03	8,05E-03	0,00E+00	0,00E+00	4,52E-03	1,01E-03	5,09E-03	3,04E-04	6,07E-03	1,17E-04
8,05E-03	9,12E-03	8,50E-04	8,50E-04	5,69E-03	1,11E-03	5,90E-03	3,30E-04	6,69E-03	1,22E-04
9,12E-03	1,03E-02	5,96E-03	3,07E-03	4,65E-03	1,03E-03	7,82E-03	3,82E-04	9,58E-03	1,45E-04
1,03E-02	1,17E-02	2,55E-03	1,47E-03	5,94E-03	1,10E-03	8,82E-03	4,09E-04	1,10E-02	1,60E-04
1,17E-02	1,33E-02	3,41E-03	1,70E-03	8,40E-03	1,45E-03	8,30E-03	4,07E-04	8,97E-03	1,44E-04
1,33E-02	1,50E-02	4,25E-03	2,25E-03	7,24E-03	1,27E-03	7,75E-03	3,95E-04	8,71E-03	1,40E-04
1,50E-02	1,70E-02	2,55E-03	1,90E-03	7,76E-03	1,43E-03	5,82E-03	3,17E-04	6,93E-03	1,24E-04
1,70E-02	1,93E-02	1,02E-02	5,25E-03	8,79E-03	1,44E-03	8,81E-03	4,11E-04	1,09E-02	1,58E-04
1,93E-02	2,19E-02	7,67E-03	3,51E-03	9,43E-03	1,37E-03	1,02E-02	4,37E-04	1,21E-02	1,67E-04
2,19E-02	2,48E-02	2,55E-03	1,90E-03	1,28E-02	1,81E-03	1,31E-02	4,97E-04	1,59E-02	1,92E-04
2,48E-02	2,61E-02	8,51E-04	8,51E-04	5,56E-03	9,76E-04	6,22E-03	3,05E-04	7,17E-03	1,13E-04
2,61E-02	2,81E-02	8,51E-04	8,51E-04	2,20E-03	6,71E-04	2,88E-03	2,08E-04	3,21E-03	7,58E-05
2,81E-02	3,18E-02	8,51E-04	8,51E-04	3,23E-03	9,05E-04	4,16E-03	2,73E-04	4,68E-03	9,97E-05
3,18E-02	4,09E-02	7,65E-03	3,71E-03	1,42E-02	2,00E-03	1,42E-02	5,95E-04	1,66E-02	2,21E-04
4,09E-02	5,25E-02	2,55E-03	1,90E-03	1,20E-02	1,82E-03	1,44E-02	6,11E-04	1,75E-02	2,29E-04
5,25E-02	6,74E-02	8,49E-04	8,49E-04	1,33E-02	1,99E-03	1,36E-02	5,68E-04	1,78E-02	2,29E-04
6,74E-02	8,65E-02	5,10E-03	2,69E-03	1,12E-02	1,87E-03	1,45E-02	6,12E-04	1,78E-02	2,35E-04
8,65E-02	1,11E-01	2,55E-03	1,90E-03	7,11E-03	1,36E-03	1,19E-02	5,50E-04	1,37E-02	2,01E-04
1,11E-01	1,43E-01	0,00E+00	0,00E+00	7,11E-03	1,43E-03	1,57E-02	6,48E-04	1,79E-02	2,35E-04
1,43E-01	1,83E-01	2,55E-03	1,90E-03	3,23E-03	8,48E-04	1,06E-02	5,10E-04	1,31E-02	1,97E-04
1,83E-01	2,35E-01	6,81E-03	3,61E-03	4,65E-03	1,23E-03	8,55E-03	4,52E-04	1,11E-02	1,80E-04
2,35E-01	3,02E-01	2,56E-03	1,91E-03	3,88E-03	1,07E-03	9,10E-03	4,60E-04	1,22E-02	1,91E-04
3,02E-01	3,88E-01	2,56E-03	2,56E-03	3,75E-03	1,15E-03	7,94E-03	4,39E-04	1,07E-02	1,81E-04
3,88E-01	4,39E-01	0,00E+00	0,00E+00	6,47E-04	3,43E-04	1,91E-03	1,79E-04	3,49E-03	8,67E-05
4,39E-01	4,98E-01	0,00E+00	0,00E+00	1,42E-03	5,63E-04	2,18E-03	1,97E-04	3,96E-03	9,18E-05
4,98E-01	5,64E-01	8,56E-04	8,56E-04	1,29E-04	1,29E-04	1,29E-03	1,48E-04	3,02E-03	8,24E-05
5,64E-01	6,39E-01	0,00E+00	0,00E+00	5,17E-04	4,09E-04	8,09E-04	1,22E-04	2,14E-03	6,87E-05
6,39E-01	7,24E-01	0,00E+00	0,00E+00	0,00E+00	0,00E+00	3,34E-04	8,28E-05	1,11E-03	4,93E-05
7,24E-01	8,21E-01	0,00E+00	0,00E+00	0,00E+00	0,00E+00	1,83E-04	5,17E-05	5,91E-04	3,54E-05
8,21E-01	9,30E-01	0,00E+00	0,00E+00	0,00E+00	0,00E+00	1,19E-04	4,70E-05	4,50E-04	3,04E-05
9,30E-01	1,05E+00	0,00E+00	0,00E+00	0,00E+00	0,00E+00	7,55E-05	3,23E-05	3,53E-04	2,66E-05
1,05E+00	1,19E+00	0,00E+00	0,00E+00	0,00E+00	0,00E+00	2,16E-05	1,53E-05	2,44E-04	2,16E-05
1,19E+00	1,35E+00	0,00E+00	0,00E+00	0,00E+00	0,00E+00	0,00E+00	0,00E+00	1,37E-04	1,70E-05
1,35E+00	1,74E+00	0,00E+00	0,00E+00	0,00E+00	0,00E+00	0,00E+00	0,00E+00	1,51E-04	1,86E-05
1,74E+00	2,23E+00	0,00E+00	0,00E+00	0,00E+00	0,00E+00	1,08E-05	1,08E-05	5,75E-05	1,03E-05
2,23E+00	2,87E+00	0,00E+00	0,00E+00	0,00E+00	0,00E+00	1,08E-05	1,08E-05	2,43E-05	7,12E-06
2,87E+00	3,68E+00	0,00E+00	0,00E+00	0,00E+00	0,00E+00	0,00E+00	0,00E+00	3,83E-06	2,86E-06
3,68E+00	4,72E+00	0,00E+00	0,00E+00	0,00E+00	0,00E+00	0,00E+00	0,00E+00	1,28E-06	1,28E-06

Upper part of the Interface (neutrons) (third part)									
Energy bins [MeV]		Tally101		Tally111		Tally121		Tally131	
from	to	Value	σ	Value	σ	Value	σ	Value	σ
4,72E+00	6,07E+00	0,00E+00							
6,07E+00	7,79E+00	0,00E+00							
7,79E+00	1,00E+01	0,00E+00							
1,00E+01	1,19E+01	0,00E+00							
1,19E+01	1,35E+01	0,00E+00							
1,35E+01	1,49E+01	0,00E+00							
1,49E+01	1,69E+01	0,00E+00							
1,69E+01	1,96E+01	0,00E+00							
total	total	1,00E+00	8,26E-02	1,00E+00	3,32E-02	1,00E+00	9,90E-03	1,00E+00	3,50E-03

Middle part of the Interface (neutrons) (first part)							
Energy bins [MeV]		Tally141		Tally151		Tally161	
from	to	Value	σ	Value	σ	Value	σ
1,00E-12	1,10E-10	0,00E+00	0,00E+00	0,00E+00	0,00E+00	0,00E+00	0,00E+00
1,10E-10	1,53E-07	1,21E-03	3,61E-05	8,13E-05	3,03E-05	1,26E-03	4,91E-05
1,53E-07	4,14E-07	5,22E-03	7,94E-05	3,51E-04	6,85E-05	5,48E-03	1,11E-04
4,14E-07	1,12E-06	1,57E-02	1,48E-04	1,05E-03	1,22E-04	1,51E-02	1,95E-04
1,12E-06	3,06E-06	3,11E-02	2,09E-04	2,09E-03	1,77E-04	2,97E-02	2,74E-04
3,06E-06	5,04E-06	2,22E-02	1,55E-04	1,49E-03	1,32E-04	2,06E-02	2,02E-04
5,04E-06	8,32E-06	2,71E-02	1,71E-04	1,82E-03	1,46E-04	2,54E-02	2,23E-04
8,32E-06	1,37E-05	3,08E-02	1,82E-04	2,07E-03	1,56E-04	2,85E-02	2,37E-04
1,37E-05	2,26E-05	3,33E-02	1,90E-04	2,23E-03	1,63E-04	3,07E-02	2,46E-04
2,26E-05	3,73E-05	3,47E-02	1,91E-04	2,33E-03	1,70E-04	3,25E-02	2,53E-04
3,73E-05	6,14E-05	4,01E-02	2,05E-04	2,69E-03	1,81E-04	3,65E-02	2,66E-04
6,14E-05	1,01E-04	4,50E-02	2,20E-04	3,02E-03	1,93E-04	4,09E-02	2,82E-04
1,01E-04	1,67E-04	4,60E-02	2,21E-04	3,09E-03	1,96E-04	4,20E-02	2,85E-04
1,67E-04	2,75E-04	4,57E-02	2,24E-04	3,07E-03	1,95E-04	4,18E-02	2,84E-04
2,75E-04	3,54E-04	1,47E-02	1,08E-04	9,89E-04	9,57E-05	1,41E-02	1,43E-04
3,54E-04	4,54E-04	1,93E-02	1,23E-04	1,29E-03	1,10E-04	1,81E-02	1,61E-04
4,54E-04	5,83E-04	2,42E-02	1,40E-04	1,62E-03	1,25E-04	2,22E-02	1,80E-04
5,83E-04	7,49E-04	2,50E-02	1,42E-04	1,68E-03	1,26E-04	2,30E-02	1,84E-04
7,49E-04	9,61E-04	2,47E-02	1,41E-04	1,66E-03	1,26E-04	2,31E-02	1,82E-04
9,61E-04	1,09E-03	1,12E-02	8,21E-05	7,55E-04	7,44E-05	1,07E-02	1,08E-04
1,09E-03	1,23E-03	1,17E-02	8,32E-05	7,86E-04	7,37E-05	1,12E-02	1,10E-04
1,23E-03	1,40E-03	1,43E-02	9,46E-05	9,62E-04	8,43E-05	1,35E-02	1,23E-04
1,40E-03	1,58E-03	1,30E-02	8,86E-05	8,74E-04	7,94E-05	1,26E-02	1,17E-04
1,58E-03	1,80E-03	1,36E-02	9,10E-05	9,12E-04	8,25E-05	1,33E-02	1,22E-04
1,80E-03	2,03E-03	1,16E-02	8,36E-05	7,79E-04	7,57E-05	1,14E-02	1,12E-04
2,03E-03	2,31E-03	9,30E-03	7,53E-05	6,24E-04	6,86E-05	9,40E-03	1,02E-04
2,31E-03	2,61E-03	7,01E-03	6,45E-05	4,71E-04	5,90E-05	7,07E-03	8,69E-05
2,61E-03	2,96E-03	1,03E-02	7,91E-05	6,89E-04	7,23E-05	1,02E-02	1,06E-04
2,96E-03	3,35E-03	1,11E-02	8,24E-05	7,47E-04	7,53E-05	1,12E-02	1,11E-04
3,35E-03	3,80E-03	1,05E-02	7,98E-05	7,05E-04	7,35E-05	1,09E-02	1,10E-04
3,80E-03	4,31E-03	8,55E-03	7,18E-05	5,74E-04	6,59E-05	9,01E-03	9,92E-05
4,31E-03	4,88E-03	8,77E-03	7,28E-05	5,89E-04	6,71E-05	9,14E-03	9,96E-05
4,88E-03	5,53E-03	9,26E-03	7,50E-05	6,21E-04	6,89E-05	9,57E-03	1,02E-04
5,53E-03	6,27E-03	8,24E-03	7,09E-05	5,53E-04	6,56E-05	8,70E-03	9,74E-05
6,27E-03	7,10E-03	8,35E-03	7,10E-05	5,61E-04	6,44E-05	8,71E-03	9,75E-05
7,10E-03	8,05E-03	6,52E-03	6,26E-05	4,38E-04	5,66E-05	6,83E-03	8,60E-05
8,05E-03	9,12E-03	7,30E-03	6,57E-05	4,90E-04	6,08E-05	7,64E-03	9,01E-05
9,12E-03	1,03E-02	1,08E-02	8,10E-05	7,25E-04	7,34E-05	1,13E-02	1,10E-04
1,03E-02	1,17E-02	1,24E-02	8,65E-05	8,29E-04	8,03E-05	1,30E-02	1,20E-04
1,17E-02	1,33E-02	9,81E-03	7,75E-05	6,58E-04	7,16E-05	1,06E-02	1,09E-04
1,33E-02	1,50E-02	9,89E-03	7,72E-05	6,64E-04	7,12E-05	1,04E-02	1,06E-04
1,50E-02	1,70E-02	7,92E-03	6,81E-05	5,32E-04	6,33E-05	8,26E-03	9,34E-05
1,70E-02	1,93E-02	1,30E-02	8,96E-05	8,72E-04	8,10E-05	1,34E-02	1,22E-04
1,93E-02	2,19E-02	1,49E-02	9,54E-05	1,00E-03	8,74E-05	1,57E-02	1,32E-04

Middle part of the Interface (neutrons) (second part)							
Energy bins [MeV]		Tally141		Tally151		Tally161	
from	to	Value	σ	Value	σ	Value	σ
2,19E-02	2,48E-02	1,95E-02	1,11E-04	1,31E-03	1,03E-04	2,08E-02	1,54E-04
2,48E-02	2,61E-02	8,77E-03	6,49E-05	5,89E-04	5,99E-05	9,53E-03	9,05E-05
2,61E-02	2,81E-02	3,72E-03	4,21E-05	2,50E-04	3,91E-05	4,13E-03	5,91E-05
2,81E-02	3,18E-02	5,42E-03	5,59E-05	3,64E-04	5,25E-05	6,13E-03	7,97E-05
3,18E-02	4,09E-02	2,03E-02	1,28E-04	1,36E-03	1,18E-04	2,25E-02	1,80E-04
4,09E-02	5,25E-02	2,16E-02	1,32E-04	1,45E-03	1,22E-04	2,42E-02	1,89E-04
5,25E-02	6,74E-02	2,18E-02	1,31E-04	1,46E-03	1,25E-04	2,49E-02	1,92E-04
6,74E-02	8,65E-02	2,25E-02	1,37E-04	1,51E-03	1,29E-04	2,59E-02	1,97E-04
8,65E-02	1,11E-01	1,72E-02	1,17E-04	1,16E-03	1,12E-04	2,04E-02	1,71E-04
1,11E-01	1,43E-01	2,35E-02	1,38E-04	1,58E-03	1,33E-04	2,80E-02	2,07E-04
1,43E-01	1,83E-01	1,68E-02	1,16E-04	1,13E-03	1,12E-04	2,07E-02	1,74E-04
1,83E-01	2,35E-01	1,45E-02	1,08E-04	9,75E-04	1,04E-04	1,80E-02	1,60E-04
2,35E-01	3,02E-01	1,67E-02	1,17E-04	1,12E-03	1,12E-04	2,02E-02	1,74E-04
3,02E-01	3,88E-01	1,49E-02	1,11E-04	1,00E-03	1,06E-04	1,69E-02	1,55E-04
3,88E-01	4,39E-01	5,23E-03	5,60E-05	3,51E-04	5,29E-05	5,35E-03	7,59E-05
4,39E-01	4,98E-01	6,36E-03	6,17E-05	4,27E-04	5,75E-05	5,90E-03	7,96E-05
4,98E-01	5,64E-01	5,12E-03	5,52E-05	3,43E-04	5,16E-05	4,45E-03	6,94E-05
5,64E-01	6,39E-01	4,03E-03	4,96E-05	2,71E-04	4,57E-05	3,13E-03	5,89E-05
6,39E-01	7,24E-01	2,27E-03	3,63E-05	1,52E-04	3,38E-05	1,64E-03	4,18E-05
7,24E-01	8,21E-01	1,15E-03	2,57E-05	7,69E-05	2,44E-05	8,57E-04	2,98E-05
8,21E-01	9,30E-01	9,13E-04	2,30E-05	6,13E-05	2,08E-05	6,70E-04	2,64E-05
9,30E-01	1,05E+00	7,05E-04	2,02E-05	4,73E-05	1,86E-05	4,64E-04	2,16E-05
1,05E+00	1,19E+00	6,07E-04	1,86E-05	4,07E-05	1,65E-05	3,05E-04	1,78E-05
1,19E+00	1,35E+00	3,42E-04	1,36E-05	2,30E-05	1,26E-05	1,30E-04	1,09E-05
1,35E+00	1,74E+00	3,66E-04	1,41E-05	2,46E-05	1,31E-05	1,48E-04	1,26E-05
1,74E+00	2,23E+00	1,68E-04	9,53E-06	1,13E-05	8,34E-06	5,00E-05	7,11E-06
2,23E+00	2,87E+00	7,52E-05	6,32E-06	5,05E-06	5,38E-06	1,48E-05	3,38E-06
2,87E+00	3,68E+00	1,46E-05	2,60E-06	9,78E-07	2,12E-06	5,55E-06	2,05E-06
3,68E+00	4,72E+00	3,73E-06	1,22E-06	2,50E-07	1,29E-06	3,70E-06	1,95E-06
4,72E+00	6,07E+00	1,36E-06	6,79E-07	9,11E-08	9,14E-07	0,00E+00	0,00E+00
6,07E+00	7,79E+00	1,02E-06	5,89E-07	6,84E-08	8,72E-07	1,23E-06	8,71E-07
7,79E+00	1,00E+01	3,39E-07	3,39E-07	2,28E-08	2,76E-07	0,00E+00	0,00E+00
1,00E+01	1,19E+01	0,00E+00	0,00E+00	0,00E+00	0,00E+00	0,00E+00	0,00E+00
1,19E+01	1,35E+01	0,00E+00	0,00E+00	0,00E+00	0,00E+00	0,00E+00	0,00E+00
1,35E+01	1,49E+01	3,38E-07	3,38E-07	2,27E-08	0,00E+00	0,00E+00	0,00E+00
1,49E+01	1,69E+01	0,00E+00	0,00E+00	0,00E+00	0,00E+00	0,00E+00	0,00E+00
1,69E+01	1,96E+01	0,00E+00	0,00E+00	0,00E+00	0,00E+00	0,00E+00	0,00E+00
total	total	1,00E+00	1,90E-03	6,71E-02	1,70E-03	1,00E+00	2,50E-03

Lower part of the Interface (neutrons) (first part)							
Energy bins [MeV]		Tally171		Tally181		Tally191	
from	to	Value	σ	Value	σ	Value	σ
1,00E-12	1,10E-10	0,00E+00	0,00E+00	0,00E+00	0,00E+00	0,00E+00	0,00E+00
1,10E-10	1,53E-07	2,49E-03	1,59E-04	5,80E-03	6,63E-04	1,37E-02	3,27E-03
1,53E-07	4,14E-07	9,39E-03	3,25E-04	1,69E-02	1,25E-03	3,42E-02	5,17E-03
4,14E-07	1,12E-06	2,35E-02	5,53E-04	3,94E-02	1,98E-03	4,24E-02	5,84E-03
1,12E-06	3,06E-06	4,18E-02	7,28E-04	6,71E-02	2,66E-03	8,81E-02	9,34E-03
3,06E-06	5,04E-06	2,82E-02	5,32E-04	3,68E-02	1,68E-03	5,24E-02	6,21E-03
5,04E-06	8,32E-06	3,32E-02	5,77E-04	4,93E-02	2,04E-03	6,04E-02	7,00E-03
8,32E-06	1,37E-05	3,58E-02	5,95E-04	4,78E-02	1,94E-03	6,36E-02	6,91E-03
1,37E-05	2,26E-05	3,93E-02	6,25E-04	4,61E-02	1,89E-03	5,59E-02	6,73E-03
2,26E-05	3,73E-05	3,84E-02	6,17E-04	4,93E-02	1,99E-03	4,72E-02	5,89E-03
3,73E-05	6,14E-05	4,19E-02	6,41E-04	4,92E-02	1,98E-03	5,99E-02	7,01E-03
6,14E-05	1,01E-04	4,57E-02	6,72E-04	5,26E-02	2,00E-03	5,62E-02	6,64E-03
1,01E-04	1,67E-04	4,70E-02	6,91E-04	4,96E-02	1,98E-03	5,56E-02	6,62E-03
1,67E-04	2,75E-04	4,60E-02	6,77E-04	4,91E-02	2,04E-03	6,54E-02	7,37E-03
2,75E-04	3,54E-04	1,51E-02	3,31E-04	1,61E-02	9,81E-04	2,50E-02	3,88E-03
3,54E-04	4,54E-04	1,88E-02	3,72E-04	1,89E-02	1,05E-03	2,05E-02	3,51E-03
4,54E-04	5,83E-04	2,34E-02	4,17E-04	2,37E-02	1,19E-03	2,40E-02	3,80E-03
5,83E-04	7,49E-04	2,46E-02	4,30E-04	2,31E-02	1,17E-03	2,37E-02	3,61E-03
7,49E-04	9,61E-04	2,45E-02	4,29E-04	2,17E-02	1,13E-03	1,50E-02	2,89E-03
9,61E-04	1,09E-03	1,13E-02	2,52E-04	1,01E-02	6,79E-04	8,98E-03	2,15E-03
1,09E-03	1,23E-03	1,15E-02	2,51E-04	1,04E-02	6,74E-04	7,74E-03	1,67E-03
1,23E-03	1,40E-03	1,38E-02	2,82E-04	1,29E-02	7,82E-04	6,98E-03	1,86E-03
1,40E-03	1,58E-03	1,26E-02	2,65E-04	1,10E-02	6,96E-04	3,74E-03	1,30E-03
1,58E-03	1,80E-03	1,29E-02	2,73E-04	1,23E-02	7,76E-04	6,99E-03	1,73E-03
1,80E-03	2,03E-03	1,13E-02	2,49E-04	1,04E-02	6,81E-04	5,99E-03	1,54E-03
2,03E-03	2,31E-03	9,53E-03	2,29E-04	9,30E-03	6,71E-04	4,74E-03	1,30E-03
2,31E-03	2,61E-03	7,26E-03	2,00E-04	6,21E-03	5,20E-04	5,49E-03	1,50E-03
2,61E-03	2,96E-03	1,07E-02	2,47E-04	9,60E-03	6,58E-04	7,98E-03	1,80E-03
2,96E-03	3,35E-03	1,06E-02	2,40E-04	1,09E-02	7,00E-04	9,47E-03	2,17E-03
3,35E-03	3,80E-03	1,07E-02	2,45E-04	9,12E-03	6,37E-04	5,99E-03	1,62E-03
3,80E-03	4,31E-03	8,93E-03	2,23E-04	7,08E-03	5,72E-04	4,99E-03	1,37E-03
4,31E-03	4,88E-03	9,18E-03	2,26E-04	7,03E-03	5,65E-04	6,49E-03	1,58E-03
4,88E-03	5,53E-03	9,44E-03	2,31E-04	7,66E-03	5,88E-04	4,99E-03	1,45E-03
5,53E-03	6,27E-03	8,41E-03	2,15E-04	6,74E-03	5,29E-04	3,25E-03	1,09E-03
6,27E-03	7,10E-03	8,44E-03	2,15E-04	7,51E-03	5,74E-04	3,50E-03	9,99E-04
7,10E-03	8,05E-03	6,44E-03	1,87E-04	5,57E-03	4,90E-04	1,50E-03	7,90E-04
8,05E-03	9,12E-03	7,28E-03	1,98E-04	5,75E-03	4,80E-04	2,74E-03	1,25E-03
9,12E-03	1,03E-02	1,06E-02	2,41E-04	8,10E-03	6,08E-04	3,99E-03	1,32E-03
1,03E-02	1,17E-02	1,15E-02	2,54E-04	8,97E-03	6,34E-04	4,99E-03	1,32E-03
1,17E-02	1,33E-02	9,24E-03	2,26E-04	8,02E-03	6,14E-04	5,24E-03	1,71E-03
1,33E-02	1,50E-02	9,15E-03	2,22E-04	7,23E-03	5,62E-04	2,00E-03	9,33E-04
1,50E-02	1,70E-02	7,54E-03	2,04E-04	5,47E-03	4,87E-04	1,50E-03	6,11E-04
1,70E-02	1,93E-02	1,13E-02	2,49E-04	9,02E-03	6,63E-04	3,99E-03	1,17E-03
1,93E-02	2,19E-02	1,38E-02	2,81E-04	9,93E-03	6,85E-04	5,49E-03	1,83E-03

Lower part of the Interface (neutrons) (second part)							
Energy bins [MeV]		Tally171		Tally181		Tally191	
from	to	Value	σ	Value	σ	Value	σ
2,19E-02	2,48E-02	1,79E-02	3,22E-04	1,21E-02	7,55E-04	5,99E-03	1,54E-03
2,48E-02	2,61E-02	7,85E-03	1,85E-04	4,98E-03	4,19E-04	2,99E-03	1,06E-03
2,61E-02	2,81E-02	3,70E-03	1,25E-04	2,58E-03	2,90E-04	1,50E-03	6,11E-04
2,81E-02	3,18E-02	5,37E-03	1,68E-04	3,83E-03	4,10E-04	9,99E-04	4,99E-04
3,18E-02	4,09E-02	1,88E-02	3,73E-04	1,28E-02	9,03E-04	5,73E-03	1,81E-03
4,09E-02	5,25E-02	1,99E-02	3,83E-04	1,24E-02	8,18E-04	6,49E-03	2,00E-03
5,25E-02	6,74E-02	1,98E-02	3,78E-04	1,21E-02	8,66E-04	8,98E-03	2,03E-03
6,74E-02	8,65E-02	2,07E-02	4,03E-04	1,29E-02	8,82E-04	5,24E-03	1,64E-03
8,65E-02	1,11E-01	1,56E-02	3,37E-04	9,48E-03	7,53E-04	9,48E-03	2,57E-03
1,11E-01	1,43E-01	2,06E-02	3,99E-04	1,16E-02	8,39E-04	6,23E-03	1,74E-03
1,43E-01	1,83E-01	1,44E-02	3,23E-04	8,12E-03	6,85E-04	2,74E-03	9,66E-04
1,83E-01	2,35E-01	1,20E-02	2,89E-04	5,57E-03	5,57E-04	4,00E-03	1,32E-03
2,35E-01	3,02E-01	1,27E-02	3,11E-04	4,93E-03	5,54E-04	2,50E-03	9,34E-04
3,02E-01	3,88E-01	9,13E-03	2,56E-04	4,22E-03	4,77E-04	2,99E-03	1,36E-03
3,88E-01	4,39E-01	2,56E-03	1,19E-04	1,30E-03	2,27E-04	1,50E-03	7,88E-04
4,39E-01	4,98E-01	2,80E-03	1,24E-04	9,71E-04	1,84E-04	9,96E-04	6,10E-04
4,98E-01	5,64E-01	1,68E-03	9,56E-05	6,13E-04	1,73E-04	0,00E+00	0,00E+00
5,64E-01	6,39E-01	1,06E-03	7,80E-05	3,07E-04	1,02E-04	0,00E+00	0,00E+00
6,39E-01	7,24E-01	4,46E-04	4,64E-05	1,02E-04	5,11E-05	0,00E+00	0,00E+00
7,24E-01	8,21E-01	2,47E-04	3,93E-05	1,02E-04	1,02E-04	0,00E+00	0,00E+00
8,21E-01	9,30E-01	1,33E-04	2,41E-05	2,56E-05	2,56E-05	0,00E+00	0,00E+00
9,30E-01	1,05E+00	5,06E-05	1,42E-05	5,13E-05	5,13E-05	0,00E+00	0,00E+00
1,05E+00	1,19E+00	5,06E-05	2,00E-05	0,00E+00	0,00E+00	0,00E+00	0,00E+00
1,19E+00	1,35E+00	1,58E-05	8,37E-06	0,00E+00	0,00E+00	0,00E+00	0,00E+00
1,35E+00	1,74E+00	2,22E-05	1,05E-05	0,00E+00	0,00E+00	0,00E+00	0,00E+00
1,74E+00	2,23E+00	0,00E+00	0,00E+00	0,00E+00	0,00E+00	0,00E+00	0,00E+00
2,23E+00	2,87E+00	0,00E+00	0,00E+00	0,00E+00	0,00E+00	0,00E+00	0,00E+00
2,87E+00	3,68E+00	0,00E+00	0,00E+00	0,00E+00	0,00E+00	0,00E+00	0,00E+00
3,68E+00	4,72E+00	0,00E+00	0,00E+00	0,00E+00	0,00E+00	0,00E+00	0,00E+00
4,72E+00	6,07E+00	0,00E+00	0,00E+00	0,00E+00	0,00E+00	0,00E+00	0,00E+00
6,07E+00	7,79E+00	0,00E+00	0,00E+00	0,00E+00	0,00E+00	0,00E+00	0,00E+00
7,79E+00	1,00E+01	0,00E+00	0,00E+00	0,00E+00	0,00E+00	0,00E+00	0,00E+00
1,00E+01	1,19E+01	0,00E+00	0,00E+00	0,00E+00	0,00E+00	0,00E+00	0,00E+00
1,19E+01	1,35E+01	0,00E+00	0,00E+00	0,00E+00	0,00E+00	0,00E+00	0,00E+00
1,35E+01	1,49E+01	0,00E+00	0,00E+00	0,00E+00	0,00E+00	0,00E+00	0,00E+00
1,49E+01	1,69E+01	0,00E+00	0,00E+00	0,00E+00	0,00E+00	0,00E+00	0,00E+00
1,69E+01	1,96E+01	0,00E+00	0,00E+00	0,00E+00	0,00E+00	0,00E+00	0,00E+00
total	total	1,00E+00	5,60E-03	1,00E+00	1,54E-02	1,00E+00	4,72E-02

Entire Interface (photons) (first part)			
Energy bins [MeV]		Tally101	
from	to	Value	σ
1,00E-12	1,10E-10	0,00E+00	0,00E+00
1,10E-10	1,53E-07	0,00E+00	0,00E+00
1,53E-07	4,14E-07	0,00E+00	0,00E+00
4,14E-07	1,12E-06	0,00E+00	0,00E+00
1,12E-06	3,06E-06	0,00E+00	0,00E+00
3,06E-06	5,04E-06	0,00E+00	0,00E+00
5,04E-06	8,32E-06	0,00E+00	0,00E+00
8,32E-06	1,37E-05	0,00E+00	0,00E+00
1,37E-05	2,26E-05	0,00E+00	0,00E+00
2,26E-05	3,73E-05	0,00E+00	0,00E+00
3,73E-05	6,14E-05	0,00E+00	0,00E+00
6,14E-05	1,01E-04	0,00E+00	0,00E+00
1,01E-04	1,67E-04	0,00E+00	0,00E+00
1,67E-04	2,75E-04	0,00E+00	0,00E+00
2,75E-04	3,54E-04	0,00E+00	0,00E+00
3,54E-04	4,54E-04	0,00E+00	0,00E+00
4,54E-04	5,83E-04	0,00E+00	0,00E+00
5,83E-04	7,49E-04	0,00E+00	0,00E+00
7,49E-04	9,61E-04	0,00E+00	0,00E+00
9,61E-04	1,09E-03	0,00E+00	0,00E+00
1,09E-03	1,23E-03	0,00E+00	0,00E+00
1,23E-03	1,40E-03	0,00E+00	0,00E+00
1,40E-03	1,58E-03	0,00E+00	0,00E+00
1,58E-03	1,80E-03	0,00E+00	0,00E+00
1,80E-03	2,03E-03	0,00E+00	0,00E+00
2,03E-03	2,31E-03	0,00E+00	0,00E+00
2,31E-03	2,61E-03	7,36E-06	7,36E-06
2,61E-03	2,96E-03	0,00E+00	0,00E+00
2,96E-03	3,35E-03	0,00E+00	0,00E+00
3,35E-03	3,80E-03	0,00E+00	0,00E+00
3,80E-03	4,31E-03	0,00E+00	0,00E+00
4,31E-03	4,88E-03	0,00E+00	0,00E+00
4,88E-03	5,53E-03	1,48E-05	1,04E-05
5,53E-03	6,27E-03	7,41E-06	7,41E-06
6,27E-03	7,10E-03	7,43E-06	7,43E-06
7,10E-03	8,05E-03	7,43E-06	7,43E-06
8,05E-03	9,12E-03	7,38E-06	7,38E-06
9,12E-03	1,03E-02	0,00E+00	0,00E+00
1,03E-02	1,17E-02	4,04E-04	5,84E-05
1,17E-02	1,33E-02	0,00E+00	0,00E+00
1,33E-02	1,50E-02	1,48E-05	1,05E-05
1,50E-02	1,70E-02	7,45E-06	7,45E-06

Entire Interface (photons) (second part)			
Energy bins [MeV]		Tally101	
from	to	Value	σ
1,70E-02	1,93E-02	2,22E-05	1,28E-05
1,93E-02	2,19E-02	7,41E-06	7,41E-06
2,19E-02	2,48E-02	2,82E-05	1,65E-05
2,48E-02	2,61E-02	1,48E-05	1,05E-05
2,61E-02	2,81E-02	7,44E-06	7,44E-06
2,81E-02	3,18E-02	5,98E-05	2,11E-05
3,18E-02	4,09E-02	1,74E-04	3,89E-05
4,09E-02	5,25E-02	4,50E-04	6,28E-05
5,25E-02	6,74E-02	1,78E-03	1,30E-04
6,74E-02	8,65E-02	2,54E-02	4,94E-04
8,65E-02	1,11E-01	9,64E-03	2,96E-04
1,11E-01	1,43E-01	2,40E-02	4,78E-04
1,43E-01	1,83E-01	4,01E-02	6,26E-04
1,83E-01	2,35E-01	5,72E-02	7,44E-04
2,35E-01	3,02E-01	6,33E-02	7,91E-04
3,02E-01	3,88E-01	6,86E-02	8,23E-04
3,88E-01	4,39E-01	3,29E-02	5,63E-04
4,39E-01	4,98E-01	3,49E-02	5,76E-04
4,98E-01	5,64E-01	1,02E-01	9,93E-04
5,64E-01	6,39E-01	2,19E-02	4,65E-04
6,39E-01	7,24E-01	2,25E-02	4,78E-04
7,24E-01	8,21E-01	2,82E-02	5,41E-04
8,21E-01	9,30E-01	3,82E-02	6,27E-04
9,30E-01	1,05E+00	1,71E-02	4,15E-04
1,05E+00	1,19E+00	1,72E-02	4,17E-04
1,19E+00	1,35E+00	1,87E-02	4,30E-04
1,35E+00	1,74E+00	4,31E-02	6,55E-04
1,74E+00	2,23E+00	4,02E-02	6,39E-04
2,23E+00	2,87E+00	4,33E-02	6,62E-04
2,87E+00	3,68E+00	4,19E-02	6,54E-04
3,68E+00	4,72E+00	4,11E-02	6,41E-04
4,72E+00	6,07E+00	4,78E-02	6,55E-04
6,07E+00	7,79E+00	7,86E-02	8,33E-04
7,79E+00	1,00E+01	3,88E-02	5,59E-04
1,00E+01	1,19E+01	2,97E-05	1,49E-05
1,19E+01	1,35E+01	0,00E+00	0,00E+00
1,35E+01	1,49E+01	0,00E+00	0,00E+00
1,49E+01	1,69E+01	0,00E+00	0,00E+00
1,69E+01	1,96E+01	0,00E+00	0,00E+00
total	total	1,00E+00	4,40E-03

Neutron Fluxes results tables

Tables of the SDEF Approach results

SDEF: Upper part: Tally 404, 414, 424, 434 (neutrons) (first part)								
	Tally 404		Tally 414		Tally 424		Tally 434	
	Normalized Values [a.u]							
Upper bin	Value	σ	Value	σ	Value	σ	Value	σ
1,00E-12	0,00E+00	0,00E+00	0,00E+00	0,00E+00	0,00E+00	0,00E+00	0,00E+00	0,00E+00
1,80E-12	0,00E+00	0,00E+00	0,00E+00	0,00E+00	0,00E+00	0,00E+00	0,00E+00	0,00E+00
3,23E-12	0,00E+00	0,00E+00	0,00E+00	0,00E+00	0,00E+00	0,00E+00	0,00E+00	0,00E+00
5,82E-12	0,00E+00	0,00E+00	0,00E+00	0,00E+00	0,00E+00	0,00E+00	0,00E+00	0,00E+00
1,05E-11	0,00E+00	0,00E+00	0,00E+00	0,00E+00	0,00E+00	0,00E+00	0,00E+00	0,00E+00
1,88E-11	0,00E+00	0,00E+00	0,00E+00	0,00E+00	0,00E+00	0,00E+00	0,00E+00	0,00E+00
3,38E-11	0,00E+00	0,00E+00	0,00E+00	0,00E+00	0,00E+00	0,00E+00	0,00E+00	0,00E+00
6,09E-11	0,00E+00	0,00E+00	0,00E+00	0,00E+00	0,00E+00	0,00E+00	0,00E+00	0,00E+00
1,09E-10	0,00E+00	0,00E+00	0,00E+00	0,00E+00	0,00E+00	0,00E+00	0,00E+00	0,00E+00
1,97E-10	4,11E-05	0,00E+00	0,00E+00	0,00E+00	0,00E+00	0,00E+00	0,00E+00	0,00E+00
3,54E-10	2,85E-05	0,00E+00	0,00E+00	0,00E+00	0,00E+00	0,00E+00	0,00E+00	0,00E+00
6,37E-10	1,50E-04	0,00E+00	0,00E+00	0,00E+00	0,00E+00	0,00E+00	0,00E+00	0,00E+00
1,15E-09	4,73E-04	0,00E+00	0,00E+00	0,00E+00	0,00E+00	0,00E+00	0,00E+00	0,00E+00
2,06E-09	1,43E-03	0,00E+00	0,00E+00	0,00E+00	0,00E+00	0,00E+00	0,00E+00	0,00E+00
3,70E-09	4,16E-03	2,60E-03	3,66E-03	3,66E-03	0,00E+00	0,00E+00	1,39E-03	1,39E-03
6,66E-09	1,17E-02	1,09E-02	9,35E-03	9,35E-03	1,09E-03	8,06E-04	1,62E-03	1,62E-03
1,20E-08	3,41E-02	2,29E-02	3,72E-02	1,71E-02	9,33E-03	3,31E-03	2,20E-02	9,40E-03
2,15E-08	8,22E-02	3,03E-02	4,86E-02	1,28E-02	1,82E-02	7,49E-03	3,70E-02	1,39E-02
3,87E-08	1,58E-01	3,95E-02	1,19E-01	2,64E-02	7,37E-01	7,04E-01	9,64E-02	2,36E-02
6,97E-08	2,15E-01	3,87E-02	1,83E-01	3,13E-02	6,28E-02	1,91E-02	1,38E-01	2,68E-02
1,25E-07	1,59E-01	4,48E-02	1,17E-01	2,94E-02	5,04E-02	1,29E-02	7,01E-02	1,90E-02
2,25E-07	5,94E-02	2,13E-02	3,99E-02	1,10E-02	1,42E-02	4,79E-03	3,88E-02	1,03E-02
4,05E-07	3,04E-02	1,72E-02	2,73E-02	9,68E-03	5,04E-03	2,67E-03	4,26E-02	1,33E-02
7,29E-07	2,89E-02	1,43E-02	7,60E-02	4,14E-02	1,83E-02	9,95E-03	5,36E-02	1,33E-02
1,31E-06	2,78E-02	9,60E-03	2,25E-02	7,48E-03	7,57E-03	4,48E-03	4,88E-02	1,31E-02
2,36E-06	2,62E-02	6,46E-03	3,04E-02	9,96E-03	1,74E-02	7,67E-03	8,47E-02	1,85E-02
4,24E-06	2,49E-02	1,92E-02	4,54E-02	1,33E-02	7,08E-03	3,84E-03	3,34E-02	9,03E-03
7,63E-06	2,20E-02	4,89E-03	2,50E-02	7,96E-03	7,81E-03	3,34E-03	5,16E-02	1,24E-02
1,37E-05	1,95E-02	1,97E-02	2,24E-02	6,97E-03	1,37E-02	5,23E-03	4,75E-02	1,11E-02
2,47E-05	1,69E-02	4,04E-02	1,18E-02	4,46E-03	4,43E-03	2,57E-03	2,93E-02	8,20E-03
4,44E-05	1,51E-02	5,27E-03	1,73E-02	7,98E-03	2,68E-03	1,61E-03	3,97E-02	8,92E-03
7,98E-05	1,19E-02	4,75E-03	1,52E-02	7,04E-03	3,13E-03	1,95E-03	2,54E-02	8,65E-03
1,44E-04	8,50E-03	1,02E-02	2,41E-02	7,38E-03	3,86E-03	3,32E-03	1,72E-02	7,64E-03
2,58E-04	7,15E-03	1,47E-03	1,59E-02	6,20E-03	5,35E-03	3,04E-03	6,07E-03	3,13E-03
4,64E-04	5,42E-03	2,18E-03	8,80E-03	4,19E-03	0,00E+00	0,00E+00	7,52E-03	3,89E-03
8,35E-04	5,55E-03	7,39E-03	2,25E-02	8,37E-03	4,68E-03	2,31E-03	1,17E-02	5,14E-03
1,50E-03	5,24E-03	1,47E-03	3,25E-02	1,42E-02	5,08E-04	5,08E-04	1,61E-02	6,71E-03
2,70E-03	4,32E-03	9,74E-04	1,16E-02	7,50E-03	9,53E-04	7,59E-04	1,45E-02	8,46E-03

SDER: Upper part: Tally 404, 414, 424, 434 (neutrons) (second part)									
	Tally 404		Tally 414		Tally 424		Tally 434		
	Normalized Values [a.u]								
Upper bin	Value	σ	Value	σ	Value	σ	Value	σ	
4,86E-03	3,63E-03	6,44E-03	3,42E-03	1,75E-03	2,93E-03	2,31E-03	1,00E-02	3,58E-03	
8,73E-03	3,09E-03	1,04E-02	1,31E-02	5,05E-03	2,70E-04	2,70E-04	2,46E-02	7,92E-03	
1,57E-02	2,94E-03	0,00E+00	9,28E-03	4,71E-03	3,39E-04	3,39E-04	1,52E-02	6,06E-03	
2,82E-02	1,98E-03	8,60E-04	6,16E-03	2,88E-03	0,00E+00	0,00E+00	3,17E-03	2,27E-03	
5,08E-02	9,54E-04	2,94E-03	0,00E+00	0,00E+00	0,00E+00	0,00E+00	2,11E-03	1,57E-03	
9,14E-02	9,06E-04	0,00E+00	2,08E-03	1,53E-03	1,39E-04	1,39E-04	6,77E-03	3,55E-03	
1,64E-01	1,07E-03	2,18E-03	0,00E+00	0,00E+00	1,31E-04	1,31E-04	1,28E-03	1,28E-03	
2,96E-01	3,72E-04	0,00E+00	3,76E-04	3,76E-04	0,00E+00	0,00E+00	1,94E-03	1,17E-03	
5,31E-01	1,05E-04	0,00E+00	0,00E+00	0,00E+00	1,49E-04	1,49E-04	0,00E+00	0,00E+00	
9,56E-01	0,00E+00	0,00E+00	0,00E+00	0,00E+00	0,00E+00	0,00E+00	0,00E+00	0,00E+00	
1,72E+00	0,00E+00	0,00E+00	0,00E+00	0,00E+00	0,00E+00	0,00E+00	0,00E+00	0,00E+00	
3,09E+00	0,00E+00	0,00E+00	0,00E+00	0,00E+00	0,00E+00	0,00E+00	0,00E+00	0,00E+00	
5,56E+00	0,00E+00	0,00E+00	0,00E+00	0,00E+00	0,00E+00	0,00E+00	0,00E+00	0,00E+00	
1,00E+01	0,00E+00	0,00E+00	0,00E+00	0,00E+00	0,00E+00	0,00E+00	0,00E+00	0,00E+00	
total	1,00E+00	1,20E-01	1,00E+00	9,65E-02	1,00E+00	7,26E-01	1,00E+00	7,70E-02	

SDEF: Upper part: Tally 444, 445 (neutrons) (first part)				
	Tally 444		Tally 454	
	Normalized Values [a.u]			
Upper bin	Value	σ	Value	σ
1,00E-12	0,00E+00	0,00E+00	0,00E+00	0,00E+00
1,80E-12	0,00E+00	0,00E+00	0,00E+00	0,00E+00
3,23E-12	0,00E+00	0,00E+00	0,00E+00	0,00E+00
5,82E-12	0,00E+00	0,00E+00	0,00E+00	0,00E+00
1,05E-11	0,00E+00	0,00E+00	0,00E+00	0,00E+00
1,88E-11	0,00E+00	0,00E+00	0,00E+00	0,00E+00
3,38E-11	0,00E+00	0,00E+00	0,00E+00	0,00E+00
6,09E-11	0,00E+00	0,00E+00	0,00E+00	0,00E+00
1,09E-10	0,00E+00	0,00E+00	0,00E+00	0,00E+00
1,97E-10	0,00E+00	0,00E+00	0,00E+00	0,00E+00
3,54E-10	0,00E+00	0,00E+00	0,00E+00	0,00E+00
6,37E-10	0,00E+00	0,00E+00	0,00E+00	0,00E+00
1,15E-09	0,00E+00	0,00E+00	0,00E+00	0,00E+00
2,06E-09	0,00E+00	0,00E+00	0,00E+00	0,00E+00
3,70E-09	4,42E-03	4,42E-03	0,00E+00	0,00E+00
6,66E-09	3,23E-03	3,23E-03	0,00E+00	0,00E+00
1,20E-08	2,02E-02	1,02E-02	5,40E-03	3,16E-03
2,15E-08	5,05E-02	1,44E-02	3,54E-02	1,36E-02
3,87E-08	8,60E-02	3,02E-02	1,48E-01	9,44E-02
6,97E-08	2,15E-01	5,12E-02	1,36E-01	4,33E-02
1,25E-07	1,15E-01	2,72E-02	9,32E-02	1,86E-02
2,25E-07	6,36E-02	2,93E-02	6,14E-02	1,59E-02
4,05E-07	2,77E-02	1,59E-02	6,60E-02	2,00E-02
7,29E-07	4,24E-02	1,78E-02	4,42E-02	1,27E-02
1,31E-06	4,60E-02	1,56E-02	5,29E-02	1,37E-02
2,36E-06	5,04E-02	2,35E-02	3,55E-02	1,09E-02
4,24E-06	1,92E-02	7,87E-03	6,67E-02	1,71E-02
7,63E-06	6,60E-02	4,59E-02	5,53E-02	1,51E-02
1,37E-05	4,14E-02	1,74E-02	4,04E-02	1,50E-02
2,47E-05	4,55E-02	2,21E-02	1,97E-02	8,36E-03
4,44E-05	1,68E-02	6,99E-03	1,47E-02	8,35E-03
7,98E-05	1,28E-02	6,12E-03	1,25E-02	6,29E-03
1,44E-04	9,88E-03	6,38E-03	1,25E-02	6,16E-03
2,58E-04	6,37E-03	4,39E-03	9,12E-03	5,36E-03
4,64E-04	1,01E-02	5,03E-03	7,61E-03	4,76E-03
8,35E-04	2,70E-02	2,58E-02	1,22E-03	8,75E-04
1,50E-03	6,66E-04	6,66E-04	1,31E-02	4,59E-03
2,70E-03	0,00E+00	0,00E+00	1,35E-02	6,19E-03
4,86E-03	1,57E-03	1,12E-03	1,59E-02	5,49E-03
8,73E-03	1,27E-02	8,11E-03	1,09E-02	5,49E-03
1,57E-02	3,23E-03	2,29E-03	1,40E-02	4,51E-03
2,82E-02	8,24E-04	8,24E-04	1,95E-03	1,26E-03

SDEF: Upper part: Tally 444, 445 (neutrons) (second part)				
	Tally 444		Tally 454	
	Normalized Values [a.u]			
Upper bin	Value	σ	Value	σ
5,08E-02	1,68E-03	1,68E-03	5,53E-03	3,55E-03
9,14E-02	0,00E+00	0,00E+00	4,45E-03	2,59E-03
1,64E-01	0,00E+00	0,00E+00	0,00E+00	0,00E+00
2,96E-01	0,00E+00	0,00E+00	2,92E-03	2,18E-03
5,31E-01	0,00E+00	0,00E+00	0,00E+00	0,00E+00
9,56E-01	0,00E+00	0,00E+00	0,00E+00	0,00E+00
1,72E+00	0,00E+00	0,00E+00	0,00E+00	0,00E+00
3,09E+00	0,00E+00	0,00E+00	0,00E+00	0,00E+00
5,56E+00	0,00E+00	0,00E+00	0,00E+00	0,00E+00
1,00E+01	0,00E+00	0,00E+00	0,00E+00	0,00E+00
total	1,00E+00	1,26E-01	1,00E+00	1,54E-01

SDEF: Lower part (neutrons) (first part)						
	Tally 464		Tally 474		Tally 484	
	Normalized Values [a.u]					
Upper bin	Value	σ	Value	σ	Value	σ
1,00E-12	0,00E+00	0,00E+00	0,00E+00	0,00E+00	0,00E+00	0,00E+00
1,80E-12	0,00E+00	0,00E+00	0,00E+00	0,00E+00	0,00E+00	0,00E+00
3,23E-12	0,00E+00	0,00E+00	0,00E+00	0,00E+00	0,00E+00	0,00E+00
5,82E-12	0,00E+00	0,00E+00	0,00E+00	0,00E+00	0,00E+00	0,00E+00
1,05E-11	0,00E+00	0,00E+00	0,00E+00	0,00E+00	0,00E+00	0,00E+00
1,88E-11	0,00E+00	0,00E+00	0,00E+00	0,00E+00	0,00E+00	0,00E+00
3,38E-11	0,00E+00	0,00E+00	0,00E+00	0,00E+00	0,00E+00	0,00E+00
6,09E-11	0,00E+00	0,00E+00	0,00E+00	0,00E+00	0,00E+00	0,00E+00
1,09E-10	0,00E+00	0,00E+00	0,00E+00	0,00E+00	0,00E+00	0,00E+00
1,97E-10	4,11E-05	2,12E-05	4,25E-06	3,25E-06	9,27E-06	9,27E-06
3,54E-10	2,85E-05	1,39E-05	2,55E-05	1,20E-05	3,12E-05	1,38E-05
6,37E-10	1,50E-04	3,36E-05	6,97E-05	1,85E-05	8,05E-05	1,96E-05
1,15E-09	4,73E-04	7,77E-05	1,94E-04	3,42E-05	2,63E-04	4,00E-05
2,06E-09	1,43E-03	1,27E-04	8,30E-04	8,29E-05	7,50E-04	6,97E-05
3,70E-09	4,16E-03	2,16E-04	2,05E-03	1,11E-04	2,43E-03	1,38E-04
6,66E-09	1,17E-02	3,74E-04	7,22E-03	2,85E-04	7,08E-03	2,38E-04
1,20E-08	3,41E-02	6,99E-04	1,93E-02	4,90E-04	2,16E-02	6,99E-04
2,15E-08	8,22E-02	1,31E-03	4,99E-02	1,09E-03	5,22E-02	1,11E-03
3,87E-08	1,58E-01	2,15E-03	9,78E-02	1,90E-03	1,06E-01	2,14E-03
6,97E-08	2,15E-01	2,84E-03	1,35E-01	2,54E-03	1,44E-01	2,88E-03
1,25E-07	1,59E-01	2,19E-03	1,04E-01	2,07E-03	1,13E-01	2,35E-03
2,25E-07	5,94E-02	1,07E-03	4,84E-02	1,13E-03	5,08E-02	1,18E-03
4,05E-07	3,04E-02	7,43E-04	3,65E-02	1,01E-03	3,54E-02	9,50E-04
7,29E-07	2,89E-02	7,54E-04	4,04E-02	1,19E-03	3,74E-02	1,05E-03
1,31E-06	2,78E-02	7,49E-04	4,49E-02	1,29E-03	4,29E-02	1,30E-03
2,36E-06	2,62E-02	7,43E-04	4,64E-02	1,44E-03	4,45E-02	1,35E-03
4,24E-06	2,49E-02	7,41E-04	4,76E-02	1,65E-03	4,32E-02	1,46E-03
7,63E-06	2,20E-02	6,92E-04	4,32E-02	1,63E-03	4,12E-02	1,52E-03
1,37E-05	1,95E-02	7,06E-04	3,83E-02	1,54E-03	3,58E-02	1,41E-03
2,47E-05	1,69E-02	6,15E-04	3,47E-02	1,57E-03	3,41E-02	1,48E-03
4,44E-05	1,51E-02	6,44E-04	2,94E-02	1,42E-03	2,95E-02	1,46E-03
7,98E-05	1,19E-02	5,26E-04	2,51E-02	1,38E-03	2,49E-02	1,27E-03
1,44E-04	8,50E-03	4,33E-04	2,08E-02	1,24E-03	2,07E-02	1,22E-03
2,58E-04	7,15E-03	3,90E-04	1,56E-02	9,80E-04	1,55E-02	9,70E-04
4,64E-04	5,42E-03	3,24E-04	1,00E-02	7,00E-04	1,06E-02	7,14E-04
8,35E-04	5,55E-03	3,33E-04	1,45E-02	1,07E-03	1,39E-02	9,58E-04
1,50E-03	5,24E-03	3,34E-04	1,21E-02	9,63E-04	1,18E-02	8,79E-04
2,70E-03	4,32E-03	2,91E-04	9,29E-03	8,46E-04	8,70E-03	7,44E-04
4,86E-03	3,63E-03	3,00E-04	1,23E-02	1,31E-03	1,05E-02	9,50E-04
8,73E-03	3,09E-03	2,45E-04	1,27E-02	1,39E-03	9,80E-03	9,87E-04
1,57E-02	2,94E-03	2,33E-04	1,40E-02	1,69E-03	1,11E-02	1,34E-03
2,82E-02	1,98E-03	2,83E-04	9,48E-03	1,51E-03	7,53E-03	1,01E-03

SDEF: Lower part (neutrons) (second part)						
	Tally 464		Tally 474		Tally 484	
	Normalized Values [a.u]					
Upper bin	Value	σ	Value	σ	Value	σ
5,08E-02	9,54E-04	1,39E-04	3,82E-03	6,92E-04	3,28E-03	5,31E-04
9,14E-02	9,06E-04	1,31E-04	6,33E-03	1,13E-03	3,70E-03	5,85E-04
1,64E-01	1,07E-03	3,83E-04	5,20E-03	9,25E-04	3,86E-03	6,24E-04
2,96E-01	3,72E-04	9,04E-05	1,82E-03	3,89E-04	1,90E-03	3,69E-04
5,31E-01	1,05E-04	4,25E-05	6,01E-04	1,99E-04	5,00E-04	1,50E-04
9,56E-01	0,00E+00	0,00E+00	2,36E-05	2,36E-05	0,00E+00	0,00E+00
1,72E+00	0,00E+00	0,00E+00	0,00E+00	0,00E+00	0,00E+00	0,00E+00
3,09E+00	0,00E+00	0,00E+00	0,00E+00	0,00E+00	0,00E+00	0,00E+00
5,56E+00	0,00E+00	0,00E+00	0,00E+00	0,00E+00	0,00E+00	0,00E+00
1,00E+01	0,00E+00	0,00E+00	0,00E+00	0,00E+00	0,00E+00	0,00E+00
total	1,00E+00	1,24E-02	1,00E+00	2,61E-02	1,00E+00	2,54E-02

SDEF: Shortest path through lead (photons)		
	Tally 104	
	Normalized Values [a.u]	
Upper bin	Value	σ
1,00E-03	0,00E+00	0,00E+00
1,21E-03	0,00E+00	0,00E+00
1,47E-03	0,00E+00	0,00E+00
1,79E-03	0,00E+00	0,00E+00
2,17E-03	0,00E+00	0,00E+00
2,63E-03	0,00E+00	0,00E+00
3,19E-03	0,00E+00	0,00E+00
3,87E-03	0,00E+00	0,00E+00
4,69E-03	0,00E+00	0,00E+00
5,69E-03	0,00E+00	0,00E+00
6,90E-03	0,00E+00	0,00E+00
8,37E-03	0,00E+00	0,00E+00
1,02E-02	0,00E+00	0,00E+00
1,23E-02	0,00E+00	0,00E+00
1,49E-02	1,88E-05	1,88E-05
1,81E-02	1,88E-05	1,88E-05
2,20E-02	0,00E+00	0,00E+00
2,67E-02	0,00E+00	0,00E+00
3,24E-02	0,00E+00	0,00E+00
3,93E-02	0,00E+00	0,00E+00
4,76E-02	2,31E-04	1,35E-04
5,78E-02	4,63E-04	2,43E-04
7,01E-02	4,66E-04	2,76E-04
8,50E-02	3,86E-03	3,64E-03
1,03E-01	4,79E-05	4,79E-05
1,25E-01	1,74E-04	1,23E-04
1,52E-01	0,00E+00	0,00E+00
1,84E-01	2,69E-03	2,45E-03
2,23E-01	1,24E-03	4,29E-04
2,71E-01	4,02E-03	9,08E-04
3,29E-01	5,18E-03	1,15E-03
3,99E-01	9,77E-03	1,59E-03
4,84E-01	1,80E-02	1,60E-03
5,87E-01	4,67E-02	2,90E-03
7,12E-01	4,09E-02	2,48E-03
8,64E-01	5,52E-02	3,05E-03
1,05E+00	7,39E-02	3,80E-03
1,27E+00	9,48E-02	4,60E-03
1,54E+00	1,26E-01	6,27E-03
1,87E+00	1,35E-01	6,86E-03
2,27E+00	1,40E-01	8,20E-03
2,75E+00	1,18E-01	8,92E-03

SDEF: Shortest path through lead (photons)		
	Tally 104	
	Normalized Values [a.u]	
Upper bin	Value	σ
3,34E+00	7,70E-02	8,38E-03
4,05E+00	2,78E-02	4,48E-03
4,91E+00	1,53E-02	3,99E-03
5,96E+00	1,59E-03	1,21E-03
7,23E+00	1,62E-03	1,45E-03
8,77E+00	0,00E+00	0,00E+00
1,06E+01	0,00E+00	0,00E+00
1,29E+01	0,00E+00	0,00E+00
1,57E+01	0,00E+00	0,00E+00
1,90E+01	0,00E+00	0,00E+00
total	1,00E+00	2,87E-02

Tables of the SSR/SSW Approach results

SSR/SSW: Upper part: Tally 404, 414, 424, 434 (neutrons) (first part)								
	Tally 404		Tally 414		Tally 424		Tally 434	
	Normalized Values [a.u]							
Upper bin	Value	σ	Value	σ	Value	σ	Value	σ
1,00E-12	0,00E+00	0,00E+00	0,00E+00	0,00E+00	0,00E+00	0,00E+00	0,00E+00	0,00E+00
1,80E-12	0,00E+00	0,00E+00	0,00E+00	0,00E+00	0,00E+00	0,00E+00	0,00E+00	0,00E+00
3,23E-12	0,00E+00	0,00E+00	0,00E+00	0,00E+00	0,00E+00	0,00E+00	0,00E+00	0,00E+00
5,82E-12	0,00E+00	0,00E+00	0,00E+00	0,00E+00	0,00E+00	0,00E+00	0,00E+00	0,00E+00
1,05E-11	0,00E+00	0,00E+00	0,00E+00	0,00E+00	0,00E+00	0,00E+00	0,00E+00	0,00E+00
1,88E-11	0,00E+00	0,00E+00	0,00E+00	0,00E+00	0,00E+00	0,00E+00	0,00E+00	0,00E+00
3,38E-11	0,00E+00	0,00E+00	0,00E+00	0,00E+00	0,00E+00	0,00E+00	0,00E+00	0,00E+00
6,09E-11	0,00E+00	0,00E+00	1,26E-07	1,26E-07	3,93E-05	3,93E-05	0,00E+00	0,00E+00
1,09E-10	0,00E+00	0,00E+00	0,00E+00	0,00E+00	0,00E+00	0,00E+00	0,00E+00	0,00E+00
1,97E-10	0,00E+00	0,00E+00	1,14E-05	8,14E-06	0,00E+00	0,00E+00	3,88E-05	3,88E-05
3,54E-10	1,69E-04	1,22E-04	1,40E-04	1,08E-04	1,76E-05	1,76E-05	0,00E+00	0,00E+00
6,37E-10	1,37E-04	4,70E-05	9,40E-05	3,40E-05	3,55E-05	2,36E-05	7,64E-05	4,35E-05
1,15E-09	2,62E-04	6,89E-05	2,52E-04	7,07E-05	1,71E-04	7,54E-05	3,40E-04	1,31E-04
2,06E-09	1,17E-02	1,07E-02	7,62E-04	1,63E-04	2,02E-03	5,82E-04	1,00E-03	2,11E-04
3,70E-09	3,82E-03	1,15E-03	2,98E-03	4,06E-04	3,16E-03	6,06E-04	2,27E-03	3,83E-04
6,66E-09	1,93E-02	1,15E-02	8,97E-03	1,05E-03	8,96E-03	1,18E-03	7,37E-03	8,03E-04
1,20E-08	3,92E-02	1,60E-02	2,86E-02	6,04E-03	3,89E-02	1,56E-02	2,66E-02	4,79E-03
2,15E-08	8,14E-02	2,20E-02	6,33E-02	6,24E-03	6,46E-02	4,53E-03	6,38E-02	7,11E-03
3,87E-08	1,15E-01	5,49E-03	1,33E-01	1,41E-02	1,26E-01	7,79E-03	1,31E-01	1,17E-02
6,97E-08	2,20E-01	3,53E-02	1,69E-01	1,11E-02	2,04E-01	2,12E-02	1,61E-01	1,01E-02
1,25E-07	1,84E-01	4,97E-02	1,40E-01	1,00E-02	1,65E-01	1,86E-02	1,31E-01	6,93E-03
2,25E-07	4,86E-02	4,64E-03	5,18E-02	4,53E-03	5,17E-02	2,48E-03	5,47E-02	2,02E-03
4,05E-07	4,56E-02	1,66E-02	3,52E-02	5,61E-03	3,05E-02	2,00E-03	3,14E-02	1,48E-03
7,29E-07	2,97E-02	4,68E-03	1,07E-01	8,31E-02	2,69E-02	2,17E-03	3,61E-02	3,63E-03
1,31E-06	2,14E-02	1,70E-03	2,72E-02	1,19E-03	2,86E-02	3,16E-03	3,77E-02	3,37E-03
2,36E-06	1,86E-02	1,08E-03	2,44E-02	8,95E-04	3,92E-02	1,36E-02	3,60E-02	1,24E-03
4,24E-06	2,18E-02	1,75E-03	2,47E-02	1,04E-03	2,31E-02	1,96E-03	3,53E-02	2,27E-03
7,63E-06	1,81E-02	2,56E-03	2,45E-02	2,55E-03	4,07E-02	2,02E-02	3,18E-02	1,13E-03
1,37E-05	1,62E-02	2,65E-03	1,86E-02	8,44E-04	1,59E-02	1,02E-03	2,75E-02	9,28E-04
2,47E-05	1,20E-02	1,10E-03	1,87E-02	8,74E-04	1,63E-02	1,44E-03	2,43E-02	9,35E-04
4,44E-05	1,40E-02	2,39E-03	1,55E-02	7,84E-04	2,06E-02	3,81E-03	2,26E-02	1,09E-03
7,98E-05	1,20E-02	1,94E-03	1,43E-02	8,68E-04	1,31E-02	2,06E-03	1,81E-02	9,38E-04
1,44E-04	1,17E-02	2,40E-03	1,16E-02	6,03E-04	9,82E-03	1,26E-03	1,47E-02	6,86E-04
2,58E-04	9,85E-03	2,43E-03	1,20E-02	2,79E-03	1,41E-02	4,94E-03	1,85E-02	6,50E-03
4,64E-04	1,15E-02	6,10E-03	1,51E-02	7,29E-03	8,29E-03	1,47E-03	8,75E-03	4,62E-04
8,35E-04	5,67E-03	5,18E-04	7,33E-03	4,64E-04	8,13E-03	1,19E-03	9,94E-03	5,35E-04
1,50E-03	6,36E-03	7,25E-04	6,98E-03	5,48E-04	7,38E-03	1,01E-03	1,02E-02	6,28E-04
2,70E-03	4,59E-03	4,99E-04	6,41E-03	5,04E-04	4,73E-03	5,56E-04	1,18E-02	2,90E-03
4,86E-03	4,29E-03	4,90E-04	6,77E-03	5,17E-04	5,23E-03	6,00E-04	1,01E-02	4,84E-04

SSR/SSW: Upper part: Tally 404, 414, 424, 434 (neutrons) (second part)									
	Tally 404		Tally 414		Tally 424		Tally 434		
	Normalized Values [a.u]								
Upper bin	Value	σ	Value	σ	Value	σ	Value	σ	
8,73E-03	3,88E-03	5,56E-04	6,12E-03	3,74E-04	5,72E-03	1,13E-03	8,82E-03	4,75E-04	
1,57E-02	2,60E-03	2,99E-04	5,64E-03	3,01E-04	3,52E-03	4,87E-04	8,75E-03	4,33E-04	
2,82E-02	2,13E-03	2,98E-04	5,93E-03	2,58E-03	3,05E-03	6,00E-04	4,84E-03	3,22E-04	
5,08E-02	1,73E-03	3,07E-04	2,18E-03	3,53E-04	3,89E-03	2,71E-03	4,72E-03	2,13E-03	
9,14E-02	1,01E-03	1,86E-04	2,12E-03	1,73E-04	5,30E-03	3,76E-03	4,64E-03	1,09E-03	
1,64E-01	1,15E-03	4,22E-04	1,80E-03	2,16E-04	9,83E-04	3,44E-04	2,75E-03	2,41E-04	
2,96E-01	3,50E-04	9,84E-05	7,54E-04	1,01E-04	3,65E-04	1,04E-04	1,50E-03	1,53E-04	
5,31E-01	1,12E-04	5,83E-05	1,59E-04	3,61E-05	4,68E-05	2,67E-05	3,10E-04	6,12E-05	
9,56E-01	0,00E+00	0,00E+00	0,00E+00	0,00E+00	0,00E+00	0,00E+00	1,07E-05	1,07E-05	
1,72E+00	0,00E+00	0,00E+00	0,00E+00	0,00E+00	0,00E+00	0,00E+00	0,00E+00	0,00E+00	
3,09E+00	0,00E+00	0,00E+00	0,00E+00	0,00E+00	0,00E+00	0,00E+00	0,00E+00	0,00E+00	
5,56E+00	0,00E+00	0,00E+00	0,00E+00	0,00E+00	0,00E+00	0,00E+00	0,00E+00	0,00E+00	
1,00E+01	0,00E+00	0,00E+00	0,00E+00	0,00E+00	0,00E+00	0,00E+00	0,00E+00	0,00E+00	
total	1,00E+00	7,78E-02	1,00E+00	1,16E-01	1,00E+00	5,69E-02	1,00E+00	2,54E-02	

SSR/SSW: Upper part: Tally 444, 454 (neutrons) (first part)				
	Tally 444		Tally 454	
	Normalized Values [a.u]			
Upper bin	Value	σ	Value	σ
1,00E-12	0,00E+00	0,00E+00	0,00E+00	0,00E+00
1,80E-12	0,00E+00	0,00E+00	0,00E+00	0,00E+00
3,23E-12	0,00E+00	0,00E+00	0,00E+00	0,00E+00
5,82E-12	0,00E+00	0,00E+00	0,00E+00	0,00E+00
1,05E-11	0,00E+00	0,00E+00	0,00E+00	0,00E+00
1,88E-11	0,00E+00	0,00E+00	0,00E+00	0,00E+00
3,38E-11	0,00E+00	0,00E+00	0,00E+00	0,00E+00
6,09E-11	0,00E+00	0,00E+00	0,00E+00	0,00E+00
1,09E-10	0,00E+00	0,00E+00	0,00E+00	0,00E+00
1,97E-10	3,76E-03	3,73E-03	6,80E-06	6,80E-06
3,54E-10	0,00E+00	0,00E+00	4,62E-05	3,47E-05
6,37E-10	2,05E-04	1,33E-04	2,86E-05	1,56E-05
1,15E-09	4,45E-04	1,18E-04	6,47E-04	3,84E-04
2,06E-09	1,00E-03	2,17E-04	9,72E-04	1,78E-04
3,70E-09	3,17E-03	4,45E-04	2,80E-03	3,14E-04
6,66E-09	9,81E-03	1,12E-03	6,53E-03	5,59E-04
1,20E-08	2,70E-02	2,15E-03	2,95E-02	6,93E-03
2,15E-08	7,71E-02	8,36E-03	5,75E-02	3,32E-03
3,87E-08	1,53E-01	2,40E-02	1,17E-01	7,25E-03
6,97E-08	2,26E-01	3,06E-02	1,86E-01	1,69E-02
1,25E-07	1,38E-01	6,58E-03	1,24E-01	6,10E-03
2,25E-07	6,31E-02	6,19E-03	6,84E-02	8,50E-03
4,05E-07	3,24E-02	3,46E-03	3,02E-02	1,43E-03
7,29E-07	2,48E-02	1,66E-03	3,21E-02	1,59E-03
1,31E-06	2,67E-02	3,03E-03	3,68E-02	1,81E-03
2,36E-06	3,80E-02	1,40E-02	4,39E-02	8,31E-03
4,24E-06	2,58E-02	2,22E-03	3,43E-02	1,72E-03
7,63E-06	1,72E-02	1,09E-03	2,99E-02	1,22E-03
1,37E-05	1,93E-02	1,76E-03	2,68E-02	1,21E-03
2,47E-05	1,59E-02	1,56E-03	2,47E-02	1,35E-03
4,44E-05	1,53E-02	1,54E-03	1,95E-02	9,24E-04
7,98E-05	1,07E-02	8,61E-04	1,66E-02	9,01E-04
1,44E-04	1,03E-02	1,06E-03	1,41E-02	7,41E-04
2,58E-04	8,34E-03	1,10E-03	1,73E-02	6,31E-03
4,64E-04	7,43E-03	1,13E-03	8,53E-03	4,99E-04
8,35E-04	5,43E-03	5,63E-04	1,00E-02	5,65E-04
1,50E-03	6,77E-03	6,74E-04	9,36E-03	5,16E-04
2,70E-03	5,85E-03	8,09E-04	8,33E-03	7,18E-04
4,86E-03	6,15E-03	9,21E-04	8,35E-03	5,27E-04
8,73E-03	6,01E-03	1,08E-03	8,48E-03	6,83E-04
1,57E-02	7,77E-03	3,87E-03	1,32E-02	5,03E-03
2,82E-02	1,78E-03	2,69E-04	5,18E-03	5,28E-04

SSR/SSW: Upper part Tally 444, 454 (neutrons) (second part)				
	Tally 444		Tally 454	
	Normalized Values [a.u]			
Upper bin	Value	σ	Value	σ
5,08E-02	3,22E-03	2,24E-03	2,72E-03	3,00E-04
9,14E-02	1,03E-03	2,99E-04	2,88E-03	2,65E-04
1,64E-01	7,63E-04	1,67E-04	2,59E-03	2,73E-04
2,96E-01	4,96E-04	1,78E-04	1,05E-03	1,46E-04
5,31E-01	4,74E-05	2,81E-05	4,55E-04	1,18E-04
9,56E-01	0,00E+00	0,00E+00	0,00E+00	0,00E+00
1,72E+00	0,00E+00	0,00E+00	0,00E+00	0,00E+00
3,09E+00	0,00E+00	0,00E+00	0,00E+00	0,00E+00
5,56E+00	0,00E+00	0,00E+00	0,00E+00	0,00E+00
1,00E+01	0,00E+00	0,00E+00	0,00E+00	0,00E+00
total	1,00E+00	5,14E-02	1,00E+00	3,35E-02

SSR/SSW: Lower part (neutrons) (first part)						
	Tally 464		Tally 474		Tally 484	
	Normalized Values [a.u]					
Upper bin	Value	σ	Value	σ	Value	σ
1,00E-12	0,00E+00	0,00E+00	0,00E+00	0,00E+00	0,00E+00	0,00E+00
1,80E-12	0,00E+00	0,00E+00	0,00E+00	0,00E+00	0,00E+00	0,00E+00
3,23E-12	0,00E+00	0,00E+00	0,00E+00	0,00E+00	0,00E+00	0,00E+00
5,82E-12	0,00E+00	0,00E+00	0,00E+00	0,00E+00	0,00E+00	0,00E+00
1,05E-11	0,00E+00	0,00E+00	0,00E+00	0,00E+00	0,00E+00	0,00E+00
1,88E-11	0,00E+00	0,00E+00	0,00E+00	0,00E+00	0,00E+00	0,00E+00
3,38E-11	0,00E+00	0,00E+00	0,00E+00	0,00E+00	0,00E+00	0,00E+00
6,09E-11	0,00E+00	0,00E+00	0,00E+00	0,00E+00	0,00E+00	0,00E+00
1,09E-10	0,00E+00	0,00E+00	0,00E+00	0,00E+00	0,00E+00	0,00E+00
1,97E-10	4,11E-05	2,12E-05	4,25E-06	3,25E-06	9,27E-06	9,27E-06
3,54E-10	2,85E-05	1,39E-05	2,55E-05	1,20E-05	3,12E-05	1,38E-05
6,37E-10	1,50E-04	3,36E-05	6,97E-05	1,85E-05	8,05E-05	1,96E-05
1,15E-09	4,73E-04	7,77E-05	1,94E-04	3,42E-05	2,63E-04	4,00E-05
2,06E-09	1,43E-03	1,27E-04	8,30E-04	8,29E-05	7,50E-04	6,97E-05
3,70E-09	4,16E-03	2,16E-04	2,05E-03	1,11E-04	2,43E-03	1,38E-04
6,66E-09	1,17E-02	3,74E-04	7,22E-03	2,85E-04	7,08E-03	2,38E-04
1,20E-08	3,41E-02	6,99E-04	1,93E-02	4,90E-04	2,16E-02	6,99E-04
2,15E-08	8,22E-02	1,31E-03	4,99E-02	1,09E-03	5,22E-02	1,11E-03
3,87E-08	1,58E-01	2,15E-03	9,78E-02	1,90E-03	1,06E-01	2,14E-03
6,97E-08	2,15E-01	2,84E-03	1,35E-01	2,54E-03	1,44E-01	2,88E-03
1,25E-07	1,59E-01	2,19E-03	1,04E-01	2,07E-03	1,13E-01	2,35E-03
2,25E-07	5,94E-02	1,07E-03	4,84E-02	1,13E-03	5,08E-02	1,18E-03
4,05E-07	3,04E-02	7,43E-04	3,65E-02	1,01E-03	3,54E-02	9,50E-04
7,29E-07	2,89E-02	7,54E-04	4,04E-02	1,19E-03	3,74E-02	1,05E-03
1,31E-06	2,78E-02	7,49E-04	4,49E-02	1,29E-03	4,29E-02	1,30E-03
2,36E-06	2,62E-02	7,43E-04	4,64E-02	1,44E-03	4,45E-02	1,35E-03
4,24E-06	2,49E-02	7,41E-04	4,76E-02	1,65E-03	4,32E-02	1,46E-03
7,63E-06	2,20E-02	6,92E-04	4,32E-02	1,63E-03	4,12E-02	1,52E-03
1,37E-05	1,95E-02	7,06E-04	3,83E-02	1,54E-03	3,58E-02	1,41E-03
2,47E-05	1,69E-02	6,15E-04	3,47E-02	1,57E-03	3,41E-02	1,48E-03
4,44E-05	1,51E-02	6,44E-04	2,94E-02	1,42E-03	2,95E-02	1,46E-03
7,98E-05	1,19E-02	5,26E-04	2,51E-02	1,38E-03	2,49E-02	1,27E-03
1,44E-04	8,50E-03	4,33E-04	2,08E-02	1,24E-03	2,07E-02	1,22E-03
2,58E-04	7,15E-03	3,90E-04	1,56E-02	9,80E-04	1,55E-02	9,70E-04
4,64E-04	5,42E-03	3,24E-04	1,00E-02	7,00E-04	1,06E-02	7,14E-04
8,35E-04	5,55E-03	3,33E-04	1,45E-02	1,07E-03	1,39E-02	9,58E-04
1,50E-03	5,24E-03	3,34E-04	1,21E-02	9,63E-04	1,18E-02	8,79E-04
2,70E-03	4,32E-03	2,91E-04	9,29E-03	8,46E-04	8,70E-03	7,44E-04
4,86E-03	3,63E-03	3,00E-04	1,23E-02	1,31E-03	1,05E-02	9,50E-04
8,73E-03	3,09E-03	2,45E-04	1,27E-02	1,39E-03	9,80E-03	9,87E-04
1,57E-02	2,94E-03	2,33E-04	1,40E-02	1,69E-03	1,11E-02	1,34E-03

SSR/SSW: Lower part (neutrons) (second part)						
	Tally 464		Tally 474		Tally 484	
	Normalized Values [a.u]					
Upper bin	Value	σ	Value	σ	Value	σ
2,82E-02	1,98E-03	2,83E-04	9,48E-03	1,51E-03	7,53E-03	1,01E-03
5,08E-02	9,54E-04	1,39E-04	3,82E-03	6,92E-04	3,28E-03	5,31E-04
9,14E-02	9,06E-04	1,31E-04	6,33E-03	1,13E-03	3,70E-03	5,85E-04
1,64E-01	1,07E-03	3,83E-04	5,20E-03	9,25E-04	3,86E-03	6,24E-04
2,96E-01	3,72E-04	9,04E-05	1,82E-03	3,89E-04	1,90E-03	3,69E-04
5,31E-01	1,05E-04	4,25E-05	6,01E-04	1,99E-04	5,00E-04	1,50E-04
9,56E-01	0,00E+00	0,00E+00	2,36E-05	2,36E-05	0,00E+00	0,00E+00
1,72E+00	0,00E+00	0,00E+00	0,00E+00	0,00E+00	0,00E+00	0,00E+00
3,09E+00	0,00E+00	0,00E+00	0,00E+00	0,00E+00	0,00E+00	0,00E+00
5,56E+00	0,00E+00	0,00E+00	0,00E+00	0,00E+00	0,00E+00	0,00E+00
1,00E+01	0,00E+00	0,00E+00	0,00E+00	0,00E+00	0,00E+00	0,00E+00
total	1,00E+00	1,24E-02	1,00E+00	2,61E-02	1,00E+00	2,54E-02

Finally, the following table expresses the automatically determined data by the TopMc processor. Since the exact dimension of the slab under study cannot be disclosed, the depth would be expressed as a fraction of the total length "L".

SDEF: Shortest path through lead (photons) (second part)		
	Tally 104	
Depth	Dose [Gr/h]	σ
0	1,20E+03	1,74E+01
1/10 L	4,15E+00	0,139090267
2/10 L	3,48E-02	0,00151842
3/10 L	3,12E-04	1,63847E-05
4/10 L	2,99E-06	1,72102E-07
5/10 L	2,97E-08	1,71511E-09
6/10 L	3,19E-10	1,8628E-11
7/10 L	3,46E-12	2,31432E-13
8/10 L	3,38E-14	2,14437E-15
9/10 L	4,38E-16	3,13155E-17
L	2,78E-16	2,00167E-17

References

- [1] N. Bohr and J. A. Wheeler. The mechanism of nuclear fission. *Physical Review*, 56:426–450, 1939.
- [2] K. S. Krane. Nuclear reaction. In *Introductory Nuclear Physics*, pages 378–520. John Wiley & Sons, 1987.
- [3] J. R. Lamarsh and A. J. Baratta. Interaction of radiation with matter. In *Introduction to Nuclear Engineering*, chapter 3, pages 52–116. Prentice Hall, 3rd edition, 2001.
- [4] World Nuclear Association. Physics of uranium and nuclear energy, 2023. Available on: <https://world-nuclear.org/information-library/nuclear-fuel-cycle/introduction/physics-of-nuclear-energy>.
- [5] G. F. Knoll. Radiation sources. In *Radiation Detection and Measurement*, chapter 1, pages 3–38. John Wiley & Sons, 1979.
- [6] N. E. Todreas and M. S. Kazimi. Thermal hydraulic characteristics of power reactors. In *Nuclear Systems I: Thermal Hydraulic Fundamentals*, chapter 1, pages 1–18. Taylor & Francis, 1990.
- [7] World Nuclear Association. Nuclear power reactors, 2023. Available on: <https://world-nuclear.org/information-library/nuclear-fuel-cycle/nuclear-power-reactors/nuclear-power-reactors.aspx>.
- [8] International Atomic Energy Agency (IAEA). Advanced Reactors Information System (ARIS), 2023. Available on: <https://aris.iaea.org/>.
- [9] World Nuclear Association. Safety of nuclear power reactors, 2023. Available on: <https://world-nuclear.org/information-library/safety-and-security/safety-of-plants/safety-of-nuclear-power-reactors.aspx>.
- [10] World Nuclear Association. Generation iv nuclear reactors, 2023. Available on: Generation IV Nuclear Reactors - World Nuclear Association.
- [11] Generation IV International Forum (GIF). A technology roadmap for generation iv nuclear energy systems, 2002. Available on [Generation IV *Vody.pmd*.p65](#).
- [12] A. Waltar, D. Todd, and P. Tsvetkov. Gas-cooled fast reactors. In *Fast Spectrum Reactors*, chapter 17, pages 489–512. Springer, 2012.
- [13] A. Waltar, D. Todd, and P. Tsvetkov. Lead-cooled fast reactors. In *Fast Spectrum Reactors*, chapter 18, pages 513–532. Springer, 2012.
- [14] A. Alemberti, V. Smirnov, C. F. Smith, and M. Takahashi. The lead-cooled fast reactor: Status report for 2012 gif symposium, 2012. GEN IV International Forum, San Diego, CA, USA, November 14, 2012.
- [15] E. Khodarev. Liquid metal fast breeder reactors. *IAEA Bulletin*, 20(6), 1978.
- [16] E. L. Gluekler. U.s. advanced liquid metal reactor (ALMR). *Progress in Nuclear Energy*, 31(1-2):43–61, 1997.
- [17] Ricerca Sistema Elettrico, ENEA. Report sulla interazione fuel-coolant in sistemi lfr. Technical report, ADPFISS – LP2 - 006, 2013.
- [18] OECD Nuclear Energy Agency. Handbook on lead-bismuth eutectic alloy and lead properties, materials compatibility, thermal-hydraulics and technologies. Technical report, OECD, 2015.

REFERENCES

- [19] A. Alemberti et al. Overview of lead-cooled fast reactor activities. *Progress in Nuclear Energy*, 77:300–307, 2014.
- [20] European Commission. Final Report Summary - LEADER (Lead-cooled European Advanced Demonstration Reactor), 2024. Available on: Lead-cooled European Advanced Demonstration Reactor — FP7 — CORDIS.
- [21] Associazione Italiana Nucleare. Sostenibilità dei reattori nucleari a piombo. Technical report, Quaderno AIN n.9, 2019.
- [22] C. F. Smith, D. Crawford, M. Cappiello, A. Minato, and J. W. Herczeg. The small modular liquid metal cooled reactor: A new approach to proliferation risk management. In *14th Pacific Basin Nuclear Conference*, Honolulu, HI, March 2004.
- [23] M. Ciotti, E. Ruberti, and J. L. Manzano. Nucleare di nuova generazione: i reattori a piombo. *Energia*, 16(4), 2020.
- [24] A. Buscarino. Overview on lead-cooled fast reactor design and related technologies developed in ENEA. *Energies*, 14(17):5360, 2021.
- [25] G. Bignan et al. The key-role of instrumentation for the new generation of research reactors. In *2nd International Conference on Advancements in Nuclear Instrumentation, Measurement Methods and their Applications*, pages 1–8. IEEE, 2011.
- [26] Tsai K. Characterizing the performance of fission chambers for local neutron flux and spectrum measurement. *Idaho National Laboratory*, 2022.
- [27] G. F. Knoll. General properties of radiation detectors. In *Radiation Detection and Measurements*, chapter 3, pages 79–103. John Wiley & Sons, 1979.
- [28] Z. Lyric. A review on the modeling of fission chambers. Master’s thesis, Department of Mechanical and Nuclear Engineering, Kansas State University, Manhattan, KS, USA, 2017.
- [29] L. Lepore. Analisi di sonde neutroniche commerciali per installazioni in ambienti ad alta temperatura. In *Ottimizzazione della strumentazione di monitoraggio neutronico del nocciolo di un reattore LFR*, chapter Capitolo 3, pages 85–87. Sapienza Università di Roma, 2016.
- [30] Shanqi Chen, Bin Wu, Zhengyun Dong, Shaoheng Zhou, Guangyao Sun, Li He, Dong Yao, Shengpeng Yu, Quan Gan, Lijuan Hao, Jing Song, Pengcheng Long, Yazhou Li, Jieqiong Jiang, Fang Wang, Liqin Hu, Yican Wu, and FDS Consortium. Development of topmc 1.0 for nuclear technology applications. *EPJ Nuclear Sci. Technol.*, 11:6, 2025.
- [31] L. Lepore. Il termine sorgente: il reattore LFR dimostrativo ALFRED. In *Ottimizzazione della strumentazione di monitoraggio neutronico del nocciolo di un reattore LFR*, chapter Capitolo 2, pages 53–78. Sapienza Università di Roma, 2016.
- [32] Christopher J. Werner. *MCNP user’s manual, code version 6.2*, 2017.
- [33] Yuefeng Qiu and Lei Lu. *McCad User Guide*. Available on: [McCadUserGuidev051.896208093.pdf](#).
- [34] Christopher J. Werner. Data cards related to tally specification. In *MCNP user’s manual, code version 6.2*, pages 3–186–3–203. 2017.
- [35] Christopher J. Werner. Data cards related to source definition. In *MCNP user’s manual, code version 6.2*, pages 3–124–3–157. 2017.
- [36] Christopher J. Werner. Data cards related to source definition. In *MCNP user’s manual, code version 6.2*, pages 3–158–3–165. 2017.

REFERENCES

- [37] X-5 Monte Carlo Team. Variance reduction. In *MCNP - A General Monte Carlo N-Particle Transport Code, Version 5*, pages 2-147-2-250. 2003.
- [38] Oak Ridge National Laboratory. *ADVANTG 3.0: AutomateD VARIance reducTion Generator (RSICC Code Package CCC-0831)*, 2016. Oak Ridge, TN: UT-Battelle, LLC for the U.S. Department of Energy.
- [39] M. B. Chadwick, M. Herman, P. Obložinský, et al. ENDF/B-VII.1 nuclear data for science and technology: Cross sections, covariances, fission product yields and decay data. *Nuclear Data Sheets*, 112(12):2887-2996, 2011. Special Issue on ENDF/B-VII.1 Library.
- [40] G. Firpo, M. Frignani, and C. M. Viberti. Benchmarking of mancintap 2.0, a parallel high-performance tool for neutron activation analysis in complex 4d scenarios. *The European Physical Journal Plus*, 135:105, 2020.
- [41] Christopher J. Werner. Data cards related to tally specification. In *MCNP user's manual, code version 6.2*, pages 3-231-3-224. 2017.
- [42] OECD NEA. Janis book view - neutrons - u235 (MT1), 2024.